Characterization of igneous terranes by zircon dating: implications for the UHP relicts occurrences and suture identification in the Central Rhodope, Northern Greece

Dissertation
zur Erlangung des Grades
"Doktor der Naturwissenschaften"

am Fachbereich Chemie, Pharmazie und Geowissenschaften
der Johannes Gutenberg-Universität, Mainz

Philippe Turpaud

geboren in Montpellier (France)

Mainz, January 2006

All views and results presented in this thesis are those of the author, unless stated otherwise.

Ich versichere, dass ich die vorliegende Arbeit selbständig und nur unter Verwendung der angegebenen Quellen und Hilfsmittel verfasst habe.

Mainz, January 2006

Foreword

This work has been presented in international conferences giving rise to the publication of the following abstracts:

Turpaud, P., Reischmann, T., 2005. Relationships between crustal blocks and UHP relicts, an example from Northern Greece. *Geophysical Research Abstracts, 04353, 7. (Poster presentation)*

Turpaud, P., Reischmann, T., 2004. Identification of Terranes by zircon dating in the western Greek Rhodope and relationships with UHP relics. *Joint Earth Science Meeting (Société Géologique de France and Geologische Vereinigung), Strasbourg. (Oral presentation).*

Turpaud, P., Reischmann, T., 2003. Zircon ages of granitic gneisses from the Rhodope (N. Greece), determination of basement age and evidences for a Cretaceous intrusive event. *Geophysical Research Abstracts, 04435, 5. (Poster presentation)*

Abstract

One of the key for the understanding of an orogenic belt is the characterization of the terranes involved and the identification of the suture(s) separating crustal blocks: these are essential information for large-scale paleo-reconstructions. In addition, the structural relationships between the terranes involved in the collisional processes and the eventual UHP relicts may provide first order inputs to exhumation models of subducted rocks.

The structure of the Rhodope Massif (northern Greece and southern Bulgaria) results from the stacking of high-grade nappes during a continental collision, which age is comprised between Latest-Jurassic and Early-Cenozoic. UHP and HP relicts, associated with oceanic and ultramafic material, suggest the presence of a dismembered suture zone within the massif. The location of this suture remains unclear; furthermore, up to now, the UHP and eclogitic localities represent isolated spots and no synthesis on their structural position within the massif has been proposed. The first aim of this work is to define the relationships between HP-UHP relicts, crustal blocks, shear zones and amphibolitic material. To achieve this objective, we characterized the accreted blocks in terms of protoliths ages of the orthogneisses mainly along two cross sections on the Greek part of the belt. Geochemical affinities of meta-igneous rocks served as a complementary tool for terrane characterization and geodynamic interpretation.

Single-zircon Pb-Pb evaporation and zircon U-Pb SHRIMP dating of orthogneiss protoliths define two groups of intrusion-ages: Permo-Carboniferous and Late Jurassic-Early Cretaceous. Structurally, these two groups correspond to distinct units: the Late Jurassic gneissic complex overthrusts the one bearing the Permo-Carboniferous orthogneisses. Mylonites, eclogites, amphibolites of oceanic affinities, and UHP micaschists, mark a "melange" zone, intensively sheared towards the SW, which separates the two units. Thus, we interpret them as two distinct terranes, the Rhodope and Thracia terranes, separated by the Nestos suture. The correlation of our findings in northern Greece to the Bulgarian part of the Massif suggests a northern rooting of the Nestos Suture. This configuration results of the closure of a marginal oceanic basin of the Tethys system by a north-directed subduction. This interpretation is supported by the geochemical affinities of the orthogneisses: the Late-Jurassic igneous rocks formed by subduction-related magmatism, pprobably the same north-directed subduction that gave rise to the UHP metamorphism of the metasediments of the "melange" zone. It is noteworthy that the UHP-HP relicts seem to be restricted to the contact between the two terranes suggesting that the UHP relicts are exhumed only within the suture zone. Furthermore, the singularity of the suture suggests that the Late-Jurassic subduction explains the occurrence of UHP and eclogite relicts in the Central Rhodope despite the large age range previously attributed the UHP and/or HP stage.

Résumé

Une des premières problématiques à résoudre dans une orogène représente la caractérisation des blocs impliqués dans la collision et l'identification de la sututre les separant. Ces informations sont des bases pour les reconstituions paléogéographiques. De plus, les relations entre blocs crustaux et les éventuelles reliques de UHP (ultra haute pression) fournissent d'importantes contraintes pour tout modèle (numérique ou conceptuel) d'exhumation des roches profondément subductées.

La structure du Massif du Rhodope (Grèce du Nord et Bulgarie du Sud) résulte de l'empilement de nappes de haut grade au cours d'une collision continentale dont l'age est compris entre le Jurassique terminal et le début du Tertiaire. La présence de reliques de UHP ainsi que d'éclogites, associées à des amphibolites d'affinité océanique et des péridotites, suggère la présence d'une suture au sein du massif. La localisation de cette suture est incertaine ; de plus, jusqu'à présent, les reliques éclogitiques et de UHP représentent des affleurements isolés sans qu'une synthèse concernant leur position structurale n'ait été proposée. Le but de ce travail est donc de définir les relations entre les reliques de UHP/eclogites et les blocs crustaux, zones de cisaillement et matériel amphibolitique. Dans ce but, nous caractérisons les blocs crustaux accrétés par la datation des protolithes des orthogneiss et par leurs affinités géochimiques, principalement le long de deux coupes perpendiculaires aux structures dans la partie grecque du massif.

La datation du protholithe des orthogneiss permet l'identification de deux unités majeures. Les datations mono grain par la méthode Pb-Pb et ponctuelles U-Pb SHRIMP sur zircons définissent deux groupes d'ages d'intrusion : Permo-Carbonifère et Jurassique supérieur/Crétacé inférieur. Du point de vue structural, ces deux groupes correspondent à des unités distinctes ; l'unité gneissique jurassique supérieur chevauche l'unité contenant les gneiss permo-carbonifères. Une zone de "mélange", fortement cisaillée en direction du Sud-Ouest, marquée par mylonites, eclogites, amphibolite d'affinités océaniques et micaschistes de UHP, sépare ces deux blocs. Ainsi, nous interprétons ces unités comme deux « terranes » distincts, respectivement le terrane du Rhodope et Thracia, séparés par la suture du Nestos. La corrélation avec la partie Bulgare du massif permet de proposer un enracinement septentrional de la suture du Nestos. La configuration actuelle résulte de la fermeture par une subduction, en direction Nord, d'un bassin océanique marginal de la Tethys. Les affinités géochimiques des échantillons datés suggèrent que les roches plutoniques du Jurassique supérieur sont issues d'un magmatisme d'arc, ce dernier probablement lié à la même subduction qui a engendré le métamorphisme de UHP. Une observation marquante est que les reliques éclogitiques et de UHP semblent restreintes à la fine zone de "mélange" marquant la suture entre les deux blocs. Ceci suggère que les reliques de UHP sont exhumées uniquement au sein de la zone de suture. De plus, cette relation géométrique nous permet de proposer qu'une unique phase métamorphique de HP-UHP peut expliquer la présence d'éclogites et de reliques de UHP dans le Rhodope Central. Ce point contredit l'importante dispersion des ages radiométriques interprétés comme datant la phase de HP-UHP.

Abstract for my family
(or how to explain them what I did the last four years)

In the Mediterranean region, plate tectonic framework is characterized by the convergence of Africa and Europe since ca. 160 Million years. Plate tectonics is the result of the movement of the rigid plates over the more ductile Earth's mantle. For example, this convergence gave birth to the well known Alps or Pyrenees. These mountainous areas rose through collision between several continental blocks after the closure of an ocean, the Tethys. Also in Greece this convergence gave rise to the stacking of several micro-blocks originally separated by small oceanic basins; the accretion started earlier in the north and then propagated towards the south. This convergence is nowadays still directly evidenced by the subduction (deepening, sinking of a plate below another one by transfer of horizontal velocity in a vertical component, see Fig. 2) of what is left of the Tethys below the southern Aegean Islands. This subduction is the reason for active volcanism in some Aegean islands such as Santorini, Milos and Nisiros.

Although this general frame is well known by the geologic community, some parts of the past evolution of the Mediterranean region are still ambiguous. The Rhodope Massif (northern Greece) is a poorly known area. Although we know that it suffered a deformation due to compression and collision, we do not know exactly which continents collided (neither exactly when). Further more, recently some exceptional rocks have been discovered within this massif: some sedimentary and oceanic rocks, after their formation on an ocean floor, experienced a burial of more than 150 Km. The presence of micro-diamonds within them is the proof for their deep burying. These are not the diamonds you will find in jewellery, they are 10 µm in size (hundredth of millimetre) and they were formed in a completely different setting than the gem quality ones. As nowadays we can walk on these rocks without special equipment, obviously, they must have come back to the surface after their burial. The mechanism leading to their exhumation is still not fully understood and is one of the more fundamental problems in Earth Sciences. Instead, the way of burying these rocks is consensual: they must have belonged to a subducting plate, wich brought them so deep from the Earth surface. Therefore, this deep burial represents an insight for an active subduction in the region (but when?).

Consequently, the first order questions of this work were:

- Which continents were involved in the collision process
- But what characterizes them and what are the relationships between them and the rocks having experienced deep burial?
- When did this all happen?

Answering these questions can give major constrain on the past evolution of this sector of the Earth in terms of plate tectonics; more fundamentally, observations on the tectonic setting of deeply buried rocks will widen the understanding of subduction and exhumation processes.

To add some hints of answer to these problems, I did field observations and dated the crystallisation of granites, nowadays deformed. A granite results from the crystallization of a magma in depth. When it is later deformed, it is called an orthogneiss. The way of dating their original crystallisation is, in theory, simple. Small minerals (the zircons) in the granite trap some uranium during crystallisation. This Uranium remains confined within this container. Uranium is radioactive, and decays in Lead at a constant and well known rate. Therefore, it is enough to measure the ratio between Uranium and Lead within the container (the zircon) to know the age of the rock.

Present overall structure of the Rhodope Massif

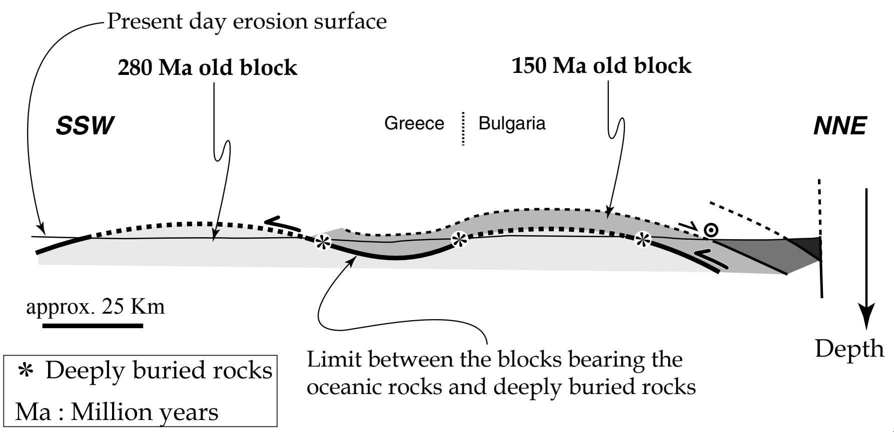

Fig. 1. Idealized vertical section through the Rhodope Massif. This "vertical cut", oriented NNE-SSW, shows the main result of this work: a block, built of 150 Million years old granites, lies above a different one (bearing 280 Million years old granites). The arrows indicate the senses of transport of the upper block. It is between these two blocks that the oceanic material and the deeply buried rocks are found. This contact is therefore interpreted as a border between two continents that where previously separated by an ocean (see Fig. 2)

My age results are split in two groups: one group of granites is 280 Million years (Ma) old and another one is 150 Ma old. At a large scale, the 150 Ma old group forms a block that has been transported by tectonic movement above the other one (the 280 Ma old one). It is between them that we find most of the oceanic rocks; the rocks bearing the micro-diamonds are also present between these two blocks (see Fig. 1). Furthermore, based on the chemical analyses of the rocks of the overlying block, I suggest that it is the result of the crystallisation of granites formed above a subduction zone.

These observations are interpreted as being the result of the collision of two micro-continents after the closure of the ocean separating them (Fig. 2). The ocean closed by progressive disappearance below the overlying block (the 150 Ma old one). As temperature increases with depth, its sinking led to the heating of the subducting plate and its dehydration. The fluid released induced the melting of the mantle. The magma ascended until the crust, where it crystallized to form the 150 Ma old granites. At the same time, the rocks belonging to the subducting plate experienced extremely deep burial. Some of these rocks came back to the Earth surface by a not fully understood process. Nevertheless, I propose that these rocks are only located between the two blocks. Hopefully, this last observation can help other scientists that are dealing with the question "By which mechanism deeply buried rocks come back on Earth surface?".

The Rhodope Massif 150 Million years ago

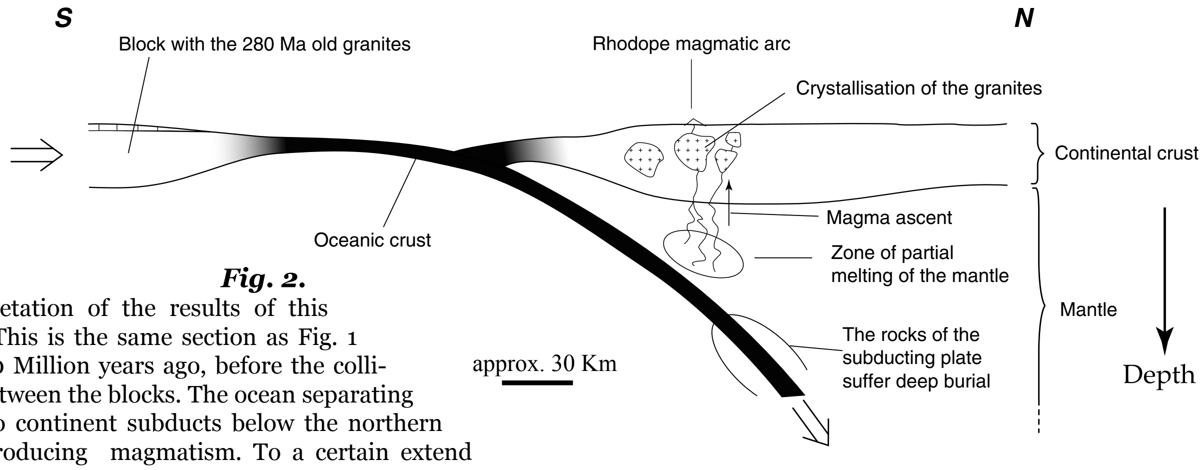

Fig. 2. Interpretation of the results of this work. This is the same section as Fig. 1 but 150 Million years ago, before the collision between the blocks. The ocean separating the two continent subducts below the northern one, producing magmatism. To a certain extend this model represents an analogous of other subduction zones, such as the present-day setting of the Aegean or of the Andes. The size of the ocean is unknown.

Résumé pour ma famille
(ou comment leur expliquer ce que j'ai fait les quatre dernières années)

En Méditerranée, la tectonique des plaques est caractérisée par la convergence de l'Afrique et de L'Europe depuis 160 Millions d'années. La tectonique des plaques résulte du mouvement de plaques rigides sur le manteau terrestre. Par exemple, cette convergence a donné lieu à la surrection des Alpes et des Apennins. Ces montagnes se sont érigées par collision entre plusieurs blocs continentaux après la fermeture d'un océan, la Thétis. Aussi en Grèce cette convergence a produits l'accrétion de plusieurs micros blocs précédemment séparés par de petits bassins océaniques; l'accrétion a commencé au Nord puis c'est propagé vers le Sud. La convergence entre l'Afrique et l'Europe est toujours tangible par la subduction de ce qui reste de la Thétis sous les îles des Cyclades. Une subduction est l'enfouissement d'une plaque sous une autre par transfert de vélocité horizontale en un component vertical (Fig. 2). Cette subduction est la raison du volcanisme de l'Egée (Santorin,...).

Bien que ce cadre général soit bien connu de la communauté géologique, quelques zones d'ombres dans l'évolution du pourtour méditerranéen subsistent. Le Massif du Rhodope (Grèce du Nord) est une région mal connue. Si nous savons qu'il fut déformé à cause d'une compression et collision, en revanche nous ne savons pas entre quoi et quoi (ni exactement quand, pour dire la vérité). De plus, récemment, des roches exceptionnelles ont été découvertes dans le massif : des roches sédimentaires et océaniques, après leur formation sur le fond océanique, on subit un enfouissement de plus de 150 Km. La présence de micros diamants préservés en leur sein est la preuve de leur enfouissement profond. Ces diamants ne sont pas ceux que vous trouverez chez votre joaillier, ils font 10 µm (un centième de millimètre) et se sont formés dans un environnement complètement différent de ceux de qualité gemme (mais c'est une autre histoire). Comme il est possible aujourd'hui de marcher sur ces roches sans équipement spécial, nous devons admettre qu'elles sont revenues à la surface après leur enfouissement. Les mécanismes permettant leur retour à la surface ne sont pas complètement compris et font partis des problématiques les plus actuelles en Science de la Terre. Au contraire la façon de les enfouir est consensuel : elles ont dut appartenir à une plaque subductée pour les amener aussi profond. Donc cet enfouissement a plus de 150 Km suggère qu'une subduction était active dans la région (mais quand ?).

En conséquence, les principales questions à l'origine du présent travail étaient :

- Entre quoi et quoi la collision a eu lieu ?
- Cette collision a impliqué deux blocs continentaux mais peut on mieux les caractériser ? Quelle est leur relation avec les roches ayant subit un enfouissement profond ?
- Quand tout cela c'est déroulé?

Répondre à ces questions peut non seulement apporter des contraintes majeures sur l'évolution passée de cette région en terme de tectonique des plaques, mais aussi plus fondamentalement, les observations sur le contexte tectonique des roches profondément enfouies élargira notre compréhension des mécanismes de subduction et d'exhumation.

Pour tenter de résoudre ces problèmes, j'ai réalisé des observations de terrain dans le nord de la Greece et daté la cristallisation de granites, aujourd'hui déformés. Un granite est un magma qui a cristallisé en profondeur. Quand il est déformé, il est appelé un orthogneiss. La méthode afin de dater leur cristallisation originelle est, en théorie, simple. De petits minéraux (les zircons) dans le granite capturent de l'uranium durant leur cristallisation. Cet uranium demeure confiné dans ce contenant. L'uranium étant radioactif, il se transforme en plomb a un rythme constant et extrêmement bien connu. Il suffit donc de mesurer le rapport entre les quantités d'uranium et de plomb présent aujourd'hui dans le zircon pour connaître son âge et par conséquent celui de la cristallisation du granite.

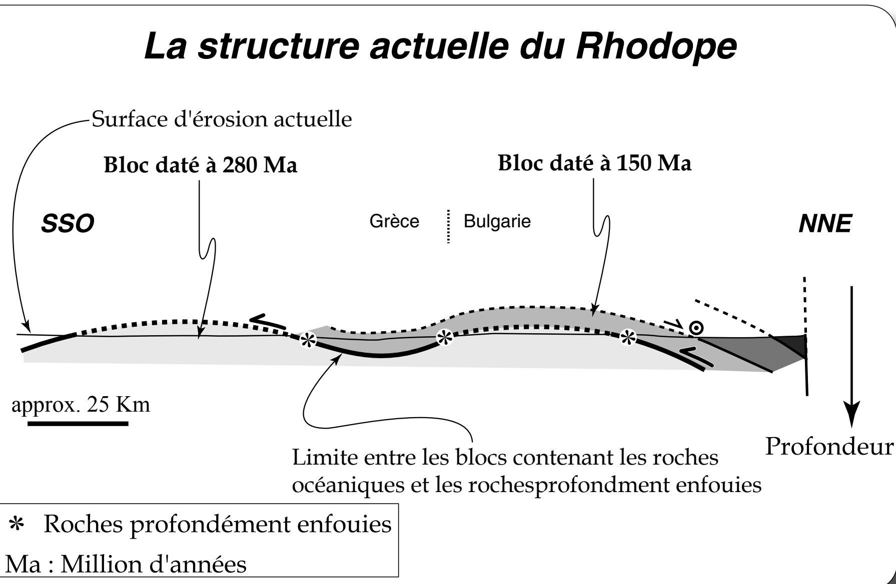

Fig. 1.
Section verticale idéalisée à travers le massif du Rhodope. Cette « tranche verticale », orientée NNE-SSO, montre les principaux résultats de ce travail : un bloc formé de granites datés a 150 Millions d'années fut transporté au dessus de celui contenant les granites datés à 280 Ma. Les flèches indiquent les sens de transport du bloc supérieur. C'est entre ces deux blocs que ce trouvent les roches océaniques et celles enfouies a plus de 150 Km de profondeur. Ce contact est donc interprété comme la frontière entre deux continents précédemment séparés par un océan (voir Fig. 2).

Les âges obtenus se divisent clairement en deux groupes : une suite de granite a 280 Millions d'années (Ma) et une autre a 150 Ma. En regardant à grande échelle, le groupe daté à 150 Ma fut transporté par mouvements tectoniques au-dessus de l'autre (celui vieux de 280 Ma). C'est au contact entre ces deux blocs que se trouvent les roches océaniques et celles contenant les micros diamants (Fig. 1). De plus la chimie des roches du bloc supérieur (150 Ma) nous suggèrent qu'elles sont le résultat de la cristallisation d'un magma formé au dessus d'une zone de subduction.

Ces observations sont interprétés comme étant le résultat de la collision de deux micros continents après la fermeture de l'océan qui les séparait (Fig. 2). Cet océan s'est fermé par disparition progressive sous le bloc supérieur (celui de 150 Ma). Comme la température s'élève avec la profondeur, la plaque océanique plongeante libéra des fluides qui provoquent la fonte partielle du manteau terrestre sus-jacent. Le magma produit s'éleva par différence de densité jusque dans la croûte, où sa cristallisation forma les granites âgés de 150 Ma. Au même moment, les roches appartenant à la plaque subductée subissent un enfouissement important. Une partie de ces roches sont revenues à la surface par un procédé qui n'est pas encore entièrement compris. Néanmoins, je propose que ces roches se trouvent seulement entre les deux blocs identifiés par cette étude. J'espère que cette dernière observation pourra aider d'autres scientifiques traitant de la question : « par quel mécanisme les roches profondément enfouies reviennent a la surface ? ».

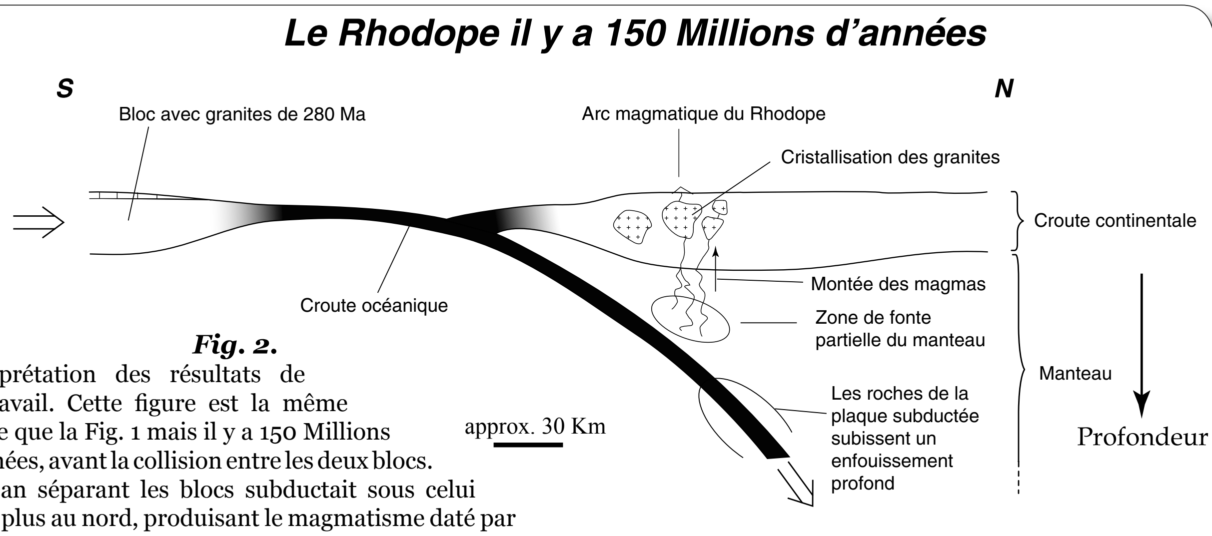

Fig. 2.
Interprétation des résultats de ce travail. Cette figure est la même coupe que la Fig. 1 mais il y a 150 Millions d'années, avant la collision entre les deux blocs. L'océan séparant les blocs subductait sous celui situé plus au nord, produisant le magmatisme daté par cette étude. Jusqu'à un certain point ce modèle représente un analogue du système de subduction actuellement actif en Egée ou dans les Andes. La taille de l'océan est inconnue.

Contents

Introduction

One of the aims of this work is to constrain better the ultra-high-pressure-metamorphism (UHPM) mechanisms, ironically almost without studying the UHP rocks themselves. Indeed, one of the first-order problems in an orogenic belt is the characterization of the terranes involved and the identification of the suture(s) separating crustal blocks: these are key information for large-scale paleo-reconstructions. In addition, the structural relationships between the terranes involved in the collisional processes and the eventual UHP relicts may provide first order inputs to exhumation models of subducted rocks. The determination of basement protolith ages on both sides of a presumed suture can verify the existence of different terranes. If the different basements recorded clearly different magmatic evolutions, there is a high probability that they belong to distinct terranes.

Since the recent discovery of metamorphic micro-diamonds and other evidences for deep subduction of both oceanic and sedimentary rocks in Northern Greece (Kostopoulos *et al.* 2000; Mposkos & Kostopoulos 2001; Kostopoulos *et al.* 2003), the Rhodope Massif (northern Greece and southern Bulgaria) gained more attention in the geologic community. Many studies concentrate on the UHP rocks but the UHP localities are isolated outcrops and their overall structural position is obscure. The overall structure and evolution of the Rhodope Massif are still poorly known. This knowledge is needed before any attempt of conceptual or numerical model dealing with burying and exhumation of these rare rocks can be done.

After Burg *et al.* (1990), the structure of the massif is attributed to a continent-continent collision. UHP relicts and eclogites associated with abundant amphibolitic material, alternatively interpreted as tholeiitic with oceanic affinities or arc related (Kolceva *et al.* 1986; Liati 1986; Kolceva & Eskenazy 1988; Liati & Seidel 1996; Barr *et al.* 1999) suggests the existence of a dismembered suture within the massif (Burg *et al.* 1996; Ricou *et al.* 1998). The structural arrangement between the UHP/eclogite relicts and the main units needs refinement to locate more precisely this suture. The geodynamic significance of this suture requires the characterization of the involved terranes to clarify the evolution of the Rhodope Massif in paleo-reconstructions of the Eastern Mediterranean region (e.g. Robertson & Dixon 1984; Dercourt *et al.* 1986; Ricou *et al.* 1994; Stampfli & Borel 2002).

A peculiar feature of the Rhodope Massif are its impressive orthogneiss exposures. This compromises the characterization of terranes by classical stratigraphy. As most of the massif is affected by high grade metamorphism, a distinction based only on geochemical means would be hazardous. This is why we determined protolith ages of orthogneisses which, coupled with field observation, allow to distinguish the major units with different magmatic evolutions.

The samples were collected mainly along two traverses, in order to constrain also the structural relationship between igneous blocks and UHP-HP relicts (see chapter 4). We present protolith-ages of the orthogneisses from the Greek part of the Central Rhodope obtained by zircon dating, through both Pb-Pb evaporation technique and U-Th-Pb SHRIMP spot-analyses (see chapter 5). Zircon minerals have the advantage to be difficult to reset even through high-grade overprints (see chapter 3). Major and trace element whole-rock analyses of a larger sample-set of the gneisses constrain the geodynamic setting of the protolith emplacement (see chapter 6). The geochronological results and structural observations allow a subdivision of the Greek part of the Central Rhodope in distinct terranes (see chapter 8). This subdivision is correlated with the Bulgarian part of the Massif on the basis of published geochronological and structural data. The structural relationships between the crustal blocks and the HP-UHP occurrences are discussed and used to clarify the mode of occurrence of the UHP relicts.

In this thesis, the term terranes will be used in a similar sense as Howell (1989): fault bounded, far travelled individual crustal entity; our modification of Howell's definition is that, here, terrane will refer to igneous or magmatic terrane as defined by their difference in igneous activity age.

Mineral abbreviations are from Kretz (1983).

Chapter 1

Geological setting of adjacent regions

The Rhodope Massif belongs to the Alpine-Himalayan orogenic belt, which extends for more than 11000 Km, from the Pyrenees to South East Asia. In the Mediterranean realm, the collision is due to the northward movement of the African plate since the Mid-Jurassic and its convergence with the European continent. Several blocks, during the Trias, rifted from the south European or Northern Gondwana margins, to be accreted during Cretaceous and Tertiary to the South European margin (e.g. Stampfli & Borel 2002).

The Rhodope Massif represents the link between two branches of the Alpine system: the Hellenides, on the one hand, and the Balkanides on the other. The overall vergence of the Hellenides is towards the SSW, whereas the Balkinides are characterized by northward thrusting (Fig 1.1 and 1.2). At the risk of oversimplification, this section presents shortly the adjacent areas to the Rhodope, mostly on the Greek mainland and Bulgaria, in order to give an overview to who might be not familiar with the complex geology of the Eastern Mediterranean.

The Hellenides

The Southern part of the Aegean domain is the present location of a north-directed subduction, below Crete, giving rise to the active volcanism of the Aegean arc. The African plate is drifting northward and consequently, the Eastern-Mediterranean oceanic crust subducts below the European margin. The past geodynamic evolution of the Aegean is characterized as well by north-directed subductions, since at least the Jurassic. This consumption of oceanic crust gave birth to the Hellenides orogen by accretion of micro-terranes due to closure of the neo-Tethys Ocean and related marginal oceanic basins.

The Hellenides is a complex orogenic belt trending NNW-SSW, with a main vergence towards the SW. Although the structural frame is complicated by intense Oligo-Miocene extension, the belt is classically divided in units separated by NNW-SSE trending thrusts (Fig. 1.2; e. g. Papanikolaou 1997). An example of the first order evolution of the Hellenides is summarized by the model of Ricou *et al.* (1998) in Fig 1.3. The overall picture is that the collision started earlier in the internal domain of the Hellenides (Rhodope, Serbo-Macedonian, Vardar and Pelagonian) than in the external (Pindos, and External Hellenides Platform). The distinction between internal and external Hellenides is classically justified by the fact that the external Hellenides have not been affected by Cretaceous compression and metamorphism whereas the internal Hellenides suffered an eoalpine metamorphic and deformational event (e.g. Brunn 1960).

External Hellenides Platform

It comprises the Mesozoic carbonate sequences of the Ionian, Gavrovo, Tripolis zones and their metamorphic equivalent, e.g. in Crete. The sedimentary series are made of Late Paleozoic to Upper Eocene-Oligocene rocks (e.g. Papanikolaou 1997; de Bono 1998 and references therein). This domain

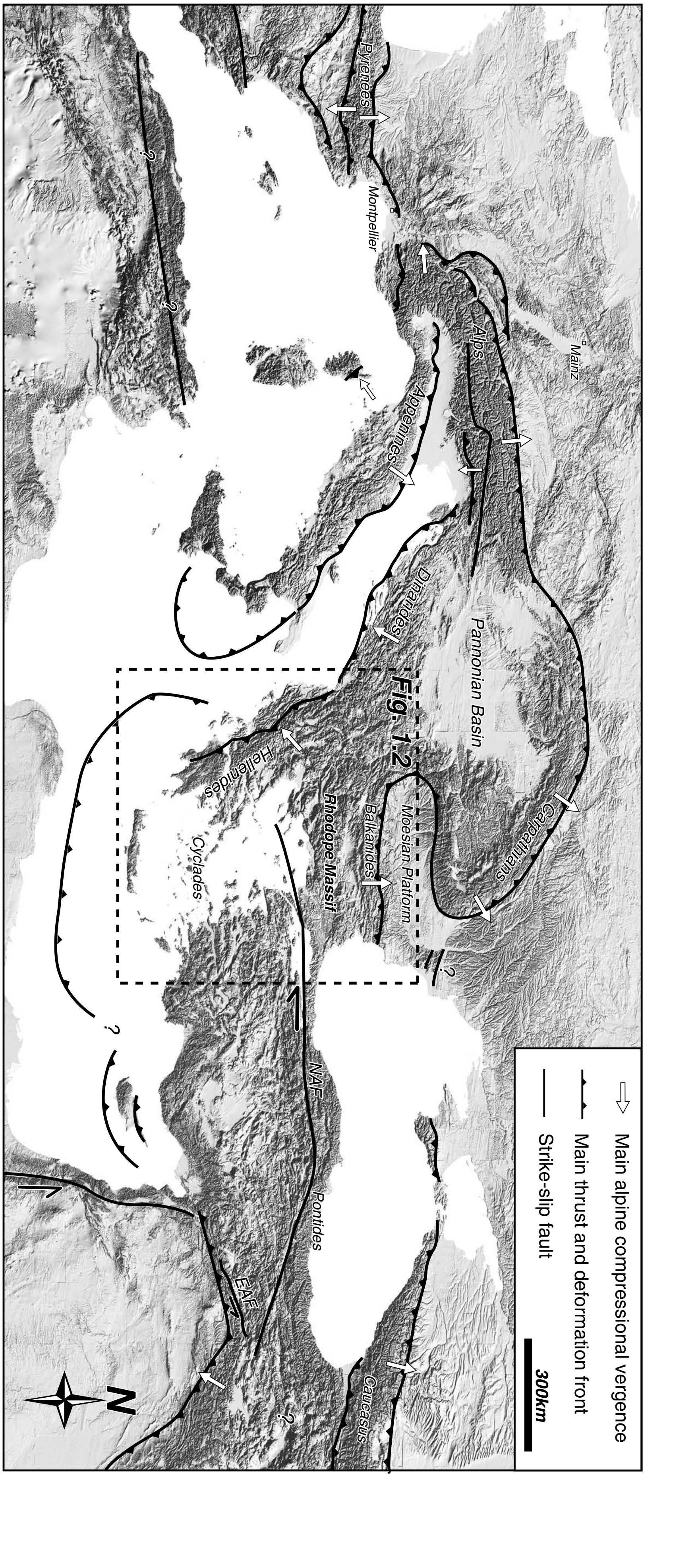

Fig. 1.1.
Digital elevation model of the Mediterranean region extracted from GTOPO30 database (geographic projection). The major deformation fronts are shown with their overall vergence. Mainly from Cavazza *et al.* (2004), modified. Note that the Rhodope massif is located between two divergent orogenic domains, the Balkanides and the Hellenides.

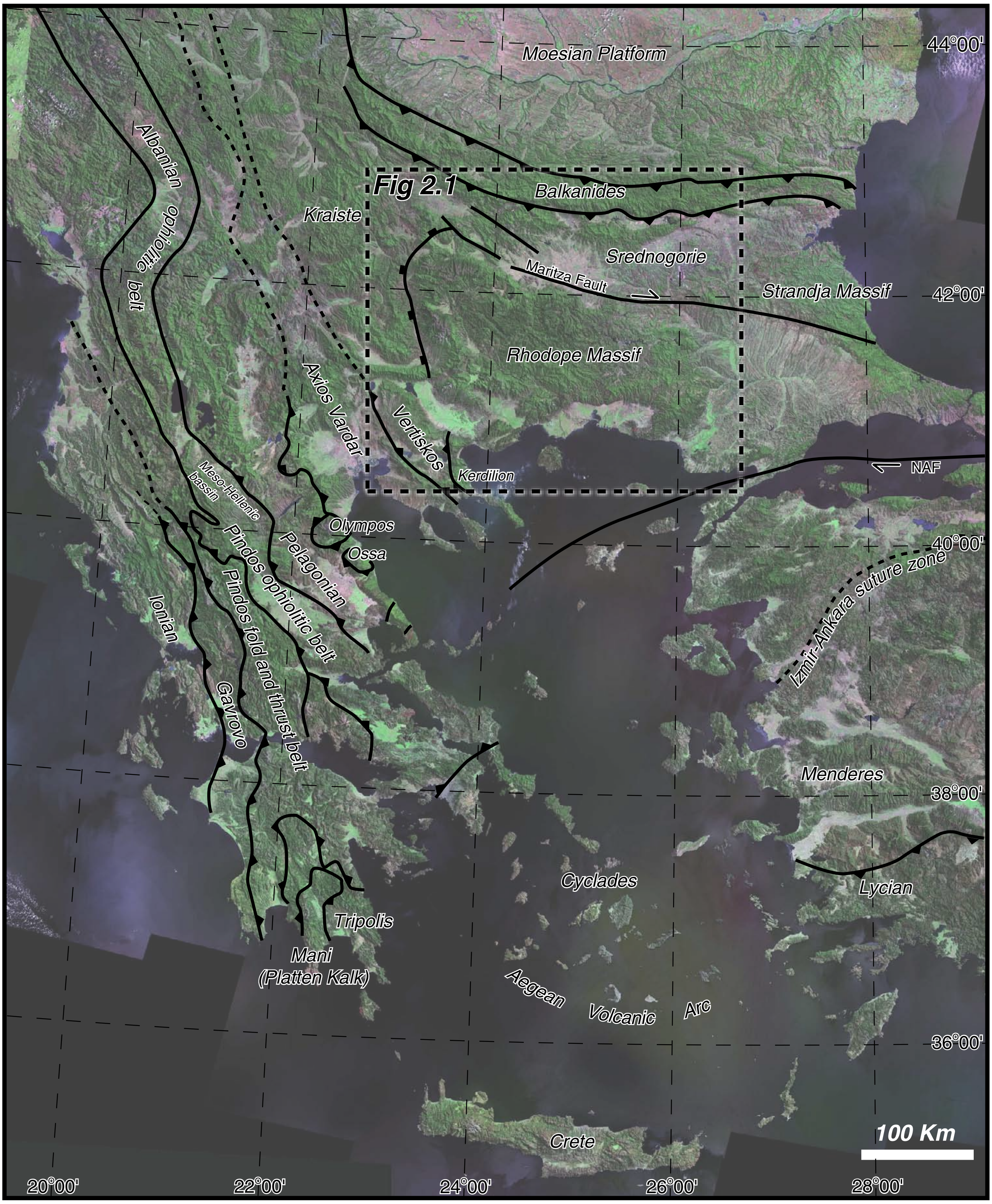

Fig. 1.2.
The Hellenides and Balkanides in a superposition of false colour Landsat 7 mosaics and shaded relief image from SRTM90 database (UTM projection). The main structural units are located (compiled after Bornovas & Rondogianni-Tsiambaou (1983), Papanikolaou (1997), Robertson & Shallo (2000), Jolivet *et al.* (2004), Neumann and Zacher (2004), Vavassis (in de Bono 1998). Crete and Cyclades are not detailed.

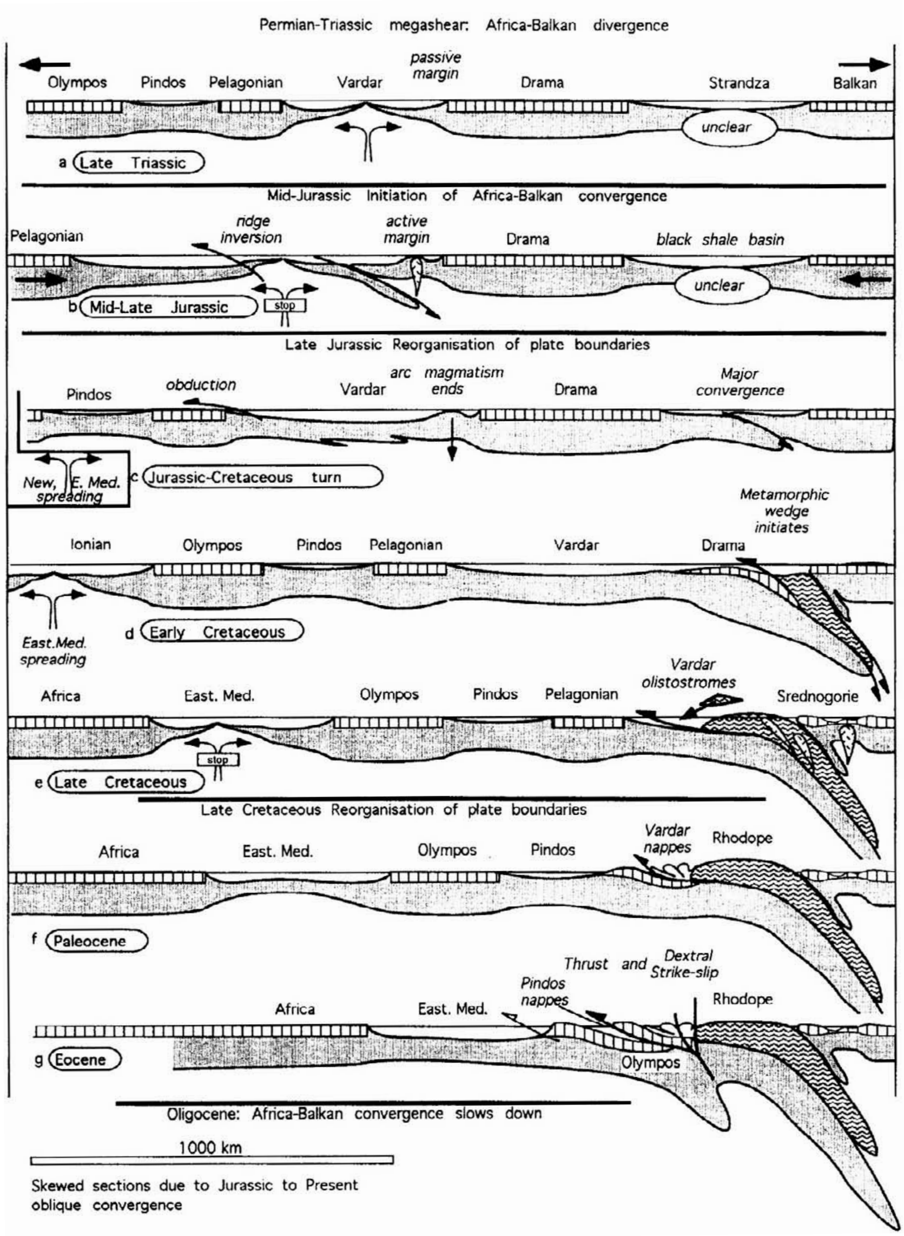

Fig. 1.3.
Evolutionnary model of the Rodope in the frame of the Hellenides during the Mesozoic and Cenozoic by Ricou *et al.* (1998). Note the collision of several terranes and the propagation of the accretion from north to south during the convergence between Africa and Europe.

is characterised by carbonatic sequences from Permo-Triassic to Upper Eocene overlying a poorly known Cambrian basement (Romano *et al.* 2004). The Ionian and Gavrovo zones, separated by thrust planes, can be distinguished also by their difference in stratigraphic records: The Ionian zone has deeper facies than the Gavrovo (see the elegant compilation of the stratigraphic records of the different zones by de Bono 1998). This carbonatic sedimentation is replaced in Oligo-Miocene by flysch inputs, due to the incorporation of this domain in the Hellenic orogen.

The equivalent of this platform is found in Crete and the southernmost Peloponnesus (e.g. Plattenkalk Unit), where it underwent metamorphism under HP-LT conditions (ca. 8-10 Kbar, 350-400 °C) during the Early Miocene ,between 20 and 25 Ma (Jolivet *et al.* 1996; Ring *et al.* 2001 and references therein). Further North, the basal unit of the Cyclades is also thought to be the equivalent of the external platform (Ring *et al.* 2001 and references therein). In the mainland the platform is overthrusted by the Pindos fold and thrust belt along a NE dipping contact.

Pindos

The Pindos thin skinned fold-and-thrust belt with its NNW-SSE trend and WSW vergence (e.g. Skourlis & Doutsos 2003) involves a sedimentary series from Trias to Eocene, in wich Jurassic radiolarite levels indicate a deep marine environment (e. g. Degnan & Robertson 1998).

An early Cretaceous flysch (the first Pindos flysch) is also present, its deposition is most probably coeval with the first thrusting event in the Vardar zone (Aubouin 1959 and Aubouin *et al.* 1960). Tertiary flysch sedimentation in this domain started in Paleocene-Eocene (e. g. Degnan & Robertson 1998), i.e. earlier than in the External Platform, indicating a progression of flysch deposition from internal to more external domains, following the general polarity of the Hellenides.

The Pindos fold-and-thrust belt is thrusted by a Jurassic ophiolitic sequence: e.g. the Pindos and Vourinos ophiolites, which are built of peridotites, mafic extrusives and metamorphic sole (e. g. Bebien *et al.* 1980). Unfortunately, the north east contact of this unit is overlain by the Meso-Hellenic Trough (a Neogene flysch) that hides possible hints for the location of the Pindos ophiolitic units root zone, source of an intense debate. For example, according to Robertson (2002) the Pindos ophiolites represent the trace of an "in situ" suture; instead Bonneau (1982) or van Hinsbergen *et al.* (2005), who accept the concept of the Pindos fold-and-thrust belt as representing a deep basin, the Pindos ophiolites are klippes originated further north, in the Vardar zone.

The Pelagonian Zone, Olympos-Ossa and Cyclades

The Pelagonian Zone, the westernmost unit of the Internal Hellenides, is mainly built of a Permo-Carboniferous igneous basement (Vavassis *et al.* 2000; Reischmann *et al.* 2001; Anders *et al*. 2002) overlain by a sedimentary sequence from late Permian to Jurassic with occurrences of precambrian basement (Anders *et al*. 2005).

Olympos and Ossa units appear as tectonic windows below the Pelagonian terrane. The Olympos and Ossa window rocks suffered a HP-LT metamorphism (5-8 Kbar, ca. 200-300 °C; Schermer 1990) as the Cyclades blueschists, of which they represent the mainland equivalent. The precise age of this blueschist metamorphism is debated; It should range from Paleocene to mid-Eocene (e. g. Maluski *et al.* 1987; Schermer *et al.* 1990; Bröcker *et al.* 1993) but could possibly be Cretaceous (Lips *et al.* 1998; Bröcker & Enders 1999). The conditions reached during this subduction event are T = ca. 450–500 °C, P = ca. 15±3 kbar (e.g. Bröcker *et al.* 1993). However there is a common agreement that the Pelagonian basement recorded metamorphism in Late-Cretaceous time. This early metamorphism could be due to the overthrusting of the Pelagionian by slices of ophiolitic rocks of Vardar origin in Cretaceous time.

The Cyclades recorded similar history as the Olympos and Ossa massif, but are more affected by subsequent extension and associated greenschist facies retrogressions which started at about 20 Ma (Lister *et al.* 1984; Gautier *et al.* 1999 and references therein). Indeed, the extension in the Olympos massif is mostly accommodated by brittle movements without associated metamorphic retrogression (Schermer 1990 and 1993). The Cyclades are the locus of intense extensional tectonics since 20 Ma, mostly trending N-S along north dipping detachments (Gautier & Brun 1994; Jolivet *et al.* 1994; Gautier *et al.* 1999); in fact the whole Aegean region (s.l.) is extending since the Miocene (Crete, Menderes, Rhodope,…).

Olympos and Ossa are classically correlated with the Ionian platform (e.g. Schermer 1993; Papanikolaou 1997; Ring *et al.* 2001) but also with Pindos basin (Bonneau 1982). Correlations between different units in the Hellenides are often speculative and still matter of debate (see Jolivet *et al.* 2004).

The Vardar Zone

The Vardar zone extends from Thessaloniki region up to Zagreb region in Croatia. It represents a ca. 1000 Km long Mesozoic ophiolitic belt, making it a probable root zone of a suture. Mercier (1968) divides the Greek Vardar domain in three zones, from the West to the East: Alompias, Paikon and Peonias.

The Paikon Massif is interpreted by Brown & Robertson (2004) as remnant of a Mid-Late Jurassic magmatic arc built above the NE-ward subduction of the main Vardar Ocean. On the other hand, for Ricou *et al.* (1998 and references therein) it represents a tectonic window, the core of which has Olympos affinities. In their view, the Guevgueli, Vassilika and Kassandra Gulf units represent a Jurassic magmatic arc, established above the subducted Vardar Ocean. This arc is covered by Late Jurassic limestones.

Towards the West, the Vardar ophiolites obduct the Pelagonian zone SW-ward: this took place during Late Jurassic or Early Cretaceous according to Bébien *et al.* (1980) and Bonneau (1982), after the Late-Cretaceous according to Ricou *et al.* (1998). Towards the East, the contact with the Serbo-Macedonian Massif is a dextral strike-slip zone that reworked a higher grade contact in greenschist facies conditions (Ricou *et al.* 1998). According to Ricou *et al*. (1998), parts of the Vardar zone represent Rhodopian klippes and a Cretaceous olistostromic flysch which bears Kimmeridgian blocks and is covered by Late Eocene.

It is worth to notice that radiometric ages from the ophiolites of Pindos, Vourinos, Vardar and Crete, either on their metamorphic sole or on comagmatic rocks, are systematically Mid- to Late-Jurassic (see Liati *et al.* 2004 and references therein).

The Serbo-Macedonian Massif

The so-called Serbo-Macedonian Massif is divided in two units since the work of Kockel (1971). The Vertiskos (to the West) and the Kerdilion (to the East) are separated by a large amount of metabasics; the Volvi complex of Dixon & Dimitriadis (1984) interpreted as part of a suture zone by Himmerkus *et al.* (2005). The Vertiskos is a gneissic complex composed of gneisses, marbles, schists and amphibolites. On the other hand, the Kerdilion consists of migmatitic gneisses, marbles, and minor amphibolites. The whole massif records a ductile shearing with a south-westward overall flow which took place during development of a crustal-scale nappe complex (Burg *et al.* 1995).

An important work related to the present study is the dating of the protolith of orthogneisses in the Vertiskos Unit by Himmerkus *et al.* (2003). The orthogneiss from the Vertiskos unit yielded Silurian protolith ages that this unit represent actually a terrane with no rhodopian affinities (see later).

The Balkanides

The Balkanides (Bulgaria) are an orogenic belt which is less studied and constrained compared to the Hellenides. The Balkanides overthrusted northward the Moesian platform along south dipping contacts. The Moesian platform consists of a Mesozoic and Cenozoic sedimentary sequence overlaying a Paleozoic or Precambrian basement (Hsü *et al.* 1977) that recorded also Permo-Carboniferous magmatic activity (Carrigan *et al.* 2003; Cortesogno *et al.* 2004). The tectonic evolution of the Balkanides is complicated, several compressive phases are identified (Ivanov 1988): Albian, end of Late Cretaceous and mid Eocene. There is no evidence for a suture zone within the Balkanides.

The Srednogorie zone presents a sequence resembling an aborted rift, with an intensive Late Cretaceous magmatic activity (e.g. Ciobanu *et al.* 2002). It has been interpreted by Boccaletti *et al.* (1974) as a remnant of a subduction-related volcanic arc built above the Vardar subduction. The Rhodope Massif is separated from the Srednogorie by a deep seated wrench fault, the Maritza fault, which displacement and age of activity is not described anywhere in the literature.

Chapter 2

The Rhodope and its geological setting

This chapter gives a brief review of the available information about the massif in the sometimes difficult to find Rhodopian literature.

Geographically, the Rhodope Massif represents the mountainous area in northern Greece and southern Bulgaria (Fig. 2.1). This high-grade massif has long been considered as a Precambrian or Hercynian continental block, surrounded by the two alpine orogenic branches described in the previous chapter: the Hellenides and the Balkanides. Since the work of Kronberg (1977) and Papanikolaou (1981), the possibility that at least a part of the observed deformation is Alpine (*s.l.*) is considered. We had to wait for the works of Burg *et al.* (1990 and 1996) and Ricou *et al.* (1998) to finally get the proof that the observed deformation is Alpine (*s.l.*). These publications are until now the only synthetic contributions describing and interpreted the massif as a whole.

The pre-Tertiary lithologies of the massif are mainly marbles, orthogneisses, migmatites, micaschists and amphibolites. The Rhodope is located between the Moesian platform to the North and the Serbo-Macedonian Massif to the West (Fig. 1.2). The contact with the Moesian platform is marked by an Early-Cretaceous and Tertiary North-verging fold-and-thrust belt, the Balkanides and Srednogorie Zone (e.g. Hsü *et al.* 1977; Ivanov 1988), interpreted by Boccaletti *et al.* (1974) as a back-arc thrust system. The Srednogorie Zone is the locus of intense Late Cretaceous magmatic and effusive activity, interpreted generally as subduction related (Ciobanu *et al.* 2002 and references therein). The Rhodope Massif is separated from the Srednogorie Zone by the Maritza wrench fault (Burg *et al.* 1996) and from the Serbo-Macedonian Massif by a top-to-the-SW Tertiary detachment (the Strymon valley detachment: Dinter & Royden 1993; Sokoutis *et al.* 1993; Dinter *et al.* 1995; Lips *et al.* 2000). This extensional tectonics, also visible in the core-complex structures of the Arda dome, probably reactivated pre-existing thrust planes (e.g. Burg *et al.* 1996; Ricou *et al.* 1998; Moriceau 2000). The massif exhibits a widespread top-to-the-SW upper amphibolite to greenschist facies deformation, except in the upper-most unit, the Asenica Unit, where a synmetamorphic top-to-the-ENE shearing is recorded (Burg *et al.* 1990).

On the basis of radiometric ages and chronostratigraphic criteria, Burg *et al.* (1996, and references therein) infered a Late Mesozoic-Early Cenozoic age for the main metamorphism and top-to-the-SW ductile shearing. Considering the high strain along thrust zones and the presence of eclogitic and mafic material with oceanic affinities, these authors interpreted the overall structure as a nappe stack, resulting from continent-continent collision between an Upper and Lower Terrane.

The Central Rhodope Massif shows evidences for HP or UHP metamorphism in metasedimentary (Mposkos & Liati 1993; Mposkos & Kostopoulos 2001; Kostopoulos *et al.* 2003; Perraki *et al.* 2004) and mafic lithologies (Kolcheva *et al.* 1986; Liati & Seidel 1996; location shown in Fig.

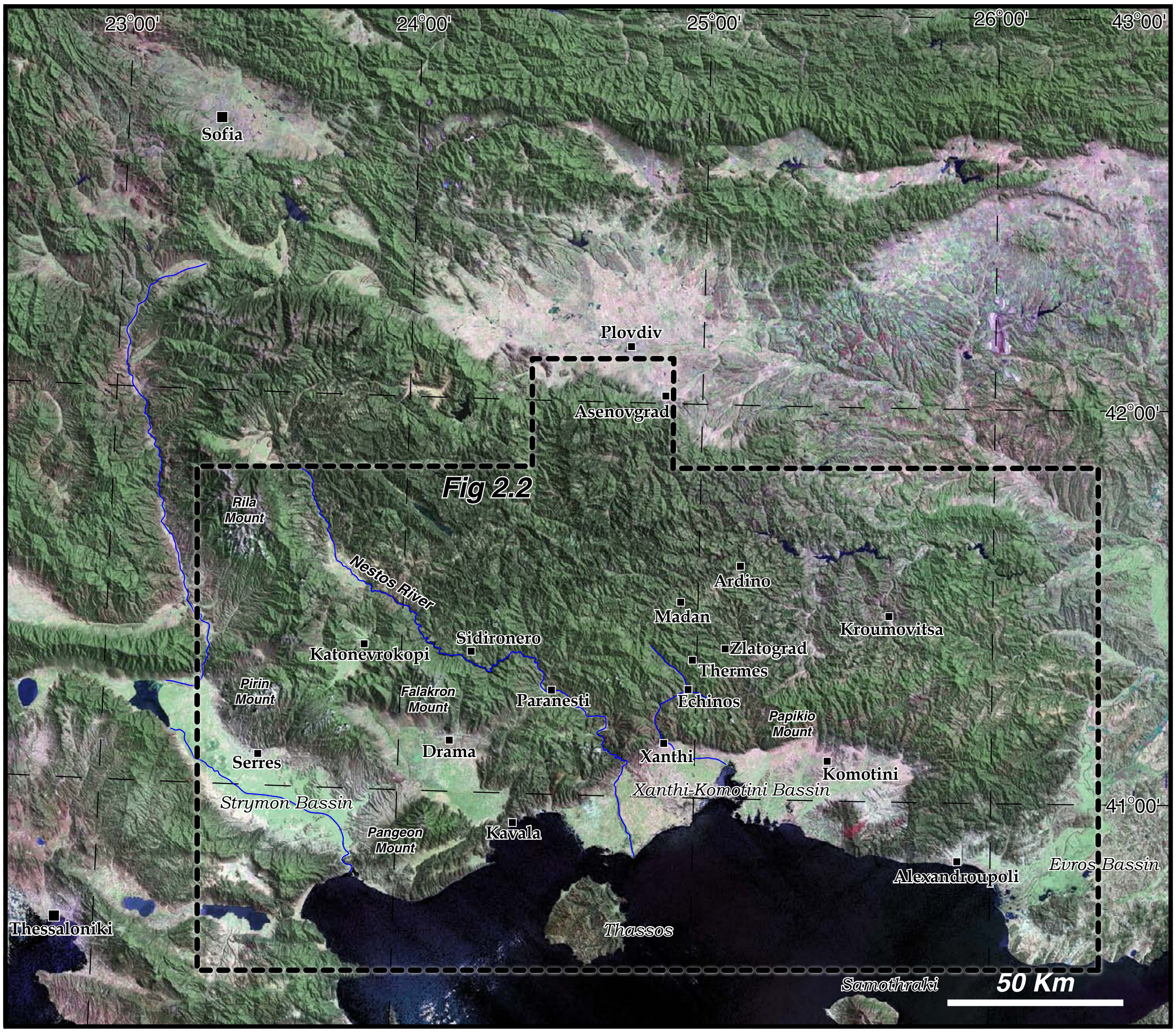

Fig. 2.1.
Superposition of false colour Landsat 7 mosaics and shaded relief image from SRTM90 database of the Rhodope region, illustrating the morphology and the main geographic features discussed in the text (UTM projection).

2.2 and 2.3). In the Eastern Rhodope, the overlaying Kimi complex yielded also UHP indicators (Mposkos 2001; Mposkos & Kostopoulos 2001; Perraki *et al.* 2004; Fig. 2.2). It is worth noting that the Asenica unit also experienced HP metamorphism, with pressures around 13 Kb (Guiraud *et al.* 1992). In the central domain, the HP-UHP rocks are generally associated with amphibolites (± Grt) and ultramafic lenses (Liati 1986; Kolcheva *et al.* 1996; Barr *et al.* 1999; Kostopoulos *et al.* 2003). The protoliths of the amphibolites have been referred to be tholeiitic basalts (Kolceva *et al.* 1986; Liati 1986; Kolceva & Eskenazy 1988; Barr *et al.* 1999), on the basis of their trace element concentration, notably Zirconium.

In the Central Rhodope, the age of the HP-UHP event(s?) is still controversial. Ages interpreted as representing the HP stage range from 40 Ma up to 180 Ma. Liati & Gebauer (1999) reported a SHRIMP age at 42.2 ± 0.9 Ma on zircons from an eclogite, close to Thermes, 25 Km north of Xanthi (Fig. 2.2). Further south, close to Xanthi, the same authors dated metamorphic-rims at 148.8 ± 2.2 Ma in zircons from Grt-Ky metasediments, with important Pb-loss around 40 Ma (Liati 2005). Further west a zircon rim in amphibolized eclogite yielded an age

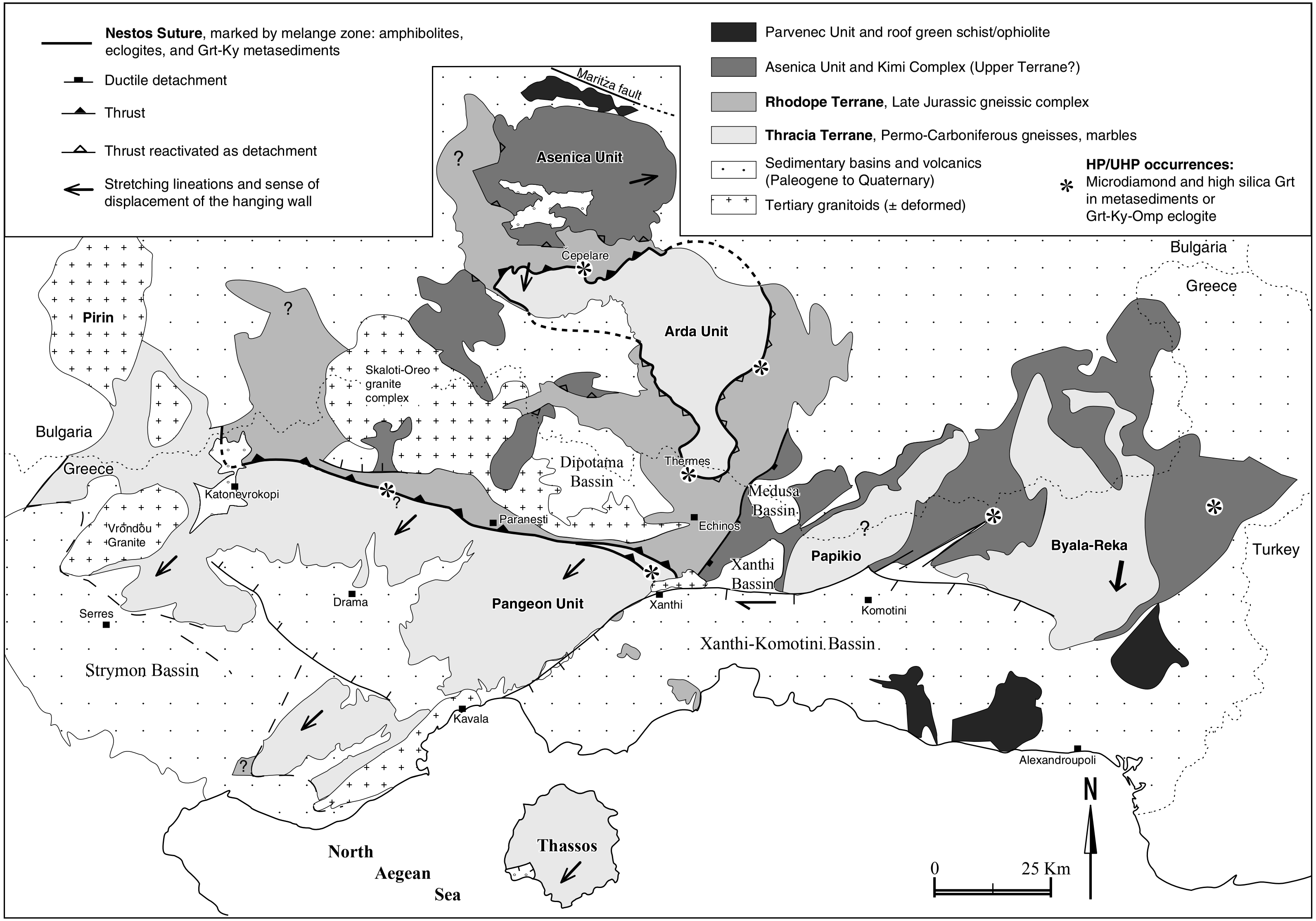

Fig. 2.2.
Sketch-map of the Rhodope Massif illustrating the subdivision defined in this study. Compilation after Kronberg (1969), Bornovas & Rondogianni-Tsiambaou (1983), Ivanov (1988), Burg *et al.* (1990 and 1996), Ricou *et al.* (1998), Moriceau (2000) and own observations.

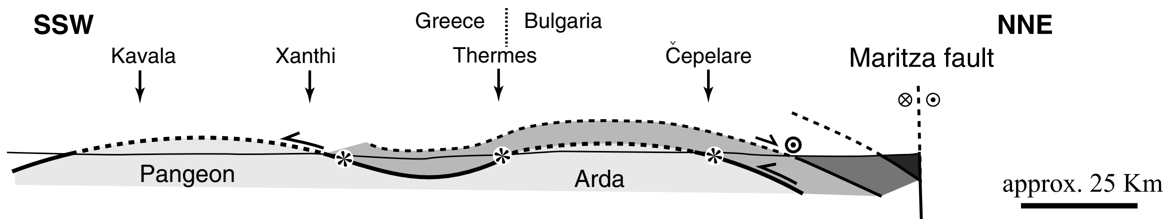

Fig. 2.3.
NNE-SSW idealized cross-section of the Central Rhodope. Note the flat-lying nature of the proposed suture separating the two terranes and its probable rooting below the Asenica Unit at the contact with the Maritza fault. Tertiary intrusives, brittle faulting and sedimentary basins were removed to simplify the scheme.

of 51.0 ± 1.0 Ma. The REE patterns of the dated zircon domains (Jurassic and Early Eocene) show no Eu anomaly and flat HREE profiles. This is why these ages are interpreted as closely approximating HP and UHP stages. This series of ages (40, 51 and 148 Ma) is interpreted as a testimony of repeated subduction and collision of several terranes (Liati 2005). In a UHP Grt-Ky micashist close to Xhanti, Reischmann & Kostopoulos (2002) obtained a Sm-Nd garnet/whole-rock age of 140 ± 4 Ma (interpreted as a cooling age postdating the UHP event), and monazite ages between 185 and 146 Ma (that could represent the UHP stage).

In the Arda Unit (Fig. 2.2), the HT overprint and migmatitization have been dated at 35-37 Ma by U-Pb on monazites (Peytcheva *et al.* 2004; Ovtcharova *et al.* 2004). On the other hand, in the hanging wall, Ovtcharova *et al.* (2004) reported monazite ages ranging between 47 Ma and 52 Ma in migmatitic gneisses. This age difference between the monazites of the footwall and hanging-wall can be a result of the differential exhumation of the two units during extensional tectonics (Ovtcharova *et al.* 2004). A possible heat-source for the HT overprint is the intrusion of Tertiary granitoids, which in our working area constitute the Vrondou and Kavala granites and the Skaloti-Oreo complex (Fig. 2.2). The latter partly hides the early Alpine structures.

Indeed, the whole massif is intensively intruded by presumed Tertiary granitoids (possibly late Cretaceous). Most of the radiometric dating of these rocks is based on K-Ar or Rb-Sr whole rocks. The few reliable age determinations on this granitic suite are the U-Pb dates between 20 and 24 Ma on titanite and zircon from Dinter *et al.* (1995) in the Kavala suite and early Miocene on titanite ($^{206}Pb/^{238}U$) and Ar-Ar on hornblende (Kaufman 1995, in Dinter 1998) in the Vrondou intrusion. The intrusion age of the Skaloti-Oreo granitic complex is poorly constrained; Liati & Gebauer (1999) dated a cross cutting pegmatoid, probably issued from the adjacent granite, close to Sminthi, at 36.1 ± 1.2 Ma (U-Pb SHRIMP on zircon). On the other hand, Soldatos & Christofides (1986) report a Rb-Sr whole-rock date of 87 ± 27 Ma in the Skaloti-Oreo complex, but the geochronological method raise a doubt on the reliability of this age. The Xanthi and Kentavros granites gave K-Ar dates respectively of 30.4 ± 0.6 and 38 ± 0.4 Ma on Hbl (Liati 1986) but the question whether these dates are cooling or intrusion ages is opened (especially considering the similarity between these ages and the Ar-Ar ones in the country gneisses).

The Ar-Ar and K-Ar cooling ages on micas, in the Greek part of the massif, cluster between 35 and 40 Ma in the hanging wall unit (Lips *et al.* 2000 on Mu, Liati 1986 K-Ar on Bt and Mu, Moriceau 2000 Ar-Ar on Bt and Mu). Liati (1986) reported K-Ar on Hbl around 45 Ma but also older ages around 80-95 Ma in “eclogitic amphibolites” (possible excess Ar). In the footwall unit (Pangeon), the cooling ages display a younging up to around 15 Ma towards the SW (Lips *et al.* 2000; Moriceau 2000). This last observation, together with the presence of the overlying Strymon basin, is a good argument in favour of a Tertiary detachment tectonic finalizing the exhumation of the Pangeon Unit. One of the still opened questions is: which part of the deformation is attributable to the detachment tectonics,

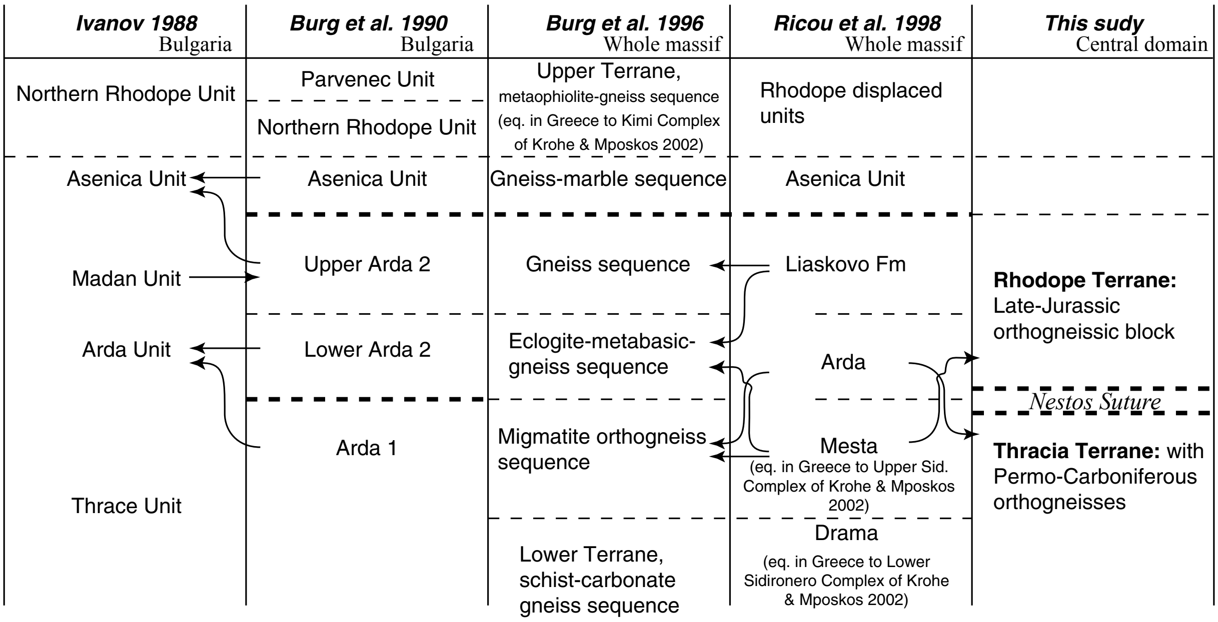

Fig. 2.4.
Correlation between the subdivisions of the Rhodope from previous authors and the one defined in this study. Arrows mean "part of" and thick lines represent the major boundaries. Below the citations, the domains of validity of the subdivisions are reported.

and which to the compressive phase(s?) (Moriceau 2000), since these two phases have similar apparent vergences?

The metamorphic pile is unconformably overlain by continental sediments; the older sedimentation is represented by Maastrichian-Oligocene conglomerates close to Kroumovitsa in south-east Bulgaria (Fig 2.1; Boyanov *et al.* 1982; Goranov & Atanasov 1992 in Burg *et al.* 1996). Marine sedimentation took place in Mid-Late Eocene time, as evidenced by nummulitic limestones (e.g. Xhanthi Bassin; Innocenti *et al.* 1984; von Braun 1993). An important Late Eocene to Early Oligocene volcanic activity, mostly rhyolitic, is associated with this sedimentation (e.g. Dipotama and Medusa basins; e.g. Innocenti *et al.* 1984).

Until now, the structural subdivisions of the Rhodope Massif were relying on structural criteria (e.g. Burg *et al.* 1996; Ricou *et al.* 1998) or metamorphic facies distinction (e. g. Krohe and Mposkos 2002). We propose a new method based on orthogneiss protolith age determination, and give a new geodynamic meaning to the previously defined units, thus we suggest a different subdivision of the central domain of the Rhodope Massif. The correlations with earlier subdivision are shown in Fig. 2.4.

Previous dating of the orthogneisses' protolith

The protolith age of the basement orthogneisses of the lower part of the tectonostratigraphic pile are attributed to the Permo-Carboniferous. Peytcheva *et al.* (1995, 2004) and Ovtcharova *et al.* (2002) reported zircon U-Pb ID-TIMS (Isotope Dissolution Thermal Ionization Mass-Spectrometry) ages in the Central and Eastern Bulgarian Rhodope between 300 and 310 Ma (Fig. 5.9). On Thassos Island, Warzenitz *et al.* (1994) reported a protolith age around 360 Ma. Recently, though, some orthogneisses from the intermediate units yielded Early Cretaceous and Late Jurassic intrusion ages (Turpaud & Reischmann 2003; Ovtcharova *et al.* 2004, ages reported in Fig. 5.9). These data raise a question about the structural relationships between orthogneisses of different age. They question as well the significance of these intrusions in the geodynamic evolution of the massif.

Chapter 3

Analytical techniques

In this chapter the procedures followed for zircon separation, cathodoluminescence (CL) imaging, dating and geochemical analyses are described. Some principles of zircon dating, that might help readers not familiar with this method, are also presented.

Why zircon?

Zircon is a Uranium-bearing accessory mineral widely used for isotopic dating. One of its main advantages is its high resistance to alteration and resetting by metamorphic overprint. As the closure temperature (although disputable concept) to Lead loss of zircon is around 900 ^{o}C for an effective diffusion radius of 100 μm (Cherniak & Watson 2000), in igneous rocks the U-Pb or Pb-Pb ages are generally interpreted as crystallization ages. A consequence of zircon's resistance is the common presence of inheritance trapped in single crystal (inherited cores). However, this inconvenience can be handled by careful study of zircons internal structure by CL imaging.

Our aim was to distinguish the main units in the Rhodope by their difference of orthogneisses' protolith ages. To obtain such crystallization or emplacement ages, i.e. protolith ages of the orthogneisses, zircon was the preferred mineral because of its common occurrence in the studied rock-type (granitic gneisses) and for its resistance to isotopic resetting. As we have seen, the Rhodope is a high-grade massif and such resetting has to be expected for other isotopic systems such as Sm-Nd, Rb-Sr or K-Ar, which are known to have lower closure temperatures than the U-Pb system in zircon.

Zircon separation

Zircons were separated by crushing whole-rock samples of 5-10 Kg each, and sieving to fraction <0.5 mm in size. A first removal of the lightest fraction has been achieved by Wilfley table separation. Then magnetic and heavy-liquid separations (bromoform and methylen-iodide) were performed to obtain unmagnetic fraction with density above 3.3 $g*cm^{-3}$. Zircons were finally hand-picked under binocular microscope. As the purpose of the study was to obtain intrusion ages, only euhedral zircons without visible inclusions or cores were selected for dating.

Cathodoluminescence imaging

CL-imaging is a powerful tool to reveal the internal structure of the zircons and a key step for age-interpretation in zircon geochronology. This technique allows the identification and characterization of growth or annealed domains, and therefore a direct interpretation of the obtained ages. The cathodoluminescence results from the interaction between a primary electron beam and the crystal lattice. The electron beam brings the irradiated lattice in an excited state, it is the recovery of the unexcited state that releases the cathodoluminescence intensity.

Cathodoluminescence imaging: a tool to decipher zircons internal structure

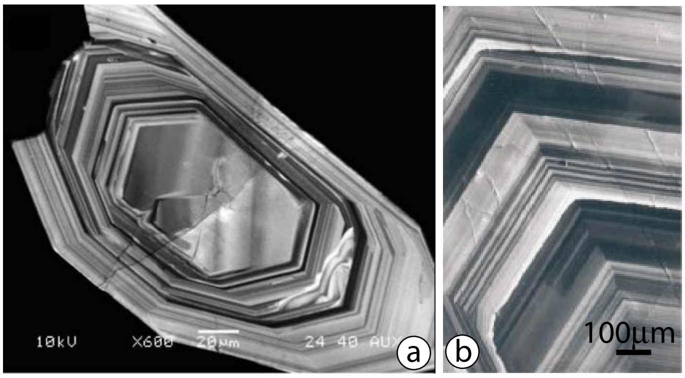

Typical high frequency oscillatory zoning. Such zoning is due to heterogeneous distribution of trace elements and difference in degree of crystallinity.
a: from Ireland & Williams (2003)
b: close up from Corfu *et al.* (2003)

Example of core-bearing grain. Note the metamorphic stucture of the core (representing most of the interior of the crystal). This core is overgrown by a thin igneous domain. From P. Kinny (unpublished data, in Corfu *et al.* 2003), grain size between 70 and 250 µm

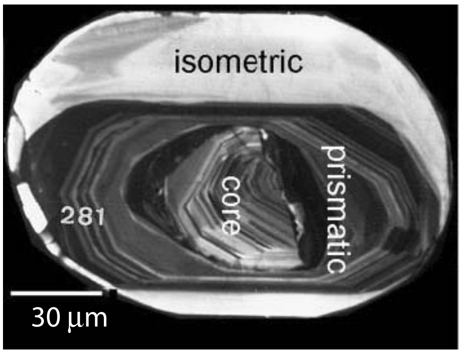

Example of complex structure showing core and magmatic overgrowth followed by metamorphic overgrowth. From Vavra *et al.* (1999)

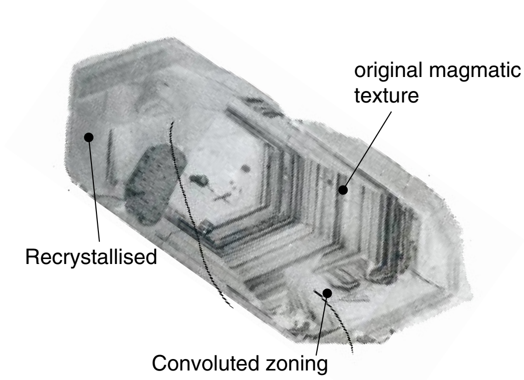

Example of magmatic grain with partial recrystallisation. Note that the recrystallized outer rim, partly preserves the igneous patern (Corfu *et al.* 2003)

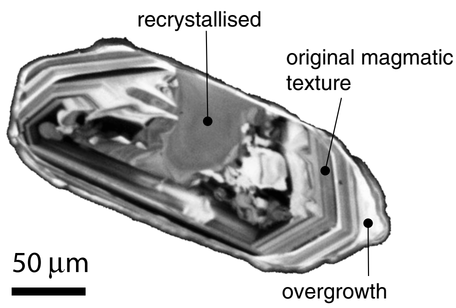

Example of partly recrystallized grain with limited overgrowth. Sample RH96, this study.

Zircon internal stucture can be difficult to interpret! Example of convoluted zoning from Pidgeon (1998). Grain lenght between 200 and 300 µm. Note that here the internal stucture is revealed by HF eatching prior to imaging with a reflected light microscope.

Igneous zircons generally display typical high frequency oscillatory zoning due to heterogeneous distribution of elements, particularly trace elements (see page 18). The presence of these elements in the crystal lattice has an influence on the degree of crystallinity, and therefore on the cathodoluminescence brightness/intensity. Indeed, the CL intensity is closely related to the lattice degree of order (Hoffman & Long 1984; Kempe *et al.* 2000; Nasdala *et al.* 2002). This is why thermally recrystallized zircons show often bright CL rims, as recrystallization leads to removal of trace elements from the crystal lattice (Gebauer 1990; Vavra *et al.* 1999; Rubatto & Gebauer 2000; Geisler *et al.* 2001; see page 18).

A study of zircon internal structures of the zircon population of each sample has been achieved; this is particulary important for the samples dated by the Pb-Pb technique, since in this case the measured grains cannot be studied in CL prior to analysis. On average, 30 zircons from the separate of each sample were mounted in epoxy; the mounts were abraded and polished to almost the half-section of the grains. CL images were taken at an acceleration voltage of about 20 kV with a JEOL JXA-8900RL superprobe at the University of Mainz (Germany) and at the MPI for Geochemistry of Mainz on an Hitashi S450 at an acceleration voltage of about 15 kV. Fig. 5.1, 5.7 and appendix 2 show representative CL images of the dated zircon populations.

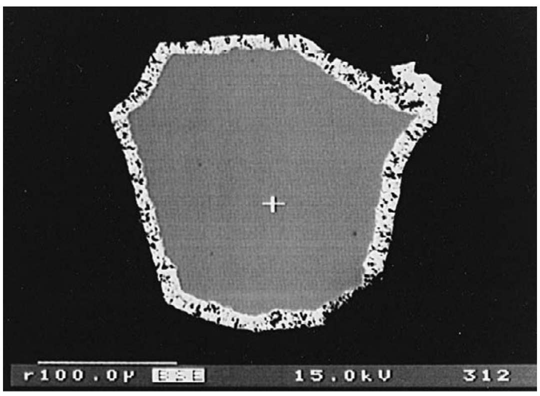

Fig. 3.1.
BSE image of a zircon fragment after one step of heating from Dougherty-Page & Barlett (1999). Note the transformation of the zircon in porous baddaleyite progressing inward from the crystal margins.

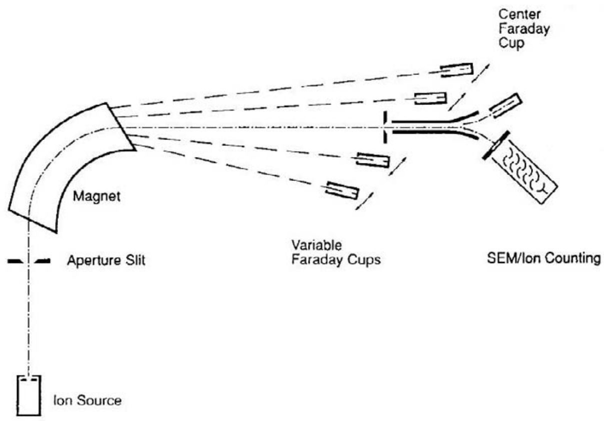

Fig. 3.2.
MAT 261 design showing the dispersion of the masses through the magnet. Along this study only the central fixed SEM has been used (modified after de Laeter 1998).

Pb-Pb dating

The Pb-Pb technique is a zircon dating technique developed mostly by Kober (1986, 1987). It allows age-determination by measure of the lead isotopic-ratios of single zircon grains without pre-treatment or chemical dissolution of the mineral and separation of the elements.

Each single-zircon suitable for age determination is wrapped in a boat-shaped Re filament (EVA filament) facing a flat Re filament (IONI filament), at a distance from the IONI of less than 1 mm, according to the methods described in Kober (1986 and 1987). Once inside the mass-spectrometer, the IONI filament is heated up to ca. 1500 °C (by application of electric potential, temperature checked by pyrometre), for cleaning purpose, then cooled down to ca. 1200 °C. The EVA filament is then slowly heated and kept at a temperature of 1350 °C in order to “clean” the zircon grain, i.e. for the removal of the external part of the grain (Ansdell & Kyser 1993, Fig. 3.1), more subject to lead-loss and metamorphic overprint. As the IONI filament is kept at high temperature during this cleaning, no Pb from such domain is deposited on it. Following this cleaning procedure, the current trough the IONI filament is brought back to zero and the EVA filament heated up to 1500°C. This elevated temperature allows the evaporation of ion compounds from the zircon crystal. These ions are deposited on the cold IONI filament facing the EVA filament. It is from this deposit that the isotopic ratios are measured. Thus, in principle, only the lattice-supported lead is deposited on the IONI filament. When no signal is detectable from the EVA filament, it is cooled down and the IONI filament is slowly heated until the signal reaches an intensity suitable for measurement.

The ions produced by heating of the IONI filaments are accelerated inside the ion source by potential difference of about 10000 kV. These ions are then separated by mass inside the magnet as shown in Fig 3.2. The masses 204, 206, 207 were scanned in dynamic mode on a Finnigan MAT 261 mass-spectrometer at the Max Planck Institute for Chemistry Mainz (Germany) with a secondary electron multiplier. Measured Pb isotopic ratios ($^{207}Pb/^{206}Pb$ and $^{206}Pb/^{204}Pb$), together with 2 σ errors and apparent ages, are reported in appendix 3. Common lead (Pb_{com}) correction follows the two-stage model of Stacey & Kramers (1975). Error due to mass fractionation is neglected (in the range of 0.1%, Kober 1987). The main source of error is the low signal and consequent poor counting statistics on the 204 mass due to the generally low Pb_{com} content. The final error on each single age takes into account the analytical error of both $^{207}Pb/^{206}Pb$ and $^{206}Pb/^{204}Pb$ values. The error on the $^{206}Pb/^{204}Pb$ measurements is empirically propagated to the final apparent age of each zircon, by calculating the maximum and minimum ages resulting from the extreme acceptable values of the $^{206}Pb/^{204}Pb$. These extreme values are calculated by adding or subtracting the 2 σ error of the $^{206}Pb/^{204}Pb$ to its mean. The weighted average Pb-Pb ages for each sample were calculated at the 95% confidence level with Isoplot/Ex of Ludwig (2003). Results are shown in Fig. 5.1 and 5.7 together with relative cumulative probability plots and representative CL images of the zircons.

In order to obtain geologically meaningful ages, some measurements have been rejected, notably those showing unstable isotopic ratios during the analysis. Our philosophy was also to reject the measurements with $^{204}Pb/^{206}Pb > 0.0005$ (except for samples RH123 and RH87). Indeed, such high Pbcom can lead to large errors on the final age. Measurements with errors on the apparent age above 20 Ma have been also rejected (except in the case of sample RH123). Zircons statistically off the mean age population, if not reproducible, are interpreted as core bearing if older, or as having experienced non-contemporaneous Pb-loss if younger (appendix 3).

An alternative age-calculation procedure is to plot the measured $^{207}Pb/^{206}Pb$ vs. $^{204}Pb/^{206}Pb$ and to calculate a regression line. The intercept of the regression line on the Y-axis gives the $^{207}Pb/^{206}Pb$ of zircons with virtually no Pb_{com} component. Appendix 3 gives the intercept ages calculated with Isoplot/Ex (Ludwig 2003) for each sample. This procedure is particularly important for the low $^{206}Pb/^{204}Pb$ measurements, since it allows checking the validity of the common lead correction. Fig. 5.8 gives the plot of measured $^{207}Pb/^{206}Pb$ vs. $^{204}Pb/^{206}Pb$ as well as the regression lines calculated for each age group.

In the case of sample F220, two-three zircons were used instead of one, in order to reach a beam intensity suitable for analysis. In the case of sample F180-2, the step-heating multi-grain technique (Kober 1987; Klötzli 1997) has been applied, to check the eventual presence of an inherited component in the zircons (Fig. 5.7). This technique is similar to the total deposition technique already exposed, but the deposition process is repeated at increasing evaporation temperatures and the IONI filament cleaned between each deposition step.

The evaporation technique allows *a priori* no control on the concordance of the zircons ages. However, it is very unlikely that each grain of the population reached the same apparent age, either by loosing the same amount of radiogenic lead during a metamorphic event, or by incorporating exactly the same proportion of an inherited component. The investigated age-range is young for the strict successful application of the Pb-Pb technique, as shown by Klötzli (1997). The dates obtained by the evaporation technique are therefore interpreted as minimum intrusion ages closely approximating the true intrusion age. The accuracy of the method is sufficient, since our purpose is to distinguish the units by their difference in igneous-activity age, and this difference resulted to be at least 100 Ma (see chapter 5). Furthermore, an important issue with the Pb-Pb evaporation technique is the absence of expensive, time consuming and tedious clean-laboratory procedure prior to analyses. This technique has been preferred to the conventional dissolution technique because it allowed the dating of a higher number of samples, thus achieving a better geographical and structural coverage. The homogeneity of the units is therefore confirmed.

SHRIMP dating

The U-Th-Pb SHRIMP (Sensitive High Resolution Ion Micro Probe) technique allows punctual dating of single domains within the grains. Together with a previous CL study, it permits the dating of complex zircons (e.g. with high proportion of inherited cores, since such inheritance makes Pb-Pb or even U-Pb ID-TIMS dating hazardous). The excellent reviews from Williams (1998) and Stern (1997) have been mainly used to synthetize the short introduction about data acquisition and treatment in SHRIMP analyses given in the frame of pages 22 and 23.

Zircon grains were hand-selected and mounted in epoxy resin together with chips of the reference zircons TEMORA 1 (Black *et al.* 2003) and 91500 (Wiendenbeck *et al.* 1995). The grains were sectioned approximately in half and polished. Reflected and transmitted light micro-photographs and cathodo-luminescence SEM images were acquired for all zircons. We used the CL images to decipher the internal structures of the sectioned grains and to target specific areas within them.

U-Th-Pb analyses were made by T. Reischmann using the SHRIMP-II at the Centre of Isotopic Research, VSEGEI, St. Petersburg, Russia. Each analysis consisted of 5 scans through the mass range, with a spot diameter of about 20 μm, and primary beam intensity of about 4 nA. The data have been reduced in a manner similar to that described by Williams (1998, and references therein), using SQUID (Ludwig 2001). The Pb-U ratios have been normalized relative to 0.0668, the $^{206}Pb/^{238}U$ value of the TEMORA 1 reference zircons, equivalent to an age of 416.75 Ma (Black *et al.* 2003). Isotopic ratios and errors are summarized in appendix 4. The Ahrens-Wetherill (1956) concordia plots, prepared with Isoplot/Ex (Ludwig 2003), for the SHRIMP spot-analyses relative to the last igneous growth are given in Fig. 5.2 and 5.4 The CL patterns, locations of the analytical spots and associated $^{206}Pb/^{238}U$ ages illustrate the textural and geochronological core-rim relationships (Fig. 5.3 and 5.5).

Whenever possible, the Pb_{com} correction was based on the measured ^{204}Pb, assuming no a priori concordance of the analyzed spot-ages. In the case of negative counts on the mass 204, hints for very low amount of Pb_{com}, the ^{208}Pb correction method has been preferred. In the case of “negative” Pb_{com} amounts using both correction methods, we supposed absence of Pb_{com} in the analyzed domain, and therefore applied no Pb_{com} correction. Uncertainties given for individual analyses (ratios and ages) are at the 1 σ level, the uncertainties of the calculated concordia ages are reported at the 95% confidence level.

Whole-rock geochemical analyses

After cleaning of the sample and a first rough crushing, fresh bits have been hand-picked. Then, an agate mill has been used to obtain fine powders at the Max Planck Institute for Chemistry Mainz (Germany). Major and trace elements have been determined on glass and powder pellets, respectively, with an X-ray fluorescence spectrometer Philips Magic X PRO at the University of Mainz. Whole-rock analyses are summarized in appendix 5a and 5b. We handled and plotted the data mostly using GDCkit (Janousek *et al.* 2003).

A word about SHRIMP procedure and data reduction

After mounting of the zircons in epoxy mounts (together with zircon standards), in a similar manner as for CL imaging preparation, the abraded and polished mount is cleaned, dried and carbon coated. CL images at taken and studied. Then the mount, after cleaning and gold re-coating, is introduced inside the Ion-Probe. After high vacuum is reached, the sample is bombarded with a high-energy focused ion beam (O_2^-): the primary ion beam. The result of this is the sputtering of an ion soup from the analysed surface. This ion soup is then accelerated (secondary ion beam), filtered and focused by electrostatic analyser, energy slit, quadrupole lens and magnet. $^{30}Zr_2\,^{16}O^+$, $^{204}Pb^+$, background, $^{206}Pb^+$, $^{207}Pb^+$, $^{208}Pb^+$, $^{238}U^+$, ^{232}Th, $^{232}Th^{16}O^+$, and $^{238}U^{16}O^+$ are then measured on an ion counter. Note that the lead is sputtered as metal whereas U has the tendency to combine with O to produce oxide compounds. At the sputtering area, a lot of hybrids are formed and accelerated into the secondary ion beam, but the design of the SHRIMP II used in this study, with a mass resolution of about 5000, allows separating the different potential interfering masses. Unknown and standards are analysed alternately at a frequency of about 3 unknowns for 1 standard during the same session.

<u>Common lead correction</u>

The measured lead isotopes need first of all to be corrected for common lead. The only non radiogenic lead isotope is ^{204}Pb. Therefore, in theory, it should be on the basis of its amount that the common lead correction should be calculated. But its abundance in routine SHRIMP analyses is very low and counting statistics on this mass sometimes poor. This is why other methods of stripping the common lead from measured data have been implemented. These methods are based on the measured ^{208}Pb and ^{207}Pb. In addition to the ^{204}Pb method, only the ^{208}Pb method will be described here, these two methods being the only one used in this work for data treatment.

f_{206} is the fraction of common ^{206}Pb in the total measured ^{206}Pb.

$$f_{206} = {}^{206}Pb_c / {}^{206}Pb_t$$

with:
c:common
t:total

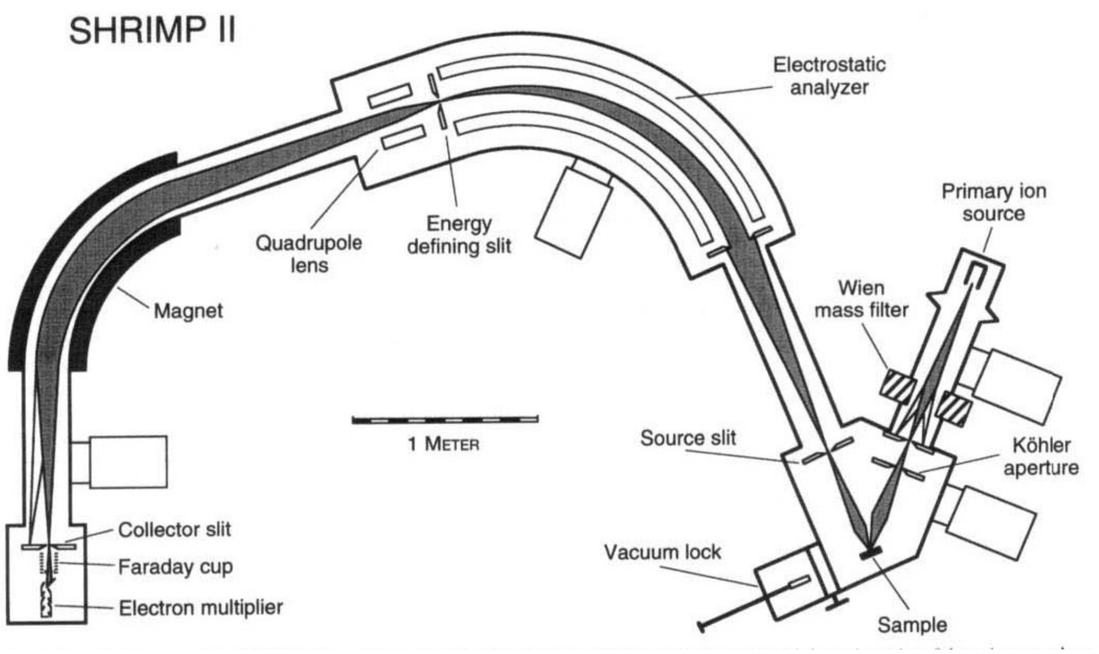

Fig. 3.3.
SHRIMP II design after Williams (1998).

The ^{204}Pb method

In this method f is calculated directly by the measured $^{204}Pb/^{206}Pb$. The only assumption is the composition of the common lead.

$$f_{206} = (^{204}Pb/^{206}Pb)_m \,/\, (^{204}Pb/^{206}Pb)_c$$

with:

m: measured

Radiogenic isotopic ratios can be calculated from such equations. For instance the $^{206}Pb^*/^{238}U$ is extracted from the ($^{206}Pb/^{238}U$) measured by:

$$^{206}Pb^*/^{238}U = (1-f_{206})\,(^{206}Pb/^{238}U)_m$$

The ^{208}Pb method

This method requires the assumption that the Th-U system remained undisturbed. The expected $^{208}Pb/^{206}Pb$ can be calculated by:

$$_8R^* = {}^{208}Pb^*/^{206}Pb^* = (^{232}Th/^{238}U)\,[(e^{\lambda_{232}t}-1) \,/\, (e^{\lambda_{238}t}-1)]$$

Then f is calculated from:

$$f = [(^{208}Pb/^{206}Pb)_m - {}_8R^*] \,/\, [(^{208}Pb/^{206}Pb)_{com} - {}_8R^*]$$

<u>**Calibration for Pb-U isotopic ratios**</u>

Analysis of $^{207}Pb/^{206}Pb$ by ion probe is straightforward under reserve of common lead correction, but measuring Pb/U isotopic ratios is more difficult because Pb and U have different secondary ionization efficiencies. Lead sputtering is enhanced over Uranium. Therefore, SIMS determinations of Pb/U are based on calibrations against reference minerals that are assumed to have uniform radiogenic $^{206}Pb/^{238}U$ (here zircon standard). The measured $^{206}Pb^+/^{238}U^+$ is very different from the real $^{206}Pb^*/^{238}U$ of the analysed domain, due to the already mentioned difference in secondary ionization efficiencies between U and Pb. On the other hand, the $^{238}U^{16}O^+/^{238}U^+$ is directly determined and not affected by difference in sputtering efficiency. Hinthorne *et al.* (1979) showed that measured $^{238}U^{16}O^+/^{238}U^+$ and $^{206}Pb^+/^{238}U^+$ are correlated as shown in Fig 3.4. After several model for its expression, the currently accepted correlation form is as follows (Claoué-Long *et al.* 1995):

$$(^{206}Pb^+/^{238}U^+) = A\,(^{238}U^{16}O^+/^{238}U^+)^2$$

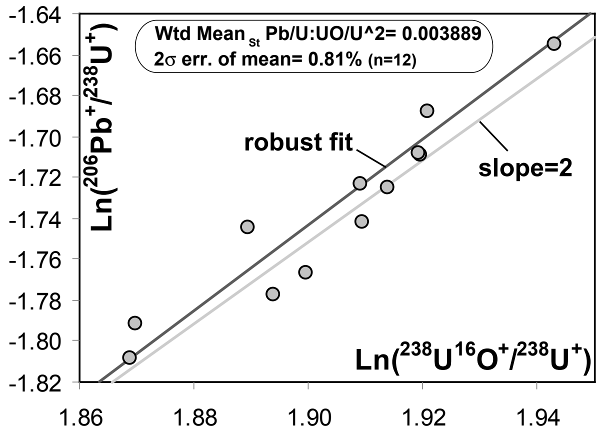

Fig. 3.4.
Graphic representation of the calibration curve used in the SHRIMP session of this study.

A is the constant used for the U/Pb calibration. It is calculated by repeated measurements (during the same session) of the standard. This standard is of known and as uniform as possible $^{206}Pb/^{238}U$ value. $^{206}Pb^*/^{238}U$ of the unknown is then obtained by the relation:

$$(^{206}Pb^{+*}/^{238}U^+)_u = \frac{[(^{206}Pb^{+*}/^{238}U^+)_{st}(^{206}Pb^+/^{238}U^+)_{u,m}]}{[(^{206}Pb^+/^{238}U^+)_{st}]}$$

With:

u: unknown

st: standard

and $(^{206}Pb^*/^{238}U)_{st}$ = constant (known)

The $(^{206}Pb^+/^{238}U^+)_{st}$ is obtained from the calibration curve thus:

$$(^{206}Pb^+/^{238}U^+)_{st} = A\,(^{238}U^{16}O^+/^{238}U^+)^2$$

(at the same value of $^{238}U^{16}O^+/^{238}U^+$ as the unknown zircon)

<u>**Calibration for U-Th isotopic ratios**</u>

The U-Th ratio used in the ^{208}Pb common lead correction is calculated in a similar way as for the Pb-U calibration, from the measured $^{232}Th^+/^{238}UO^+$ by the empirical relation (Williams *et al.* 1996):

$$^{232}Th/^{238}U = {}^{232}ThO^+/^{238}UO^+[0.03446(^{238}U^{16}O^+/^{238}U^+)+0.868]$$

Chapter 4

Field relationships

This chapter gives a more detailed description of the Greek part of the Central Rhodope Massif and of the studied cross-sections. The description of the dated samples is also given at the end of this chapter.

The Central Greek Rhodope can be subdivided in three main units:

-At the lower structural position, the **Pangeon Unit** (Fig. 4.1) consists of a thick horizon of marbles with minor amphibolites, calcsilicates and orthogneisses. For the detailed mapping of this unit, the reader is sent to the work of Kronberg (1969) and Jordan (1969). The depositional age of this impressive marble unit is unknown. These marbles typically overly orthogneisses along tectonic contacts. The orthogneisses belonging to this unit overthrust the marbles in some places, notably north of Drama (see Fig. 4.2.b). The orthogneisses are also found tectonically emplaced within the marbles (e.g. sample RH123). The orthogneisses of this unit display typically an augen texture but are also sometimes non porphyritic. They are either dark Bt-Mu or leucocratic Mu gneisses. The whole unit displays an intense penetrative top-to-the-SW shearing under amphibolite and green-schist facies (Burg *et al.* 1996; Dinter 1998 and references therein). The extremely well defined foliation is sub horizontal with kilometric-scale waving along NE-SW trending opened folds (Kronberg 1969). The foliation bends to a steeper dip towards the NE at the vicinity of the overlying unit, that we will call the melange zone (the lower part of the Mesta unit of Ricou *et al.* 1998).

-The Pangeon Unit is overthrusted by a relatively thin **"melange zone"** (ca. 1-km thick in Xanthi area) bearing most of the amphibolitic material. Grt-Ky metasediments, migmatites, orthogneisses, and minor marbles are also present. This unit displays important signs of partial melting in contrast to the Pangeon unit. This NE dipping unit is intensively sheared top to the SW (Burg *et al.* 1996; Barr *et al.* 1999; Moriceau 2000).

-An orthogneissic complex occupies the higher structural level of the Greek part of the massif. This complex will be named in the discussion the **Rhodope Terrane**. It corresponds to the Mesta unit (Ricou *et al.* 1998) or Sidironero complex (Krohe & Mposkos 2002). The main lithology present in the unit is a non-porphyritic Bt-orthogneiss. Despite a locally strong foliation, the deformational pattern of the unit is obscured by the locally important migmatitization. Furthermore, this orthogneissic unit is strongly intruded by the Skaloti-Oreo granitic complex. This undeformed granite intrudes the foliated country rock along a gradational contact. It is problematic whether the heat induced by the granite is at least partly responsible for the migmatitization. The main granitic body is undeformed and includes a large volume of the foliated country rock as xenoliths (Fig. 4.6.c-f). The dykes from the granite are generally undeformed but locally some pegmatites,

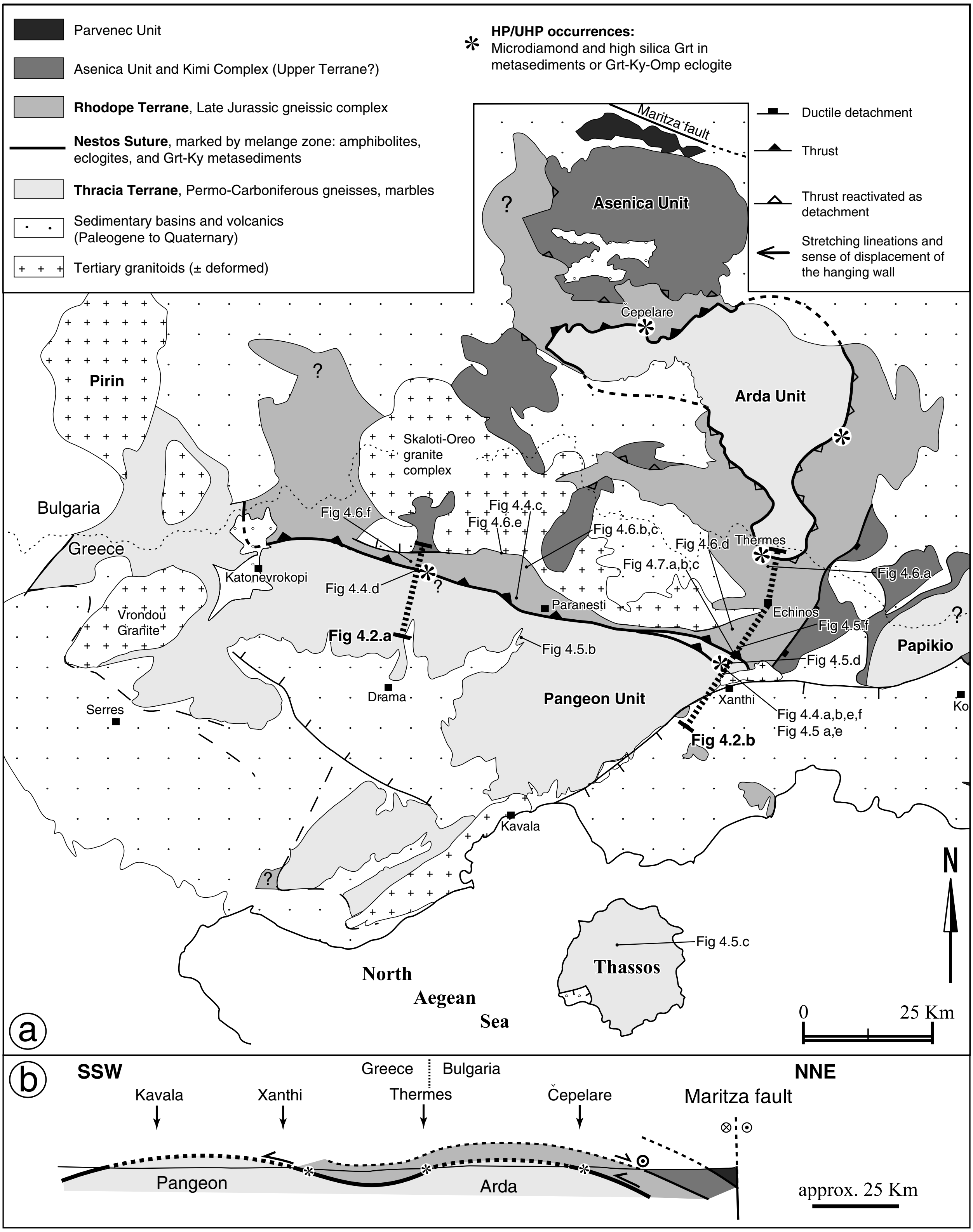

Fig. 4.1

(**a**) Sketch map of the Central Rhodope illustrating the subdivision defined in this study. Compilation after Kronberg (1969), Bornovas & Rondogianni-Tsiambaou (1983), Ivanov (1988), Burg *et al.* (1990 and 1996), Ricou *et al.* (1998), Moriceau (2000) and own observations. Location of figures, and the eclogite or UHP occurrences are shown (Kolcheva *et al.* 1986; Liati & Seidel 1996; Mposkos & Kostopoulos 2001; Kostopoulos *et al.* 2003; Perraki *et al.* 2004). Note the traces of the cross sections of Fig. 4.2.

(**b**) NNE-SSW idealized cross-section of the Central Rhodope. Note the flat-lying nature of the proposed suture separating the two terranes and its probable rooting below the Asenica Unit, at the contact with the Maritza fault. Tertiary intrusives, brittle faulting and sedimentary basins were removed to simplify the scheme.

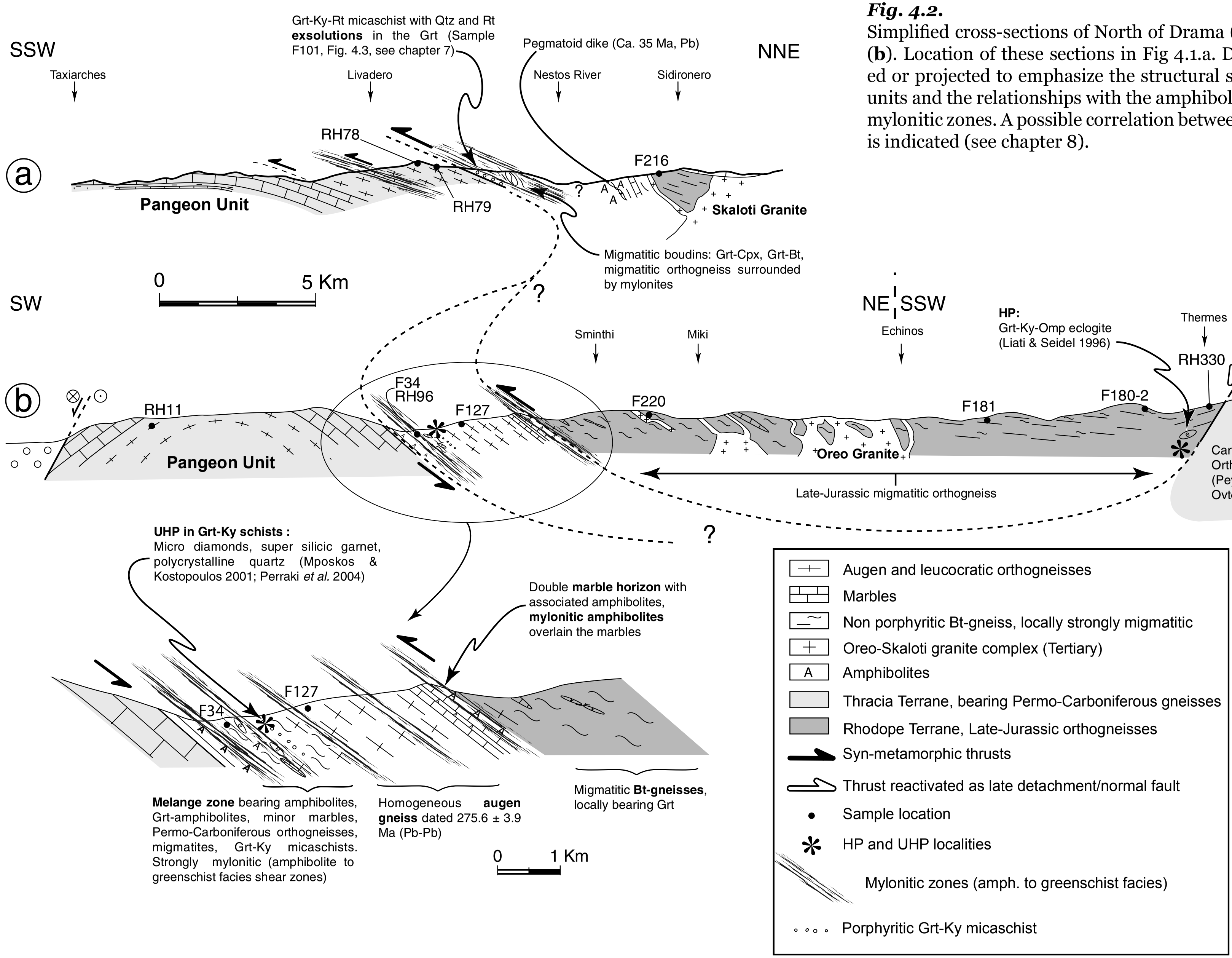

Fig. 4.2.
Simplified cross-sections of North of Drama (**a**) and North of Xanthi (**b**). Location of these sections in Fig 4.1.a. Dated samples are located or projected to emphasize the structural superposition of the two units and the relationships with the amphibolites, UHP-HP relics and mylonitic zones. A possible correlation between the two cross-sections is indicated (see chapter 8).

probably related to the same intrusive suite, are severely deformed, raising the question of the exact timing of deformation and granitic intrusion(s?). This question remains opened.

In order to constrain the structural relationships between the dated samples and the melange zone, we studied in detail two sections perpendicular to the main structures. The locations of both sections are shown in the map of Fig. 4.1.

North of Xanthi section

-North of Xanthi (Fig. 4.2 b): In the Pangeon Unit some minor amphibolites are present at the contact between the marbles and the underlying leucocratic orthogneisses. The melange zone, consisting mostly of migmatites, orthogneisses (samples RH96 and F34), minor marbles, amphibolites, Grt-amphibolites and Grt-Ky schists, overlies the Pangeon marbles (for a detailed description of this sector see Barr *et al.* 1999). This melange zone shows an intense amphibolite to green-schist facies shearing. The transport direction is consistently top-to-the-SW (Fig. 4.5.a,d-f). Some Grt-Ky schists preserved metamorphic microdiamonds and garnets with exsolutions of quartz and rutile. These features are interpreted as records of an UHP metamorphism (Mposkos & Kostopoulos 2001; Perraki *et al.* 2004; see for further discussion Beyssac & Chopin 2003 and Mposkos & Kostopoulos 2003). A ca. 1-km thick sliver of augen-gneiss (sample F127) overlies the melange zone. Further upward, mylonitic amphibolites overthrusted the double horizon of marbles associated with amphibolites (Fig. 4.7.a-c). Overlaying these amphibolites, an orthogneissic complex is pervasively intruded either by syn- to post-deformational pegmatitic dykes from the adjacent Skaloti-Oreo granite, or by the granite itself (Kronberg & Raith 1977; Lips *et al.* 2000 and personal observations; Fig. 4.6.a-e). This orthogneissic complex is dominated by Bt-gneisses, with occurrence of hornblende, and is strongly migmatitic at the base (e.g. sample F220). In this unit, stretching lineations are scarce, thus its detailed internal kinematics remains problematic. This is most probably due to the strong HT overprint resulting in the widespread partial melting and recrystallization of most of the kinematic indicators (Kronberg & Raith 1977). Close to the Greek-Bulgarian border (Thermes, Fig. 4.1.a and 4.2.b), an eclogite experienced minimum peak-pressure of about 19 Kbar (Liati & Seidel 1996). This eclogite is exposed close to the contact between the Bt-gneiss unit and the Arda Unit. This contact, reactivated by intense cataclastic deformation, is a site of hydrothermal activity (justifies the name of the locality).

North of Drama section

-North of Drama (Fig. 4.2 a): the frame is slightly different. Above the Pangeon Marbles, instead of the melange zone, a ca. 2-km thick unit of non-migmatitic orthogneisses crops out. These two lithologies are separated by a non impressive contact, bearing minor, strongly retrogressed amphibolite boudins. Within this unit, a highly sheared marble horizon is exposed near Livadero village. The

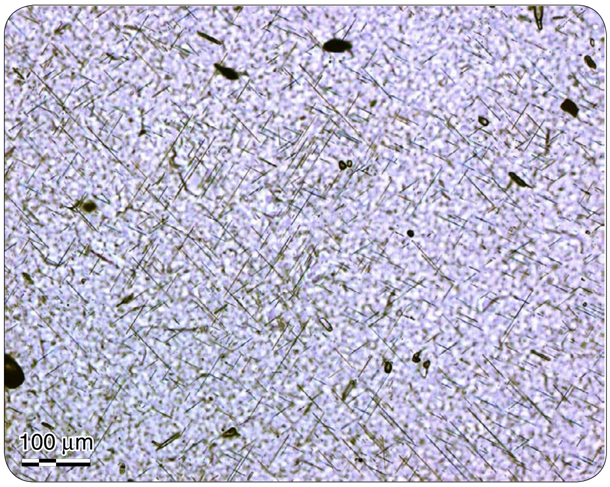

Fig. 4.3.
Microphotograph of garnet from the Grt-Ky-Rt micaschist F101 (location in Fig. 4.2.a and 4.8). Note the systematic orientation of needles, following crystallographic orientations. These needles, interpreted as exsolutions, consist of quartz and rutile (analysed by microprobe, see chapter 7). They point to a former high Si and Ti garnet precursor (supersilisic garnet?), and therefore to an eventual UHP metamorphic event predating re-equilibration at lower pressure.

The "Melange" zone

Fig. 4.4.a.
Boudins of amphibolites and quartzo-feldspatic melt (view toward the NE, perpendicular to the stretching lineation). Melange zone, north of Xanthi.

Fig. 4.4.b.
Rootless folds in amphibolitic material, note the complexity of the partial melting/deformation history (view toward the NE, perpendicular to the stretching lineation). Melange zone, north of Xanthi.

Fig. 4.4.c.
Boudin of Grt-bearing amphibolite surrounded by Pl-Grt melt. NW of Paranesti.

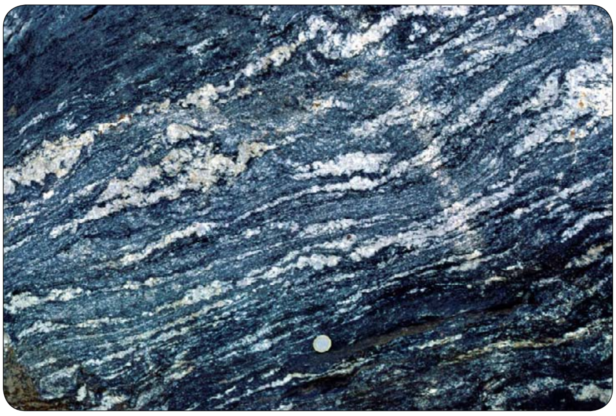

Fig. 4.4.d.
Example of Grt-Bt migmatite, occurring in a strain pocket within the melange zone north of Drama.

Fig. 4.4.e.
The strain can be extreme in the melange zone as exampled by this "a" type isoclinal fold (view toward the NE, perpendicular to the stretching lineation, hammer indicates the stretching lineation), north of Xanthi.

Fig. 4.4.f.
Another example of extreme strain but in green-schist facies (hammer indicates the stretching lineation). Melange zone, north of Xanthi.

Shear sense indicators

Fig. 4.5.a.
Micro-folds with apparent overturning towards the SW interpreted as drag fold resulting from a top-to-the-SW shearing. Melange zone, north of Xanthi.

Fig. 4.5.b.
σ clast in a Bt-Mu augen-gneiss (sample RH60). Pangeon Unit, SW of Paranesti.

Fig. 4.5.c.
C/S shear bands in a Bt-Mu augen gneiss from Thassos Island (sample RH89).

Fig. 4.5.d.
Post-migmatitic C' shear band in a Bt-gneiss within the melange zone north of Xanthi.

Fig. 4.5.e.
σ clasts within the melange zone north of Xanthi.

Fig. 4.5.f.
Big σ clast of pegmatitic material (interpreted as co-genetic with the Skaloti-Oreo granite) within fine grained Bt-gneiss (melange zone, north of Xanthi).

The Bt-gneiss unit

Fig. 4.6.a.
Typical aspect of the upper unit (Rhodope Terrane) when the Bt-gneiss is not strongly migmatitic. The leucocratic intrusives are dykes of the Skaloti-Oreo granite (south of Thermes, sample F180-2).

Fig. 4.6.b.
Another example of the Bt-gneiss from the upper unit (north-west of Paranesti).

Fig. 4.6.c.
More foliated facies of the Bt-gneiss. Note the importance of leucocratic intrusives (north-west of Paranesti).

Fig. 4.6.d.
The lower part of the upper unit, north of Xanthi, is migmatitic and strongly intruded by dykes of the Skaloti-Oreo granite (sample F220).

Fig. 4.6.e.
The contact between the Bt-gneiss and the Skaloti granite is never sharp. Indeed, the contact is gradational; an important volume of dykes is found within the country rock and many xenoliths of the country rocks are within the granite itself. Between Sidironero and Paranesti.

Fig. 4.6.f.
The pegmatoids of the Skaloti-Oreo granite intruded also the foliated amphibolites north of Nesos River (South of Sidironero).

Fig. 4.7.a.
The double horizon of marbles marks a clear topographic high.

Fig. 4.7.b.
Mylonitic amphibolite above the double horizon of marbles in the Northern Xanthi cross-section. Note the short spacing of the foliation in this rock, as proof for high strain. Scale: camera lid, diameter: ca. 4 cm.

Fig. 4.7.c.
Close-up on the foliation of the amphibolites above the double horizon of marble. Note that the granitic leucocratic material is intrusive in the foliated amphibolites but is also weakly foliated itself.

base of the orthogneiss unit is leucocratic, whilst its upper part consists of augen- and Bt-gneisses (samples RH79 and RH78). Above the gneissic unit, a thin layer of Grt-Ky-Rt micaschist was sampled. Its garnets show abundant needles of quartz and rutile (sample F101, Fig. 4.3; see also chapter 7). These metasediments are associated with Grt-Pl-Cpx and Grt-Pl-Bt migmatites, as well as amphibolites and ortho-migmatites. This association of lithologies, in our view, represents the lateral equivalent of the already described melange zone North of Xanthi. Besides signs of partial melting can be found only above the Grt-Ky micaschists. Further upward, on the northern side of the Nestos River, amphibolites associated with marbles are overlain by a Bt-gneiss (F216), which in turn is strongly intruded by the adjacent Skaloti granite.

Samples description

RH11:

Sample RH11 is a leucocratic orthogneiss collected below the marbles of the Pangeon unit, ca. 2 Km North of Xhrissa (SW of Xanthi). In thin section, it shows K-feldspar porphyroclasts within a locally intensively deformed matrix consisting of quartz and muscovite.

RH60:

RH 60, collected ca. 6 Km southwest of Paranesti, is a typical dark coloured augen-gneiss (Fig. 4.5.b). It displays a clear top-to-the-SW shear sense, evidenced by σ tails around the K-feldspar porphyroclasts. These porphyroclasts are often mantled by myrmekites and are within a strongly foliated greenish-brown Bt, Mu, Qz and epidote matrix. Some late stage chlorites are also present. As the epidotes are concentrated in foliation-parallel bands, they are interpreted as metamorphic (Ca-rich fluid circulation?). On the other hand, numerous brittely deformed titanite belong to the pristine paragenesis.

RH78:

This sample was collected ca.15 km south of Sidironero, at the pass on the road from Drama. It is a

Table 4.1. Short description, mineralogy and location of the orthogneiss or granitoid samples. Mineral abreviations after Kretz (1983).

age group	Sample	Rock type	Mineralogy	Comments	Latitude; Longitude	Area
Permo-Carboniferous	RH11	Leucocratic gneiss	Qtz, Kfs, Mu, op, Zrn	foliated, altered	41°08.883'N; 24°50.883'	North-Xanthi
	RH60	Augen gneiss	Qtz, Kfs, Bt, Mu, Ep(II), Chl (II), Ttn, Pl, Zrn	foliated, top SW shearing	41°14.566'N; 24°26.900'	West-Paranesti
	RH78	Bt-gneiss	Qtz, Kfs, Ep, Bt, Ttn, Zrn	foliated, top SW shearing	41°18.433'N; 24°12.866'	North-Drama
	RH79	Augen gneiss	Qtz, Kfs, Mu, Bt, Zrn	foliated, top SW shearing	41°19.683'N; 24°12.466'	North-Drama
	RH87	Bt-gneiss	Qtz, Pl, Bt, Kfs, Ep, Ttn, Zrn	foliated	41°20.133'N; 23°49.433'	Katonevrokopi
	RH89	Augen gneiss	Qtz, Kfs, Mu, Bt, Zrn	foliated, top SW shearing	40°43.133'N; 24°37.883'	Thassos
	RH96	Augen gneiss	Qtz, Kfs, Mu, Bt, Zrn	foliated, top SW shearing	41°10.916'N; 24°51.013'	North-Xanthi
	RH123	Leucocratic gneiss	Qtz, Kfs, Mu, Zrn	foliated, top SW shearing	41°07.038'N; 24°22.348'	Kavala
	RH336	Leucocratic gneiss	Qz, Fl, Mu, Bt	foliated, top SW shearing	40°55.400'N; 24°17.177'	Kavala
	F34	Augen gneiss	Qtz, Kfs, Chl (II), Bt, Mu, Pl	foliated, top SW shearing	41°11.192'N; 24°51.801'	North-Xanthi
	F127	Augen gneiss	Qtz, Kfs, Pl, Bt	foliated, top SW shearing	41°11.912'N; 24°51.646'	North-Xanthi
	RH132	Augen gneiss	Kfs, Qtz, Pl, Bt, Chl (II), Mu, Zrn		41°11.850'N; 24°50.554'	North-Xanthi
	RH31	Augen gneiss	Qtz, Kfs, Pl, Bt, Chl (II), Op, Ttn	foliated	41°12.400N; 24°51.782'	North-Xanthi
	RH311	Leucocratic gneiss	Qz, Kfs, Mu	foliated, top S shearing	41°06.503N; 25°51.404'	Byala-Reka
	RH323	Augen gneiss	Qz, Fs, Bt, Mu		41°14.068N; 26°02.299'	Byala-Reka
Late Jurassic/Early Cretaceous	RH126	Bt-granite	Qz, Pl, Bt, Ttn, Zrn	weakly deformed	41°17.309'N; 24°28.856'	West-Paranesti
	RH330	Bt-Amp gneiss	Qtz, Pl, Amp, Bt, Ttn, Op (Py...)		41°20.391'N; 25°02.130'	Thermes
	F180-2	Bt-Amp gneiss	Qtz, Pl, Amp, Bt, Op (Py...)		41°20.994'N; 24°58.037'	North-Xanthi
	F181	Bt-granite	Qtz, Pl, Bt, Chl(II), Op, Mu, Zrn	weakly deformed	41°17.871'N; 24°57.612'	Thermes
	F190	Bt-gneiss	Pl, Qtz, Bt, Amp, Ep, Ttn	weakly deformed	41°19.601'N; 24°27.493'	West-Paranesti
	F216	Bt-gneiss	Pl, Qtz, Bt, Zrn	foliated	41°21.634'N; 24°13.286'	North-Drama
	F220	Bt-migmatitic gneiss	Qtz, Bt, Pl, Kfs, Grt(II)	foliated, migmatitic	41°14.254'N; 24°53.169'	North-Xanthi
	F180-1	Bt-Amp gneiss	Pl, Qtz, Amp, Bt, Chl (II), Op, Grt (incl. in Pl), Zrn		41°20.994'N; 24°58.037'	North-Xanthi
	F203	Bt-gneiss	Qz, Pl, Bt		41°19.722'N; 25°03.394'	Thermes
	F206	Bt-gneiss	Qtz, Pl, Bt, Chl (II), Op, Zrn	foliated	41°20.801'N; 25°01.079'	Thermes
	F207	Bt-gneiss	Qtz, Pl, Bt, Op, Chl (II), Ap, Grt, Zrn		41°16.424'N; 24°58.612'	Echinos
	F224	Bt-gneiss	Qtz, Pl, Bt, Chl (II), Op, Ttn, Grt (incl. in Pl), Zrn	foliated	41°21.165'N; 24°25.396'	West-Paranesti
	F225	Bt-gneiss	Qtz, Pl, Bt, Mu, Grt (incl. in Pl), Zrn		41°21.699'N; 24°22.657'	West-Paranesti
	F226	Bt-gneiss	Qtz, Pl, Bt,Chl (II), Grt (incl. in Pl), Op, Zrn	foliated	41°21.474'N; 24°24.648'	West-Paranesti

II: secondary
Op: opaque

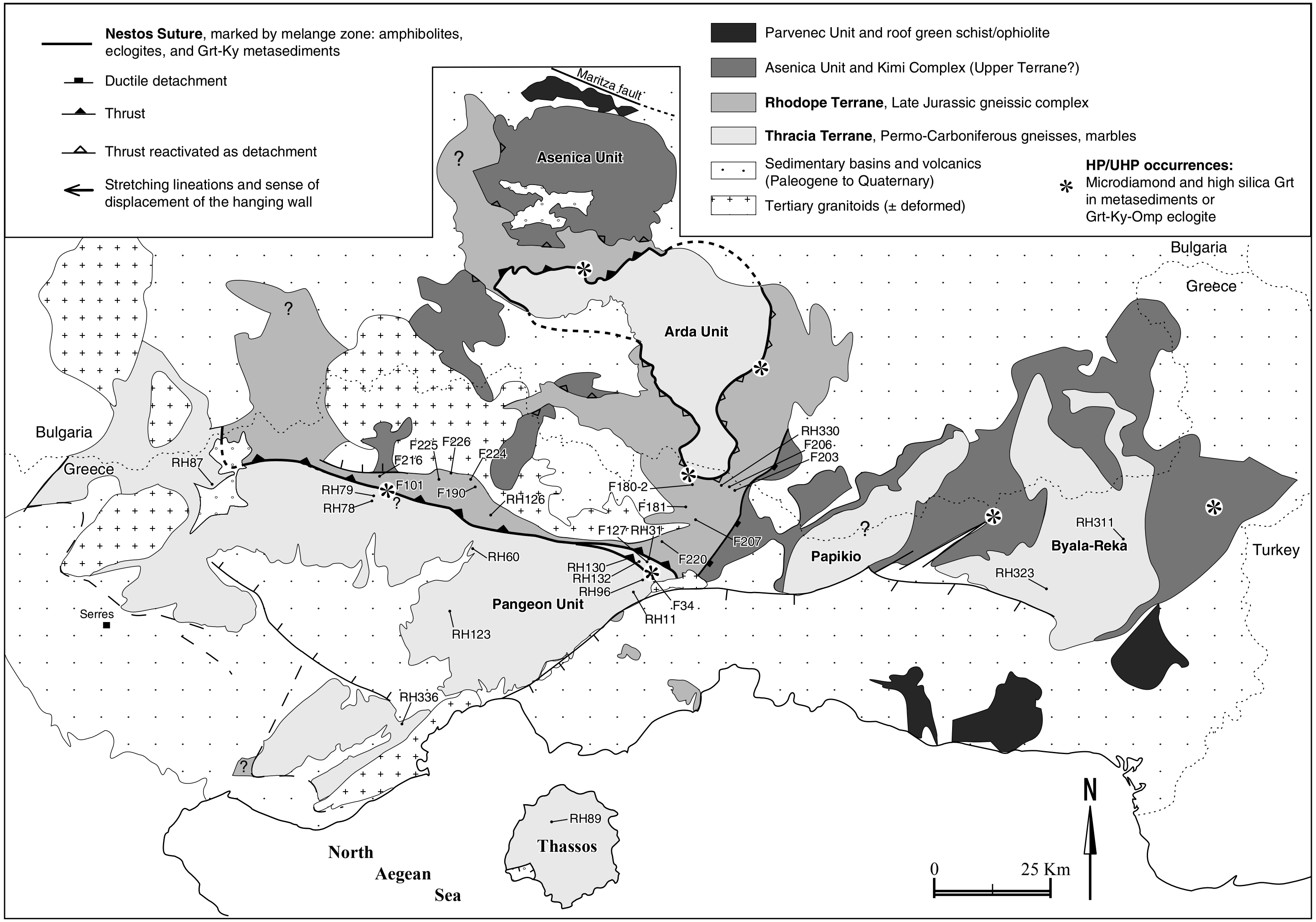

Fig. 4.8. Sketch map of the Central Rhodope locating the samples used for geochemical analyses and dating. Compilation after Kronberg (1969), Bornovas & Rondogianni-Tsiambaou (1983), Ivanov (1988), Burg *et al.* (1990 and 1996), Ricou *et al.* (1998), Moriceau (2000) and own observations.

dark coloured, non-porphyritic, foliated Bt-gneiss. It shows systematic microscale folds with apparent overturning to the SW. This sample bears rare K-felspars. It shows greenish-brown biotites and no Muscovite. Impressive primary titanite clasts are visible in hand specimen. The foliation is also marked by an important amount of epidotes (secondary).

RH79:
This light grey augen gneiss has been collected ca. 10 km south of Sidironero, after the pass on the road that descends to the Nestos River. It is a typical light grey augen-gneiss displaying clear top-to-the-SW ductile shear sense indicators (σ porphyroclasts).

RH87:
This fined grained foliated greenish gneiss outcrops ca. 5 Km west of Katonevrokopi. The primary paragenesis consist of K-feldspar, plagioclase, brown biotite and titanite. Epidotes are secondary minerals.

RH89:
This sample is an intensively deformed augen gneiss collected below the marbles of Thassos Island. Myrmekites mantle the porphyritic K-feldspars. The K-feldspars themselves often ductily deformed (proof for high-temperature deformation). Numerous C' shear bands truncate the foliation, indicating a top to the SW shear sense consistent with σ clast criteria. The porphyritic K-feldspar are within a matrix composed of recrystallized K-feldspar, quartz, muscovite and brown reddish biotite.

RH96:
RH 96 is an intensively weathered, mylonitic, but still porphyritic orthogneiss collected on the road between Pilima and the Xanthi River.

RH123:
This leucocratic orthogneiss has been collected on the road between Egiros and Peristeria. It is located at the base of an orthogneiss slice, tectonically emplaced within the marbles of the Pangeon unit.

F34:
This orthogneiss has been collected on the road along the Xanthi River, ca. 200 m north of the bridge to Pilima over the Xanthi River. The K-feldspars are often altered; biotite often altered in chlorite (titanite needles). Biotite, when fresh, is pale reddish. Numerous C' shear bands, indicating a top to the SW shear sense, truncate the foliation.

F127:
Is a light grey coloured augen-gneiss, collected on the road along the Xanthi River 900 m north of the road junction between Xanthi, Stavroupoli and Sminthi. It belongs to the homogeneous augen gneiss body, visible north of Xanthi, which overthrusts the melange zone and below the double horizon of marble. K-feldspar porphyroclasts and plagioclases occur within a foliated matrix of quartz, dark brown biotite and plagioclase.

RH126:
This weakly deformed granite with homogeneous grain size (ca. 1 mm) has been collected 2 Km North West of Paranesti along the Nestos River. The weakly expressed foliation is marked by a slight preferred orientation of the dark brown-greenish biotite grains. The mineralogy consists of quartz, plagioclase, biotite and titanite. Formally speaking, this rock is a slightly deformed granite rather than a gneiss (weak foliation and no foliation-parallel mineral-segregation).

RH330:
This dark coloured sample outcrop 1.3 Km West of Medusa on the road from Thermes. The mineralogy consists of quartz, plagioclase, amphibole, dark brown biotite, few titanite and pyrite (secondary). Amphiboles display a strong pleochroism from light brown to intense bluish-green. The sample shows a homogeneous grain size and a weak foliation

marked by the orientation of biotite and a beginning of mineral segregation evidenced by elongated quartz aggregates.

F180-2:
This sample, very similar to RH330, outcrops 2 Km south of Thermes. Its mineralogy and texture are the same as RH330, except for the lack of titanite and the slightly higher abundance of quartz and plagioclase.

F181:
This sample, collected 2.4 Km Northwest of Echinos, is a weakly deformed granitoid. The only signs of deformation are undulatory quartz and aggregates of recrystallized quartz. The mineralogy consists of quartz, plagioclase, brown biotite, pyrite (secondary), minor muscovite. The biotites are often partly altered in chlorite.

F190:
This sample was collected on the road along the Nestos River 8.4 Km after the junction between Drama-Paranesti main road and the one heading to the electrical dam along the Nestos River. The mineralogy of this undeformed granite (except for some undulatory quartz) consists of plagioclase, quartz, brown biotite, minor light-brown to bluish-green amphibole, some titanite (primary, pale-brown), and epidote (secondary?). The colour of the amphiboles is as intense as to obliterate interference colours. Zircon is also visible in thin section, both interstitial, and included in plagioclase and biotite.

F216:
Is a fine-grained foliated gneiss collected ca. 1.5 Km south of Sidironero, between Sidironero and the Nestos River. The mineralogy consists of quartz, plagioclase and brown biotite. The foliation is well expressed by the preferred orientation of biotite and quartz.

F220:
This sample, collected 900 m north of Sminthi, shows in hand specimen numerous Qz-Pl aggregates suggesting an intense migmatization. The foliation is intense and marked by the orientation of the brown biotites. The mineralogy is quartz, plagioclase brown biotites. Furthermore, some secondary garnets are present (due to the migmatitization event?). At the contact with the garnets, the biotites are green in polarized light.

Chapter 5

Zircon dating

This chapter exposes the orthogneiss protolith dating via both Pb-Pb and SHRIMP techniques. A striking bimodal distribution of the ages emerged; this is essential for the geological interpretation. Therefore, the data are presented separately for each of the two age groups.

All the dated samples are granitic orthogneisses. Sample description and mineralogy are given in chapter 4 and table 4.1; location of the samples is in Fig. 4.8. The sampling strategy was to avoid whenever possible the migmatitic domains, in order to obtain zircon fractions which U-Pb system was least disturbed by metamorphic overprint.

The main dating technique used in this work is the Pb-Pb single grain evaporation. This technique allows *a priori* no control on the concordance of the ages. However, it is very unlikely that each grain of the population reached the same apparent age, either by loosing the same amount of radiogenic lead during a metamorphic event, or by incorporating exactly the same proportion of an inherited component. The investigated age-range is young for the strict successful application of the Pb-Pb technique (Klötzli 1997); in addition, we cannot exclude some non-contemporaneous Pb-loss. Nevertheless, the CL images generally show well-preserved igneous patterns, hence the metamorphic Pb-loss is considered low (Fig. 5.1, 5.7 and appendix 2). Another argument in favour of a low metamorphic overprint is the overall normal distribution of the apparent $^{207}Pb/^{206}Pb$ ages (Fig. 5.1 and Fig. 5.7). CL images of the zircon grains show high-frequency oscillatory zoning typical of magmatic growth. The dates obtained by the evaporation technique are therefore interpreted as minimum intrusion ages closely approximating the true intrusion age. The accuracy of the method is sufficient, since our purpose is to distinguish the units by their difference in igneous-activity age, and this difference resulted to be at least 100 Ma. The evaporation technique has been preferred to the conventional dissolution technique because it allowed the dating of a higher number of samples, thus achieving a better geographical and structural coverage. The relative homogeneity of the units is therefore confirmed.

Permo-Carboniferous orthogneisses

This group of samples is represented mostly by either Bt-Mu augen gneisses (e. g. RH60, Fig. 4.5.b) or leucocratic gneisses (RH11, RH123; appendix 1a). Despite the strong lithological difference, calculated ages are similar. Samples RH60, RH78, RH79, RH87, RH89, F34 and F127 yielded $(^{207}Pb/^{206}Pb)_{rad}$ single-grain protolith ages between ca. 275 and 290 Ma (Fig. 5.1). Without major rejection, the probability density curves for the apparent ages of these samples are similar to a normal distribution. Moreover, the CL patterns of the zircons from samples RH60, RH78, RH87, and F34 exhibit systematically igneous zoning. Thus, the interpretation of the obtained ages is straightforward and does not require detailed filtering of the data: these Pb-Pb ages represent protolith intrusion-ages.

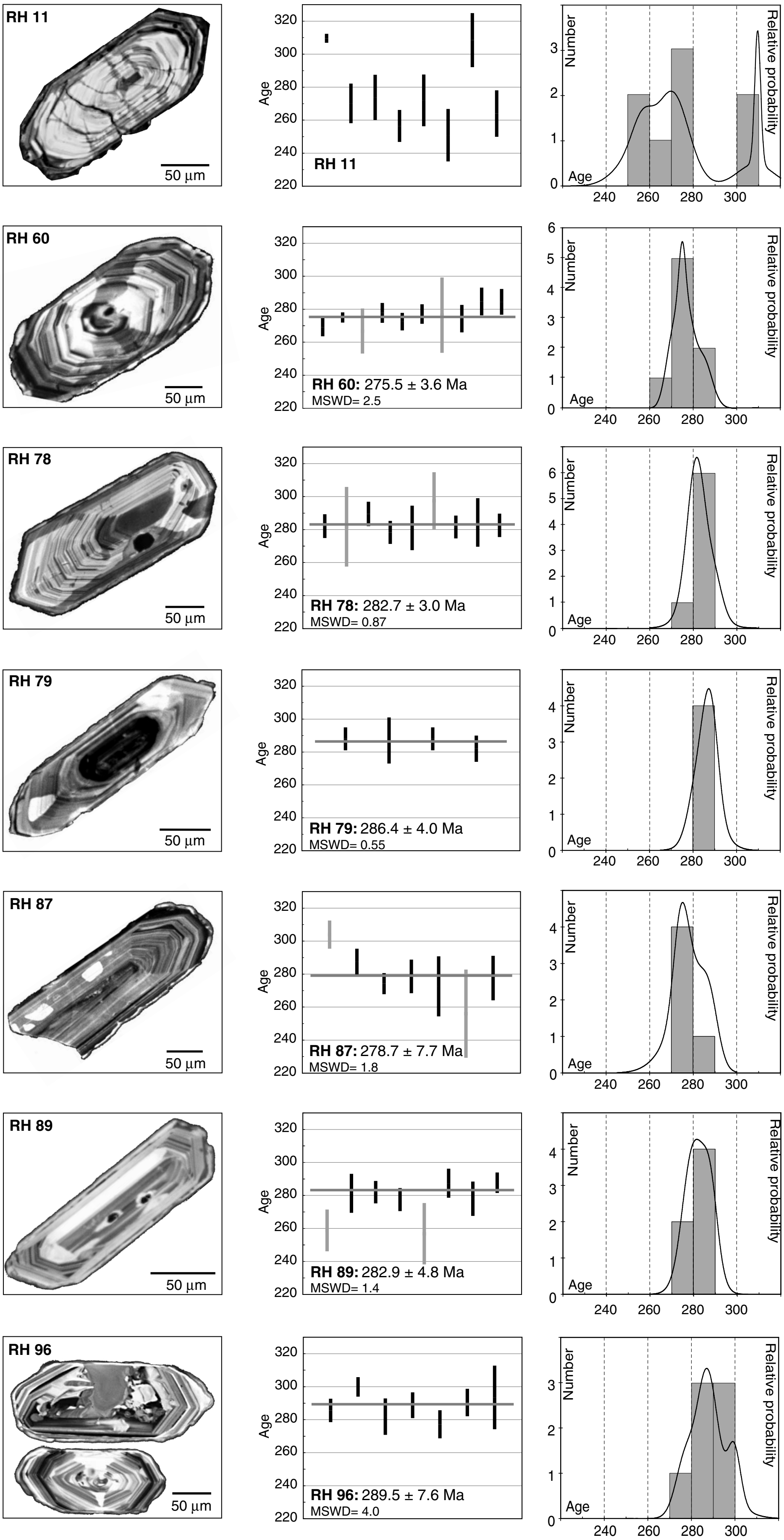
RH 11
50 µm
Age
320
300
280
260
240
220
RH 11
Number
Relative probability
240
260
280
300
RH 60
50 µm
RH 60: 275.5 ± 3.6 Ma
MSWD= 2.5
RH 78
50 µm
RH 78: 282.7 ± 3.0 Ma
MSWD= 0.87
RH 79
50 µm
RH 79: 286.4 ± 4.0 Ma
MSWD= 0.55
RH 87
50 µm
RH 87: 278.7 ± 7.7 Ma
MSWD= 1.8
RH 89
50 µm
RH 89: 282.9 ± 4.8 Ma
MSWD= 1.4
RH 96
50 µm
RH 96: 289.5 ± 7.6 Ma
MSWD= 4.0

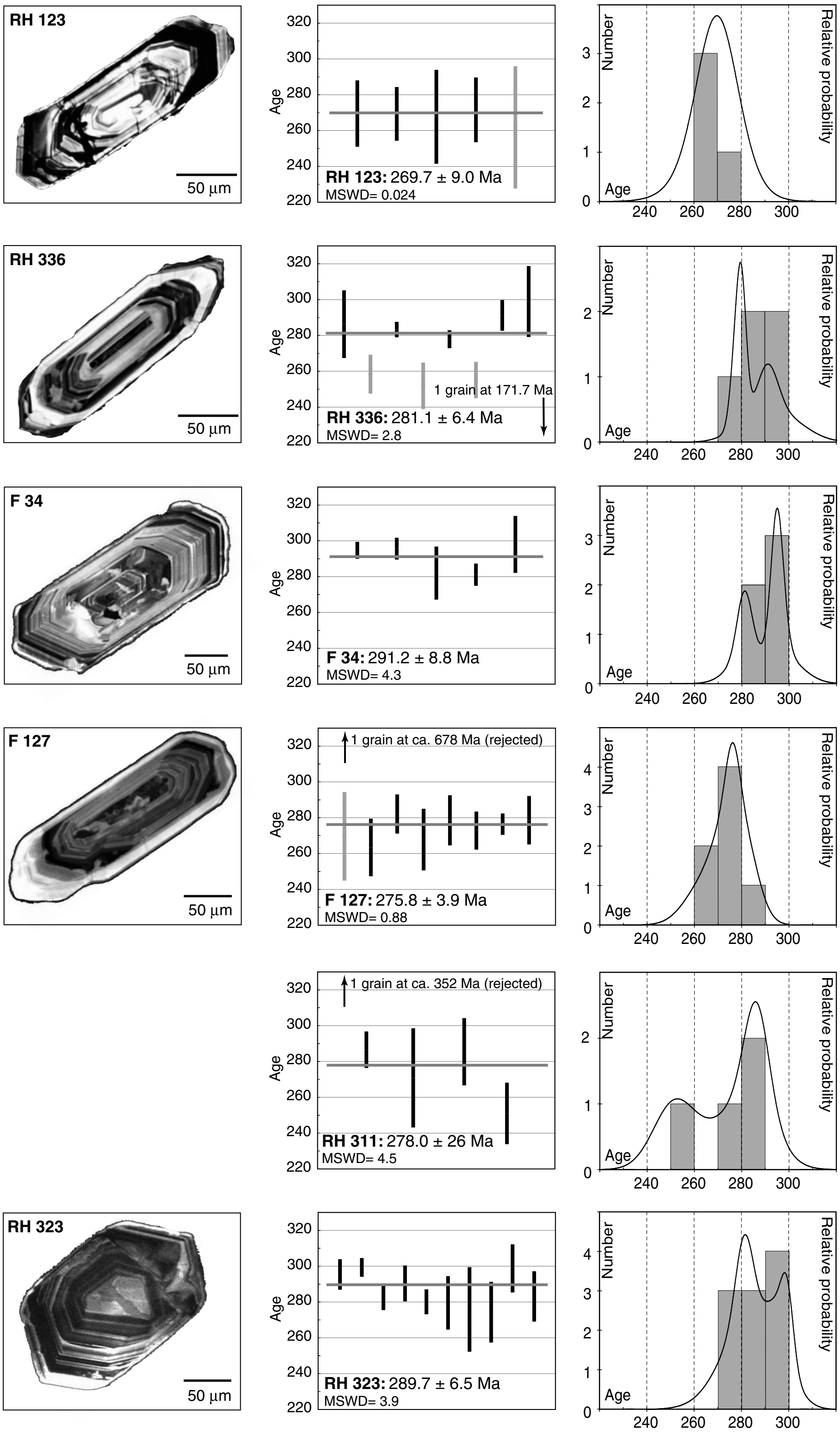

Fig. 5.1. (This page and previous one)
95% confidence level weighted averages of the zircon Pb-Pb apparent ages, cumulative probability diagrams (after data rejection) and representative cathodo-luminescence images of the dated populations of the Permo-Carboniferous group. Apparent ages are single-grain measurements. All error bars are at the 2 σ level of uncertainty. Data rejected from age calculations are plotted in grey. The bin-size of the cumulative histograms is proportional to the mean 2 σ error on the ages. Measured ratios and errors are given in appendix 3.

F127 has nice igneous zoning but the rims are systematically overprinted, brigth, but not completely recrystallised, since the original zoning is still preserved. However, repeted measurements gave a mean weighted average of 275 ± 3.9 Ma (n=7).

Although the zircons from RH 79 showed some inherited cores, no sign of this inheritance is visible in the age data and the CL are typical of igneous zircons. The mean age is 286.4 ± 4.0 Ma (n=4).

Sample RH96 showed some partly recrystallized zircons, sometimes even with very limited metamorphic overgrowths (Fig. 5.1). Despite the metamorphic overprint, the original igneous CL pattern and the intrusion age of 289.5 ± 7.6 Ma do not seem perturbed by lead loss.

Samples RH11, RH 123 and RH87 yielded ages still in the 260-300 Ma range, but with less precise or more scattered results.

Zircons from the leucocratic gneiss RH11 (Fig. 5.1) gave two age populations, one around 310 Ma, and the other at about 260-270 Ma. This scatter of ages can be related to the numerous cracks in zircons from this sample (Fig. 5.1 and appendix 2). Since the Pb-Pb method permits no control on the concordance of the measurements, the discrimination between Pb-loss and inherited cores is difficult; this limitation does not allow to say which is the true intrusion age, either ca. 260-270 Ma or 310 Ma. However, as all the CL images of the zircons from this sample display typical igneous zoning and since all the apparent ages range between 260 and 310 Ma, the Permo-Carboniferous intrusion-age is confirmed.

Samples RH123 and RH87 yielded zircons with a high amount of non-radiogenic lead (often with $^{206}Pb/^{204}Pb \approx 1000$). For RH123, this low $^{206}Pb/^{204}Pb$ is attributed to numerous cracks and probably metamict domains (black domains in the CL image of Fig. 5.1). Rigorously, such low $^{206}Pb/^{204}Pb$ would preclude any dating, the Pb_{com} correction leading to significant error in the calculated age. However, as the ages fall in the 260-300 Ma age range, we consider the intrusion of these samples to be Permo-Carboniferous.

Sample RH336 yielded a significant proportion of zircons with apparent ages below 260 Ma. Although no CL feature diagnostic of lead loss is recognizable, we rejected four out of nine analyses. The five remaining grains gave a weighted average of 281.1 ± 6.4 Ma, interpreted as the intrusion age.

As a result, all dated samples from the Pangeon Unit are Permo-Carboniferous (Fig. 5.9). The two samples from the footwall unit in the Eastern Rhodope belong also to this Permo-Carboniferous group (samples RH311 and RH323 dated respectively 278 ± 26 and 289.7 ± 6.5 Ma, located in Fig. 4.8).

Late Jurassic-Early Cretaceous orthogneisses

This group consists exclusively of non-porphyritic Bt-orthogneisses and granites, locally with amphibole (e.g. RH330, F180-2). They are lithologicaly more homogeneous than the Permo-Carboniferous gneisse that to the contrary show a variability from leucocratic to melanocratic.

The gneisses are locally migmatitic, especially North of Xanthi (Fig. 4.2.b and Fig. 4.6.d), but, despite the intense Tertiary HT overprint, the CL patterns and U-Pb system are not affected (except for sample F220, Fig. 5.7).

Samples RH330 and F216, which showed a high proportion of inherited cores, have been dated using the SHRIMP technique. The analytical spots corresponding to the last growth phase are concordant, and allow the calculation of concordia ages (Ludwig 1998). The corresponding Th/U values are generally between 0.1 and 0.4, typical of igneous zircons (Appendix 4), and the CL patterns of the analyzed zircon-domains show high-frequency oscillatory zoning (Fig. 5.3 and 5.5). The calculated ages are therefore protolith ages.

RH330:

Spots 6.1 and 10.1 (407.5 ± 4.1 and 291.4 ± 3.4 Ma,

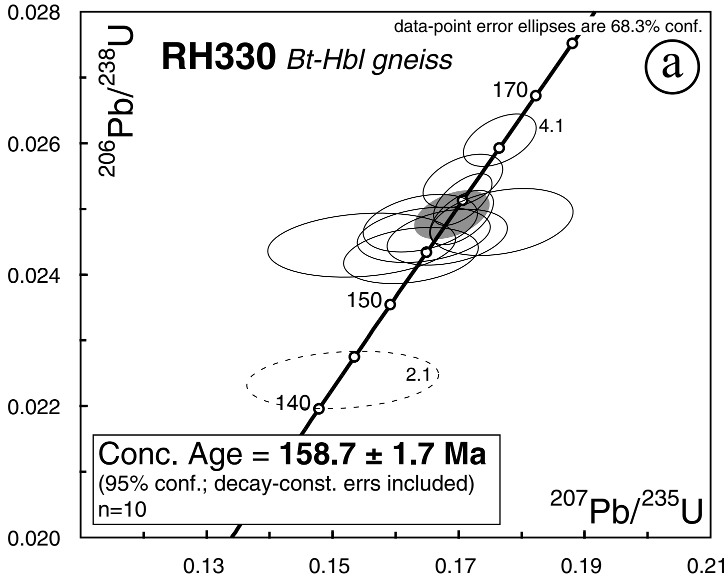

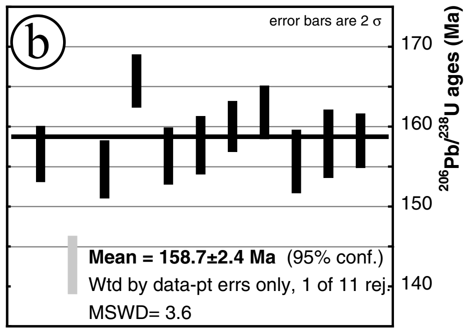

Fig. 5.2.

a) Concordia diagrams of the U-Pb SHRIMP analyses of sample RH330 and calculated concordia ages (grey ellipses). Only the ages younger than 200 Ma are reported since they represent the last igneous growth. In dashed line, analytical spots rejected from concordant age calculation (details of data rejection in the text).

b) Mean weigthed average of $^{206}Pb/^{238}U$ ages of the same data set.

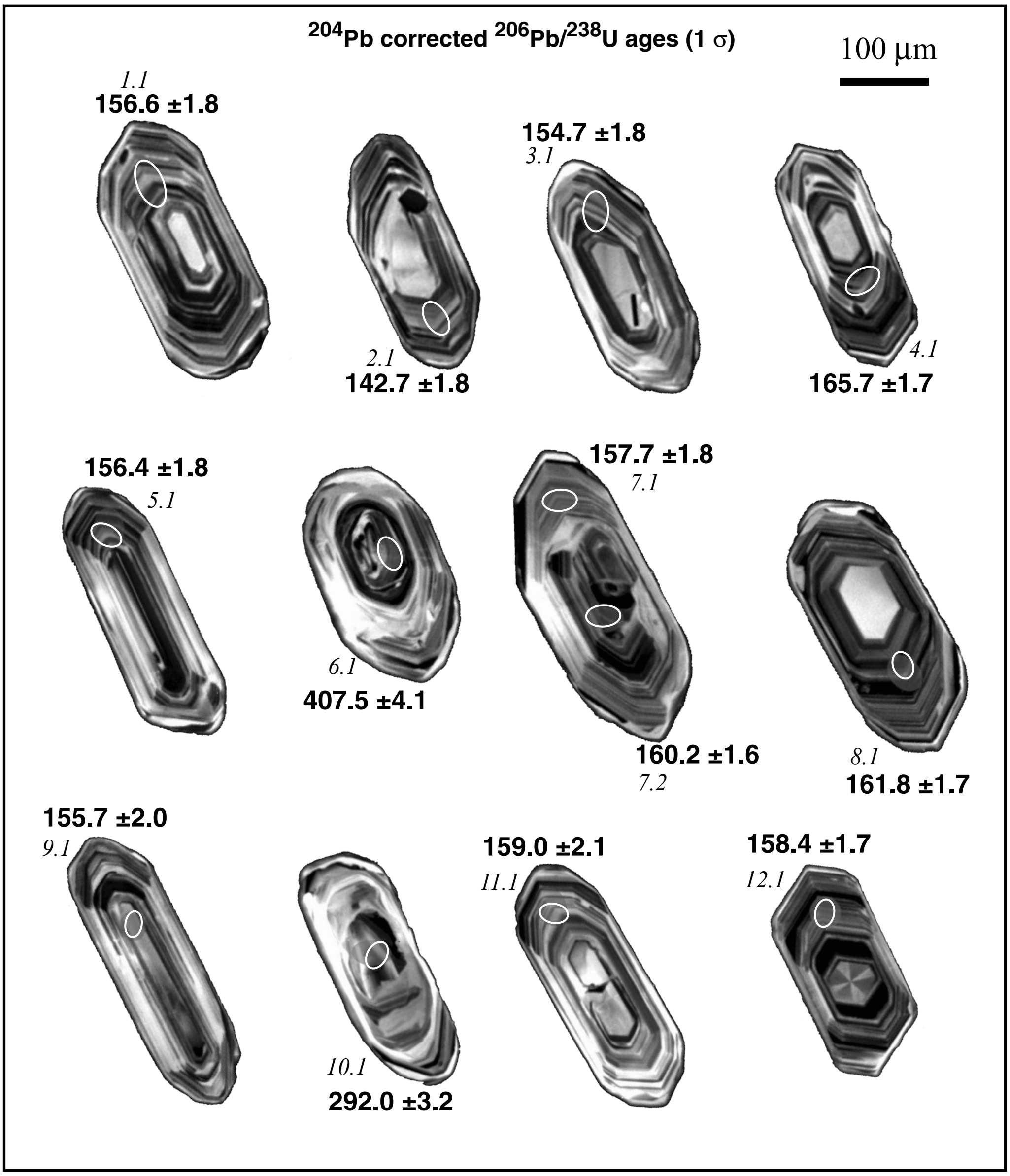

Fig. 5.3.
CL-images with location of analyzed domains show the typical internal structures. Note the textural as well as geochronological core/last igneous-growth relationships. Circles indicate location of analyses and associated $^{206}Pb/^{238}U$ ages (at 1 σ u. l.). Spot numbers correspond to those of appendix 4.

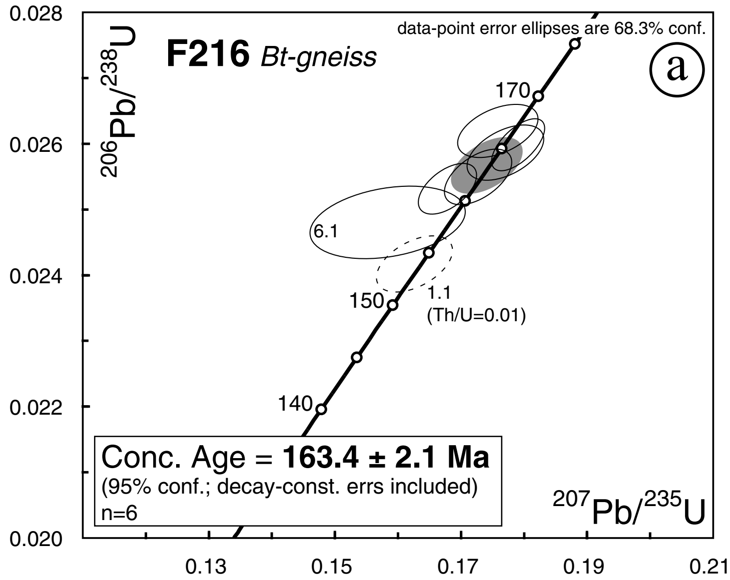

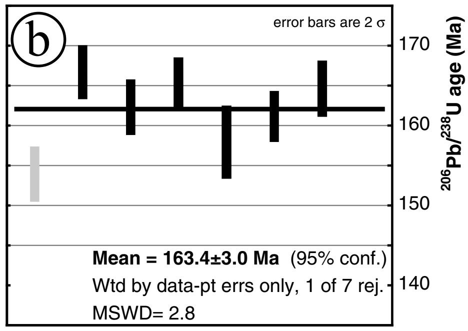

Fig. 5.4.
a) Concordia diagrams of the U-Pb SHRIMP analyses of sample F216 and calculated concordia ages (grey ellipses). Only the ages younger than 200 Ma are reported since they represent the last igneous growth. In dashed line, analytical spots rejected from concordant age calculation (details of data rejection in the text).
b) Mean weigthed average of $^{206}Pb/^{238}U$ ages of the same data set.

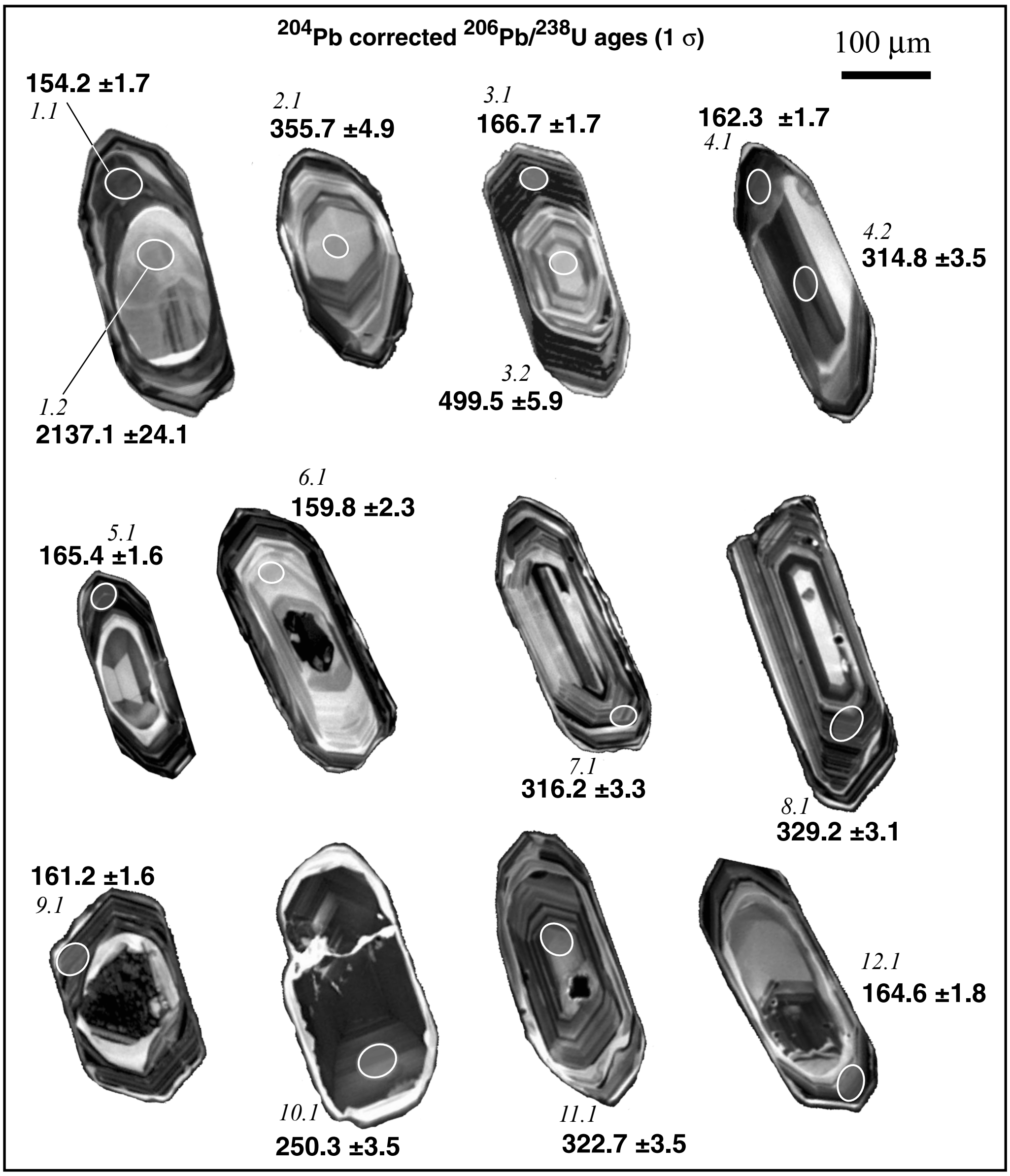

Fig. 5.5. CL-images with location of analyzed domains show the typical internal structures. Note the textural as well as geochronological core/last igneous-growth relationships. Circles indicate location of analyses and associated $^{206}Pb/^{238}U$ ages (at 1 σ u. l.). Spot numbers correspond to those of appendix 4.

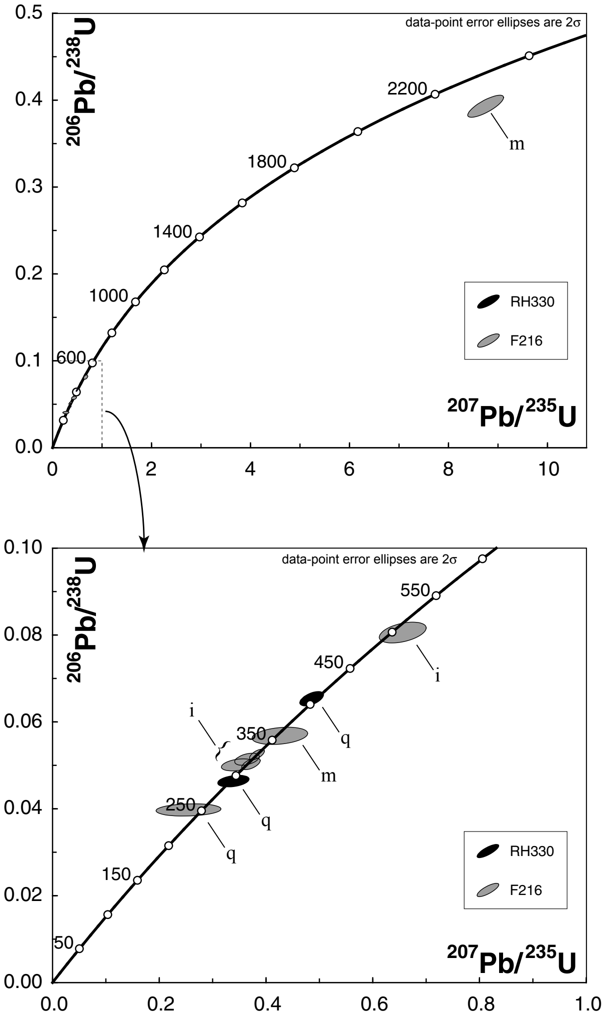

Fig. 5.6.
Concordia diagram of the inherited cores dated within samples F216 and RH330. The type of CL pattern is indicated when identifiable (i: igneous; m: metamorphic; q: questionable) showing the predominance of Permo-Carboniferous igneous ages. This suggests the emplacement of the Late-Jurassic rocks in a crust with Permo-Carboniferous major crustal growth.

respectively) are interpreted as inherited cores (Fig. 5.3 and appendix 4). Spot 2.1 shows no symptom of Pb-loss, neither in CL, nor in its Th-U ratio of 0.29. Although we have no explanation for its younger age, it has been rejected for concordia age calculation because it represents a clear outlier in the data set (Fig. 5.2). After this data rejection, a concordia age of 164.1 ± 2.3 Ma (95%-conf.) is calculated on ten concordant analytical spots, representing the protolith crystallization.

F216:

The sample shows a very high proportion of non-digested relict zircon domains (inherited cores). Sometimes the newly grown domains are extremely limited, less than 10 µm in size (Fig 5.5). The analyses with $^{206}Pb/^{238}U$ ages between 2137 and 250 Ma (spots 1.2, 2.1, 3.2, 4.2, 7.1, 8.1, 10.1 and 11.1 in appendix 4) have been rejected from the calculation of the intrusion age as clearly representing inherited cores. Fig. 5.5 illustrates the textural and geochronological core-rim relationship. Since the intrusion age is represented by the outer igneous domains, only the spots located in these domains have been used to determine the time of the protolith crystallization. Among the analyses fulfilling this criterion, spot 1.1 is younger than the rest of the population, and shows a very low Th-U ratio of 0.01, possible diagnostic for Pb-loss during a metamorphic overprint (e.g. Williams et al. 1996; Hoskin & Black 2000). Thus, the spot was not included in the concordia-age calculation. The concordia age on six concordant analytical spots is 158.0 ± 1.7 Ma (95%-conf.), and represents the intrusion age.

The SHRIMP technique allowed the dating of inherited zircon cores of samples RH330 and F216. (Fig. 5.6). Apart from the discordant Proterozoic core of sample F216 (spot 1.2), the remaining nine concordant core-ages range between 250 Ma and 500 Ma ($^{206}Pb/^{238}U$ ages), with a strong predominance of Permo-Carboniferous igneous ages. The age of these incorporated components therefore suggests that the Late-Jurassic gneisses were originally intruded within a crust having experienced an intense Permo-Carboniferous crustal growth, possibly the equivalent of the Pangeon Unit (see chapter 8 for further discussion).

In order to check the homogeneity of the unit, five additional samples have been dated by the Pb-Pb technique (RH126, F190, F181, F180-2, and F220, Fig. 5.7).

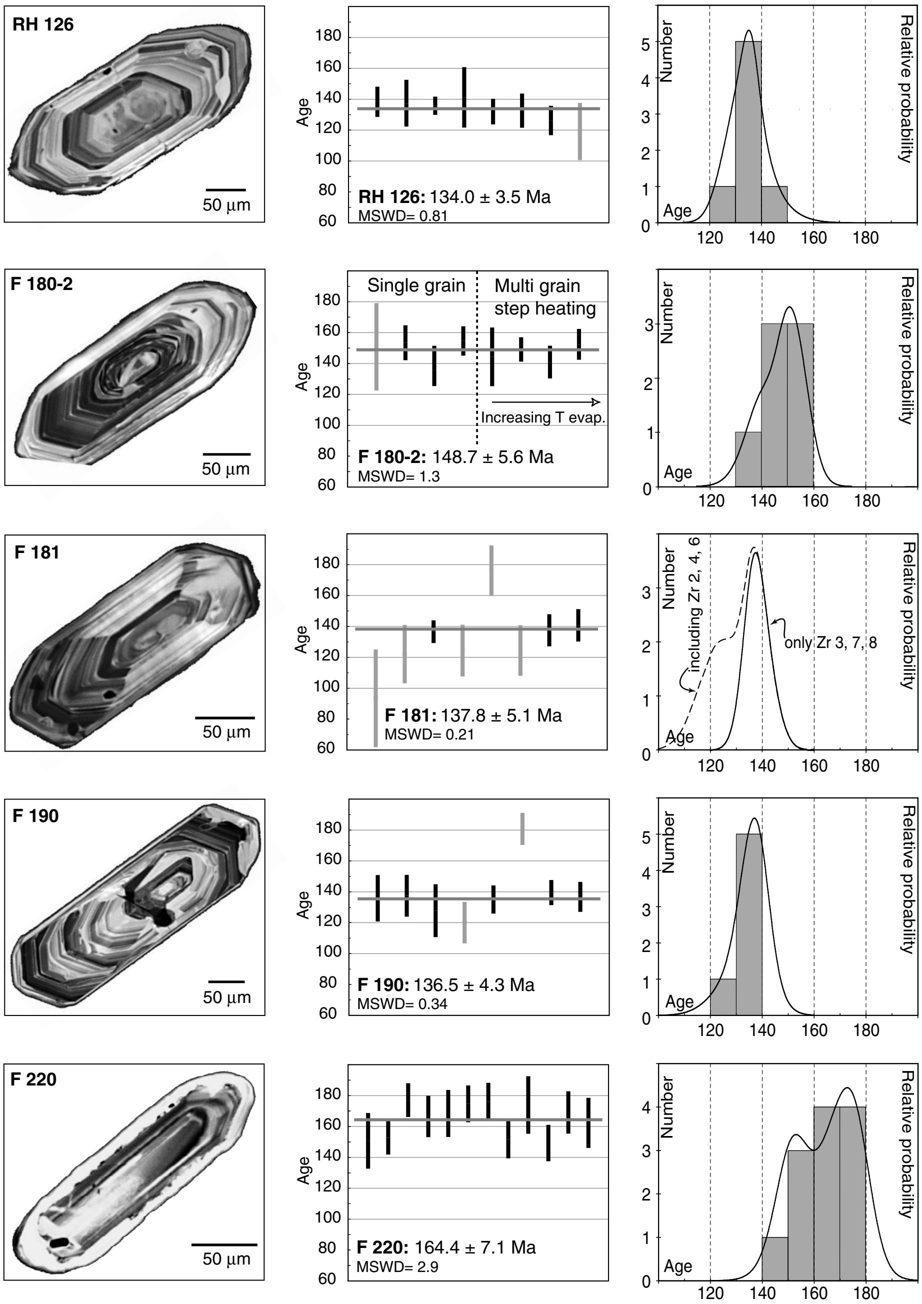

Fig. 5.7.
95% confidence level weighted averages of the zircon Pb-Pb apparent ages, cumulative probability diagrams (after data rejection) and representative cathodo-luminescence images of the dated populations of the Late-Jurassic Early-Cretaceous group. Apparent ages are single-grain measurements, except for samples F180-2 and F220 (see notes on the diagrams and text). All error bars are at the 2 σ level of uncertainty. Data rejected from age calculations are plotted in grey. The bin-size of the cumulative histograms is proportional to the mean 2 σ error on the ages. Measured ratios and errors are given in appendix 3. Dashed lines in cumulative probability curve of F181 is with zircons 2, 4, 6, 3, 7 and 8. Full line, only with zircons 3, 7 and 8.

RH126 and F190:

Samples RH126 and F190 are dated 134.0 ± 3.5 and 136.5 ± 4.3 Ma respectively. Their age-data have normal distributions without major rejection and their CL patterns are typical of igneous zircons; these dates are therefore intrusion ages.

F180-2:

For sample F180-2, the Pb-Pb multi-grain step-heating technique has been applied in addition to the single-grain technique (Kober 1987; Klötzli 1997). The CL images show systematically well preserved igneous zoning. Total-deposition single-grain analyses and step-heating measurements at increasing deposition temperatures yielded similar ages, with a total weighted average of 148.7 ± 5.6 Ma (Fig. 5.7). The age does not change with increasing deposition temperature, proving the homogeneity of the ana-

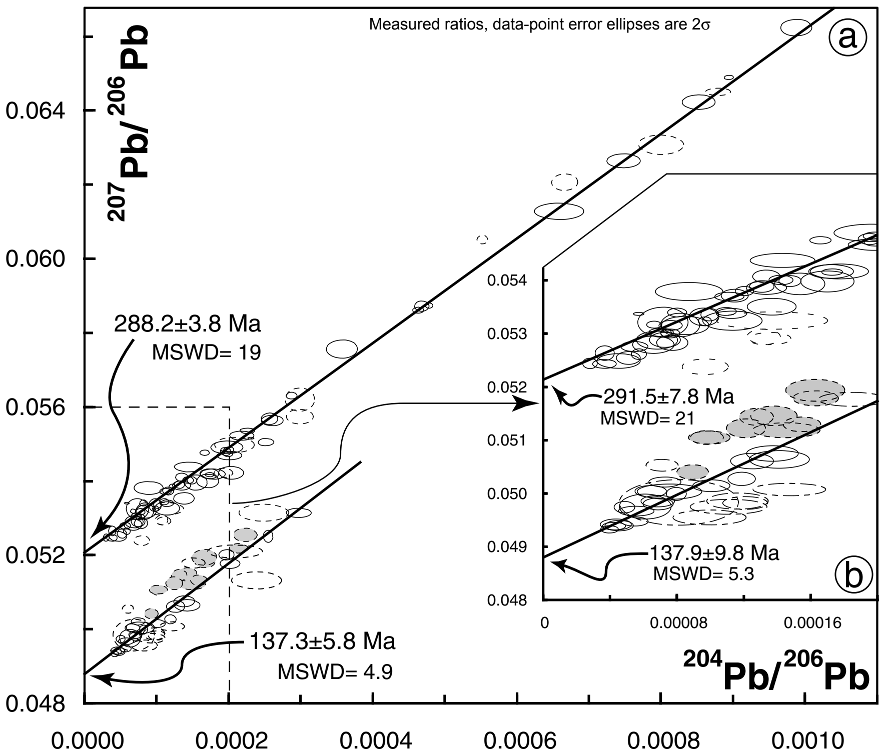

Fig. 5.8. Measured $^{204}Pb/^{206}Pb$ vs. $^{207}Pb/^{206}Pb$ plot of the zircon evaporation analyses with associated 2 σ errors: (**a**) for all data used for age calculation and (**b**) for the measurement with $^{204}Pb/^{206}Pb$ below 0.0002.

A regression line is calculated for each age group. The regression lines are very similar including or not the high $^{204}Pb/^{206}Pb$ measurements. The intercept with the Y-axis and the regression line gives the $^{207}Pb/^{206}Pb$ (and consequently the age) of the zircon group hypothetically without common lead. This shows the validity of the common lead correction, even for high $^{204}Pb/^{206}Pb$ grains, as well as the clear distinction between the two age groups. Note that the measurements of sample F220 (in grey) are not included in the calculation of the age resulting from the regression line calculation. Dashed ellipses represent the measurements rejected from age calculations.

lyzed zircon population.

F181:

Zircons 1 and 5 represent outliers in the data set (attributed to lead loss and inherited cores respectively). The mean age calculated after rejecting these measurements is 134.4 ± 7.1 (MSWD=1.5). Nevertheless, the cumulative probability curve shows a “shoulder” towards younger ages (dashed line in Fig. 5.7), due to zircons 2, 4 and 6 (associated to large errors). This “shoulder” may indicate lead loss, although this is not evidenced in the CL images. Therefore, the weighted average age of 137.8 ± 5.1 Ma, calculated only on the more precise measurements (zircons 3, 7 and 8), probably approximates more closely the true intrusion age.

F220:

All CL images of zircons from this sample show extremely bright rims due to complete recrystallisation during a metamorphic event. This overprint is linked to partial melting. The rims of the zircons were most probably removed during thermal cleaning before measurement. Furthermore, their strong brightness is a sign for very low U and Pb content. They might have a limited participation to the mean Pb content. This is why we consider the final ages to be only slightly affected by the metamorphic lead loss suggested by the CL patterns.

Although slightly older, the 164.4 ± 7.1 Ma mean age of sample F220 is comparable to that of the rest of the group. The cumulative probability curve shows a bimodal distribution. This might be due to the fact that we used two-three zircons instead of only one per analyses. This dating on population increases the chances of incorporating inherited components. The intrusion might be either 152.5 ± 7 (n=4) or 172.1 ± 5.2 (n=8). The determination of an accurate intrusion-age is difficult with this data set. Nonetheless, we attribute this sample to the Jurassic-gneisses, with important geological implications because of its location in the lower part of the Bt-gneiss unit (Fig. 8.1).

The Pb-Pb ages are in the range of those obtained by the SHRIMP technique, although sometimes slightly younger. Thus, we interpret the rocks dated between 135 and 165 Ma by the evaporation

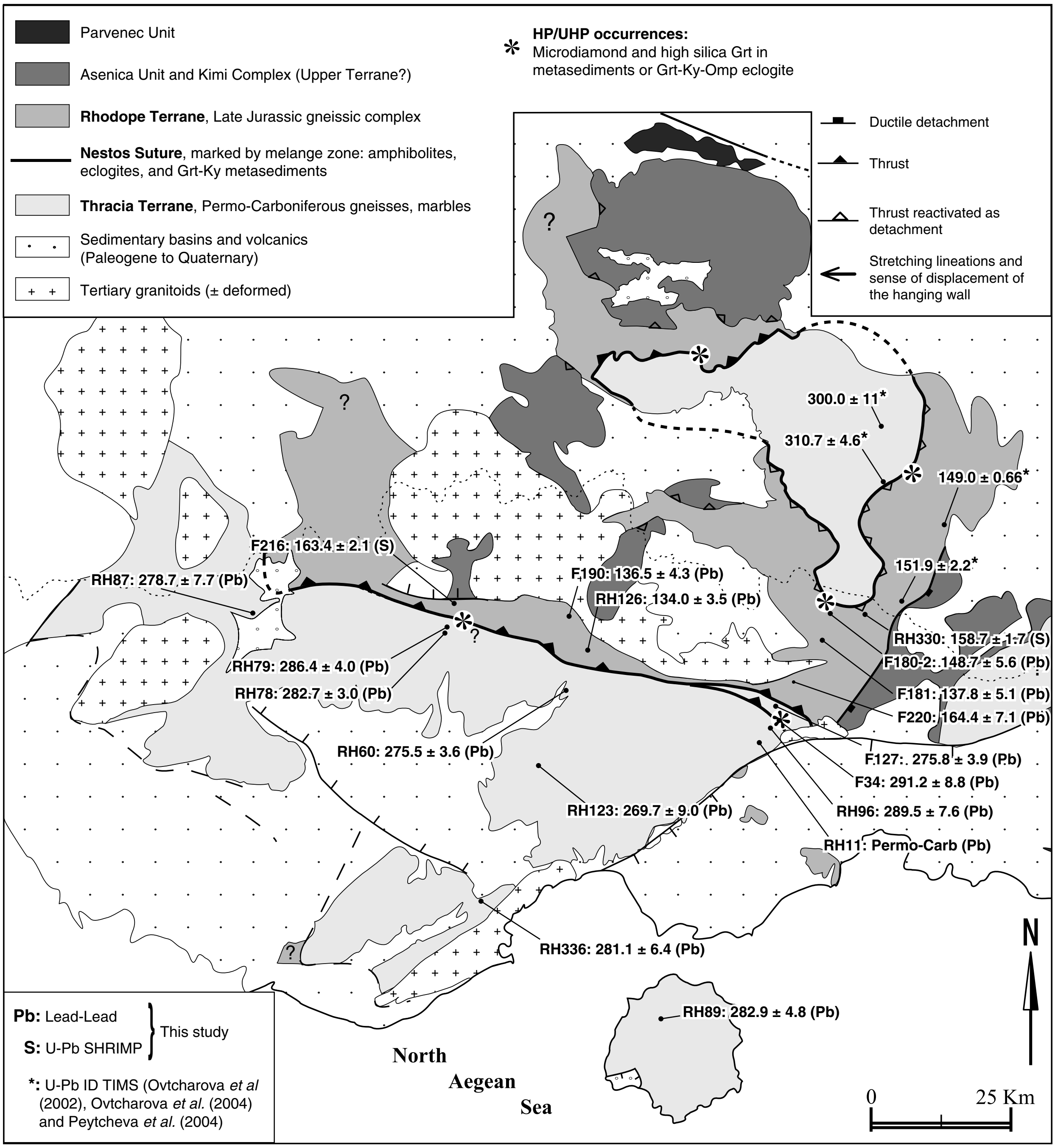

Fig. 5.9.
Sketch map of the Central Rhodope summarizing the orthogneiss protolith-ages obtained in this study. The zircon U-Pb ID-TIMS protolith ages (in Ma) on orthogneisses in Bulgaria from Ovtcharova *et al.* (2002), Ovtcharova *et al.* (2004) and Peytcheva *et al.* (2004) are reported (marked by a star). For each age, the correspondent dating method is indicated (Pb-Pb or SHRIMP).

technique as belonging to the same age group (and gneissic unit) as the Late-Jurassic gneisses dated by SHRIMP. The U-Th-Pb analyses allow a control on the concordance of the ages, as well as a direct interpretation of their geological meaning. As a result, they are the more accurate, and therefore we will refer to this group of samples as the Late-Jurassic orthogneisses.

A separation in two distinct age groups is also clear in the plot of measured $^{207}Pb/^{206}Pb$ vs. $^{204}Pb/^{206}Pb$ values of Fig. 5.8. A regression line is drawn for each age group. The regression lines are very similar either including or excluding the high $^{204}Pb/^{206}Pb$ measurements. The intercept with the Y-axis and the regression line gives the $^{207}Pb/^{206}Pb$ and consequently the age for each age group of the zircon hypothetically without common lead component. The intercept ages for the older group of samples, excluding the analyses already rejected, are similar whether including or not the measurements with $^{204}Pb/^{206}Pb$ above 0.0002 (288.2 ± 3.8 and 291.5 ± 7.8 Ma respectively). In the case of the younger group, excluding sample F220, these ages are also equivalent, including or not the measurements with high $^{204}Pb/^{206}Pb$ (137.3 ± 5.8 and 137.9 ± 9.8 Ma respectively). These calculations show the validity of the common lead correction, even for grains with high $^{204}Pb/^{206}Pb$.

In summary, this geochronological study clearly defines two intrusion age groups: Permo-Carboniferous and Late Jurassic.

Chapter 6

Mineralogy and whole-rock chemistry of the orthogneisses

This chapter exposes the petrological characteristics of the dated orthogneisses. Their whole-rock geochemistry is also presented and discussed.

Mineralogy

Most of the studied rocks are foliated, but some of the Late-Jurassic orthogneisses still exhibit magmatic textures. The main mineralogical phases , macroscopically recognizable, are: quartz, feldspars and micas. The two age-groups show nonetheless some petrographic dissimilarities. The Permo-Carboniferous orthogneisses have often augen textures, contain Kfs, and often Bt together with Mu (Table 6.1). Instead, the Late-Jurassic orthogneisses are Pl- and Bt-bearing, with occurrence of Hbl (e.g. RH330, F180-1, F190). They rarely contain muscovite. These petrographic characteristics suggest an evident “I-type” affinity for the Late-Jurassic

Table 6.1. Summary of the mineralogy of the studied orthogneisses. Location of the samples in Fig. 4.8

age group	Sample	Rock type	Mineralogy
Permo-Carboniferous	RH11	Leucocratic gneiss	Qtz, Kfs, Mu, op, Zrn
	RH60	Augen gneiss	Qtz, Kfs, Bt, Mu, Ep(II), Chl (II), Ttn, Pl, Zrn
	RH78	Bt-gneiss	Qtz, Kfs, Ep, Bt, Ttn, Zrn
	RH79	Augen gneiss	Qtz, Kfs, Mu, Bt, Zrn
	RH87	Bt-gneiss	Qtz, Pl, Bt, Kfs, Ep, Ttn, Zrn
	RH89	Augen gneiss	Qtz, Kfs, Mu, Bt, Zrn
	RH96	Augen gneiss	Qtz, Kfs, Mu, Bt, Zrn
	RH123	Leucocratic gneiss	Qtz, Kfs, Mu, Zrn
	RH336	Leucocratic gneiss	Qz, Fl, Mu, Bt
	F34	Augen gneiss	Qtz, Kfs, Chl (II), Bt, Mu, Pl
	F127	Augen gneiss	Qtz, Kfs, Pl, Bt
	RH132	Augen gneiss	Kfs, Qtz, Pl, Bt, Chl (II), Mu, Zrn
	RH31	Augen gneiss	Qtz, Kfs, Pl, Bt, Chl (II), Op, Ttn
	RH311	Leucocratic gneiss	Qz, Kfs, Mu
	RH323	Augen gneiss	Qz, Fs, Bt, Mu
Late Jurassic/Early Cretaceous	RH126	Bt-granite	Qz, Pl, Bt, Ttn, Zrn
	RH330	Bt-Amp gneiss	Qtz, Pl, Amp, Bt, Ttn, Op (Py...)
	F180-2	Bt-Amp gneiss	Qtz, Pl, Amp, Bt, Op (Py...)
	F181	Bt-granite	Qtz, Pl, Bt, Chl(II), Op, Mu, Zrn
	F190	Bt-gneiss	Pl, Qtz, Bt, Amp, Ep, Ttn
	F216	Bt-gneiss	Pl, Qtz, Bt, Zrn
	F220	Bt-migmatitic gneiss	Qtz, Bt, Pl, Kfs, Grt(II)
	F180-1	Bt-Amp gneiss	Pl, Qtz, Amp, Bt, Chl (II), Op, Grt (incl. in Pl), Zrn
	F203	Bt-gneiss	Qz, Pl, Bt
	F206	Bt-gneiss	Qtz, Pl, Bt, Chl (II), Op, Zrn
	F207	Bt-gneiss	Qtz, Pl, Bt, Op, Chl (II), Ap, Grt, Zrn
	F224	Bt-gneiss	Qtz, Pl, Bt, Chl (II), Op, Ttn, Grt (incl. in Pl), Zrn
	F225	Bt-gneiss	Qtz, Pl, Bt, Mu, Grt (incl. in Pl), Zrn
	F226	Bt-gneiss	Qtz, Pl, Bt,Chl (II), Grt (incl. in Pl), Op, Zrn

II: secondary
Op: opaque

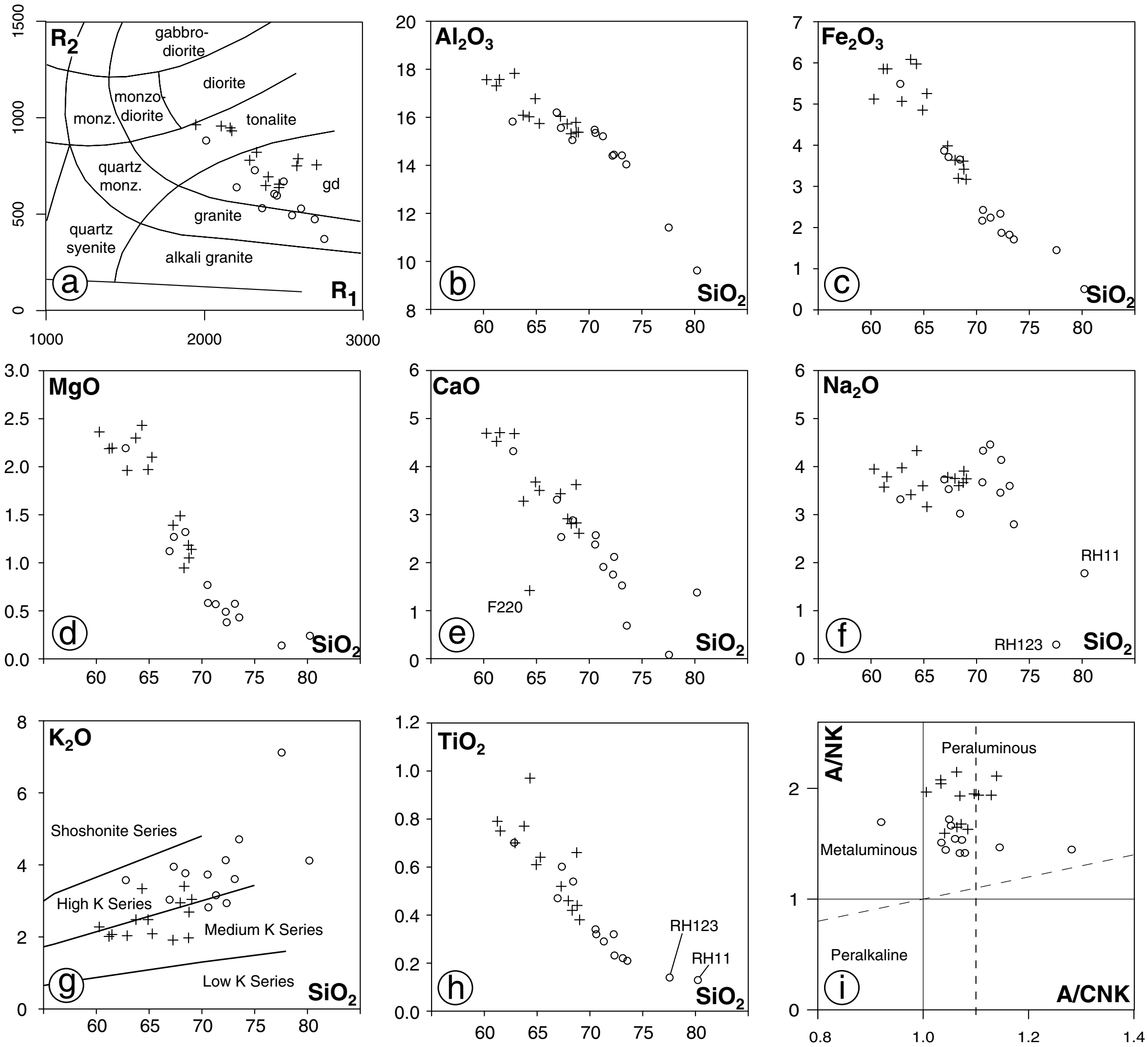

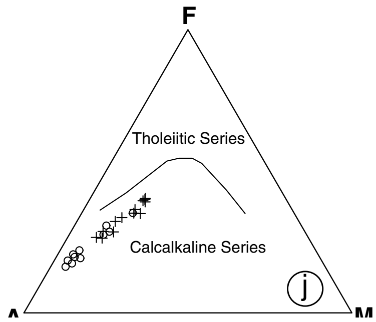

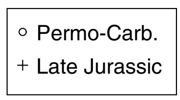

Fig. 6.2.

(**a**) Classification R1-R2 diagram of De La Roche *et al.* (1980). (R1= 4Si - 11(Na + K) - 2(Fe + Ti), R2= 6Ca + 2Mg + Al).

(**b-h**) Variation diagrams of selected major elements vs. SiO2. Trends are similar to those caused by magmatic differentiation. The Late-Jurassic gneisses as a whole are more mafic than the Permo-Carboniferous gneisses.

(**i**) Plot of ACN/K versus A/NK.

(**j**) AFM diagram of Irvine & Baragar (1971) showing the calc-alkaline affinity of both groups of orthogneisses. A= Na2O+K2O; F=FeOt; M=MgO.

gneisses, as compared to the Permo-Carboniferous ones (Chapell & White 1974).

Geochemistry

The Permo-Carboniferous gneisses are mainly granites and granodiorites, whereas the Late-Jurassic gneisses are more mafic granodiorites or tonalites (de La Roche *et al.* 1980, Fig. 6.2.a). Furthermore, the Late Jurassic rocks are systematically richer in Cr, Ni, Cu, and Co (Appendix 5a and 5b), suggesting a lower degree of differentiation than the Permo-Carboniferous ones.

The variation diagrams of Fig. 6.2 show trends similar to those caused by magmatic differentiation. Although the samples of each group are not considered as comagmatic, major elements such

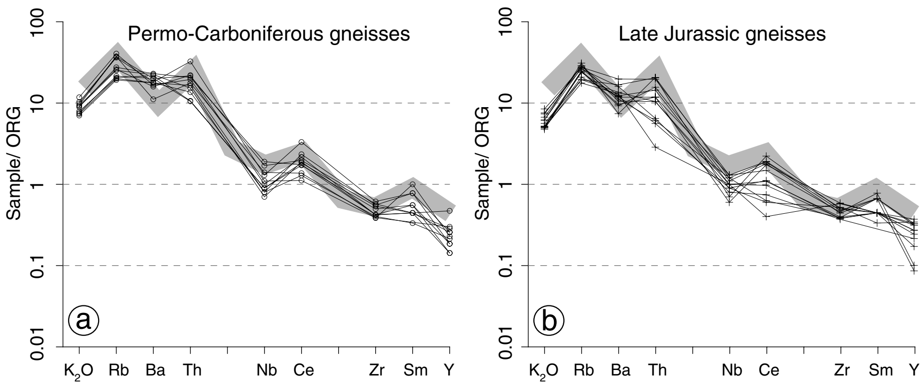

Fig. 6.3.
Whole-rock multi-elements diagram, normalized to a hypothetic oceanic ridge granite (ORG of Pearce *et al.* 1984) for the Permo-Carboniferous (**a**) and Late-Jurassic orthogneisses (**b**). The volcanic arc granite from Chile of Pearce *et al.* (1984) is shown in grey for comparison.

as Ti, Al, Fe, Mg, Ca show decrease of abundance with increasing Si content. The concentrations of these elements are therefore only slightly disturbed by metamorphism and alteration, and can be used to characterize the protoliths. The diagrams CaO vs. SiO_2, NaO vs. SiO_2 and K_2O vs. SiO_2 (Fig. 6.2 e f and g) show samples RH11, RH123, and F220 plotting far off the trends defined by the other samples. This is probably due to metamorphic alteration. F220 is strongly migmatitic and RH11 and RH123 are mylonitic leucocratic gneisses. The zircons from RH11 and RH123 show systematically numerous cracks suggesting an important deformation and alteration (Fig. 5.1 and appendix 2). Thus RH11, RH123 and F220 are not used for the following interpretation.

The scattering of K_2O content of the samples might reflect metamorphic disturbance (Fig. 6.2.g). However, most of the Jurassic samples belong to a medium-K series. In contrast, the Permian samples belong to a high-K series. This difference is in agreement with the mineralogical observation of Kfs only in the Permo-Carboniferous orthogneisses. Therefore, despite its scatter, the K_2O content, at least to some extend, represents an original feature confirmed by the difference in CaO and Ba contents (Fig. 6.2.e, appendix 5a and 5b).

The orthogneisses of both age-groups are slightly peraluminous. A/CNK values range between 0.92 and 1.37 for the Permo-Carboniferous gneisses (cluster between 1 and 1.10) and between 1 and 1.15 for the Jurassic ones. This predominance of A/CNK values allows to classify the granitoids of both age-groups as I-type granitoids (Chappel & White 1974). Moreover, both are calc-alkaline in the diagram of Irvine & Baragar (1971) in Fig. 6.2.j.

In the multi-element diagrams normalized to ORG (Pearce *et al.* 1984; Fig. 6.3), all orthogneisses show depletion in moderately incompatible elements as Zr, Sm and Y, and display a Nb anomaly. The same diagram shows the strong enrichment in highly incompatible elements such as K, Rb, Th and Ba, as well as the clear similarity between the

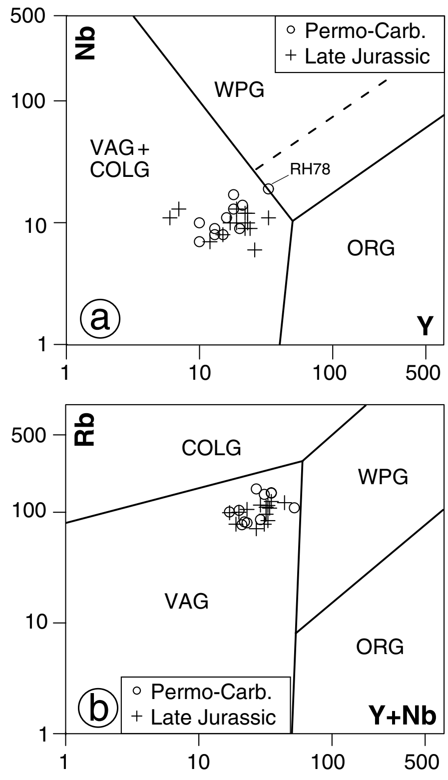

Fig. 6.4.
Granite tectonic-setting discrimination diagrams of Pearce et al. (1984): Y vs. Nb (**a**), Y+Nb vs. Rb (**b**). VAG: volcanic arc granites; ORG: oceanic ridge granites; WPG: within-plate granites; COLG: collisional granites.

analyzed samples and the volcanic-arc granites of Pearce *et al.* (1984). All these features are possible properties of volcanic-arc granitoids, but also of syn-or post-collisional granites (Pearce *et al.* 1984). Furthermore the samples plot in the volcanic arc field of the Rb vs. (Y+Nb) and Nb vs. Y diagrams (Fig. 6.4; Pearce *et al.* 1984) suggesting a volcanic arc origin for these rocks. In the discussion, we will integrate these geochemical data to their geological and geochronological contexts.

Chapter 7

Metamorphic study of Grt-Ky schists from the "melange" zone

One of the major problematics in the Greek Rhodope concerns the lateral prolongation of the UHP melange zone north of Xanthi (Barr *et al.* 1999; Mposkos & Kostopoulos 2001). Until now, the UHP Xanthi locality is isolated, and so far no study explicitly described an eventual lateral continuation. A first hint comes from the zircon dating. The protolith of the orthogneisses provides evidence for the location of the contact between the two units already described in chapter 4 (Pangeon Unit and Rhodope Terrane). Furthermore, field observations revealed an important volume of amphibolites (± Grt) close to the Nestos River south of Sidironero (see also the map of Kronberg 1969). All these facts suggest a westward continuation of the melange zone bearing the UHP relicts.

In order to provide constrains on this issue, we sampled the best candidate for having experienced UHP metamorphism (sample F101, located in Fig 4.2 and 4.8). This Grt-Ky micaschist comes from the contact between the two units defined by the structural study and protolith dating (Pangeon Unit and Rhodope Terrane). In order to check if these two units are distinct terranes, we need to characterize the nature of their contact. In other words to know if other UHP rocks can be found within the melange zone westward from Xanthi and if we can correlate the two cross sections presented in chapter 4 also on the basis of metamorphic petrology.

Mineral abbreviations are after Kretz (1983), end-member abbreviations are from Powell *et al.* (1998).

Outcrop, sample description, and petrography:

The outcrop in which sample F101 was collected displays a high lithological variability. Layers of orthogneisses, migmatites, mylonites, marbles, Grt-micaschists, amphibolites and epidote-rich amphibolites alternate at the decimetre-scale. All these lithologies occur in a thickness of less than 20 metres. This justifies the "melange zone" terminology used throughout this work. Mylonites separate this melange zone from overlaying decametric boudins of Grt-Bt and Grt-Cpx-Pl migmatites.

Sample F101 belongs to an horizon of Grt-micaschist which is less than one metre-thick. It consists of Grt and Ky porphyroblasts (both sometimes centimetric in size) within a strongly foliated matrix of quartz, muscovite, biotite and rare plagioclase. The reddish-brown biotites are generally restricted to pressure shadows around garnets and indicate a top-to-the-SW shear sense. Appearance of biotite seems to be related to the retrogression of garnets. Abundant reddish-brown rutiles are present both within the matrix and included in garnet. The garnets often show rutile and quartz needles with an extremely high length-width ratio, these needles are very thin, elongated (often lenght of 100 μm and width of about 1 μm). They systematically follow crystallographic orientations (Fig. 4.3 and 7.1). These feature allows a clear distinction between rutile needles and inclusion. Microprobe analyses

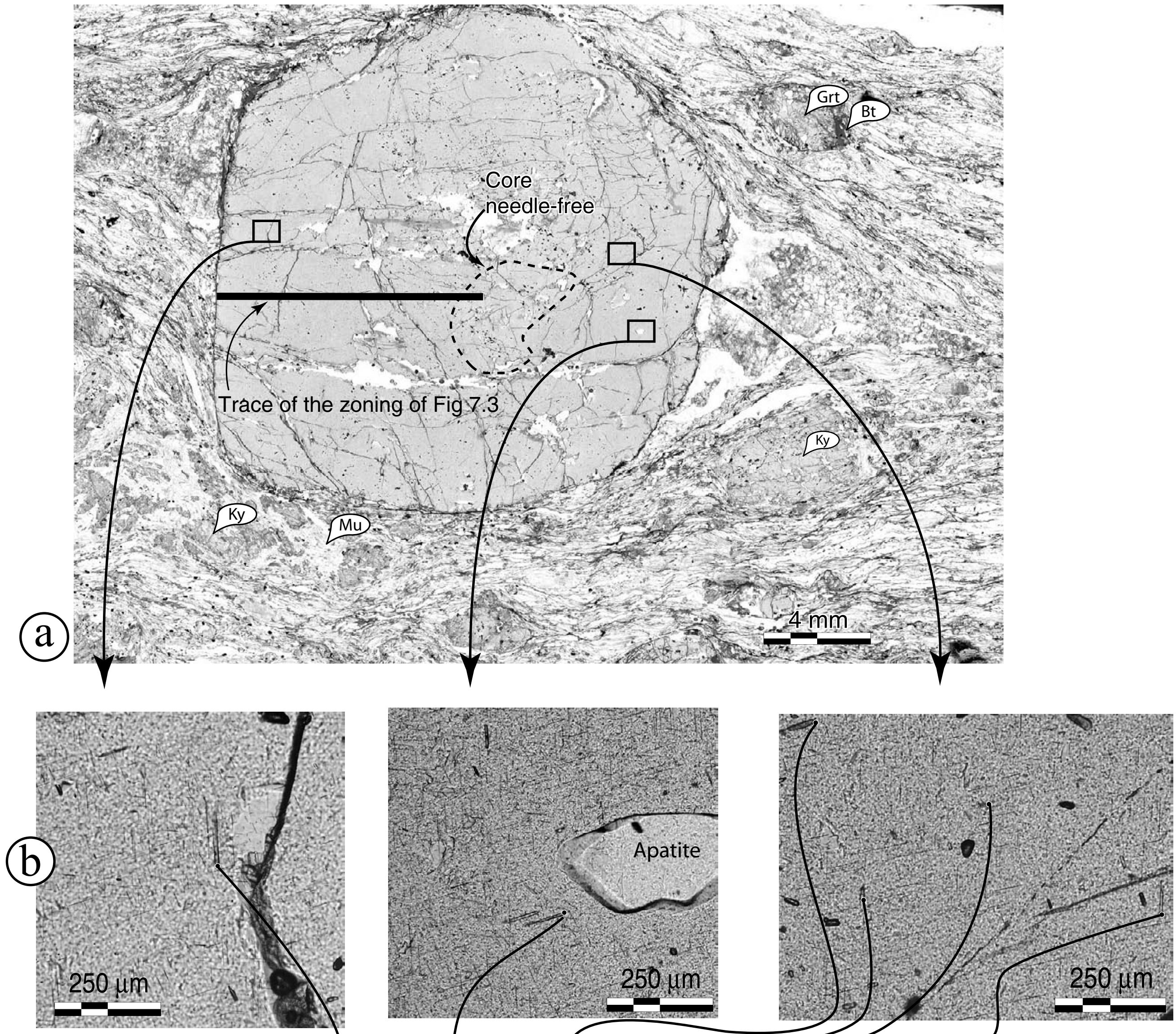

c

	Qz	*Rt**	*Rt*	*Qz*	*Qz*	*Qz**
Na_2O	0.00	0.00	0.01	0.00	0.01	0.00
SiO_2	**91.02**	6.85	0.08	**100.52**	**100.30**	**85.15**
K_2O	0.01	0.00	0.01	0.00	0.01	0.02
TiO_2	0.02	**80.01**	**98.24**	0.00	0.03	0.00
FeO	1.68	6.31	1.77	1.04	1.05	7.59
Al_2O_3	1.03	4.11	0.05	0.15	0.05	3.42
MgO	0.25	0.87	0.00	0.02	0.00	0.94
CaO	0.05	0.22	0.04	0.00	0.02	0.17
Cr_2O_3	0.05	0.10	0.06	0.09	0.07	0.05
MnO	0.05	0.31	0.04	0.05	0.02	0.25
Total	94.15	98.78	100.29	101.89	101.57	97.59

** : analyses mixed with the host garnet*

Fig 7.1.
a) Microphotograph of the thin section of sample F101-1. Note the size of garnet and kyanite. Assymetric tails on both sides of the garnet porphyroblast are made of quartzo-feldspatic material. Note that kyanite is partly retrogressed to muscovite.
b) Microphotographs of the rutile and quartz needles within the garnet-porphyroblast with location of the analysed points. Note the systematic crystallographic orientation of the needles. Only needles with a large enough outcropping-surface have been analyzed. They are parallel to the thinner ones and therefore interpreted to belong to the same generation.
c) Microprobe analyses of the quartz and rutile needles. Note that some analyses are mixed with the host garnet due to small outcropping surface.

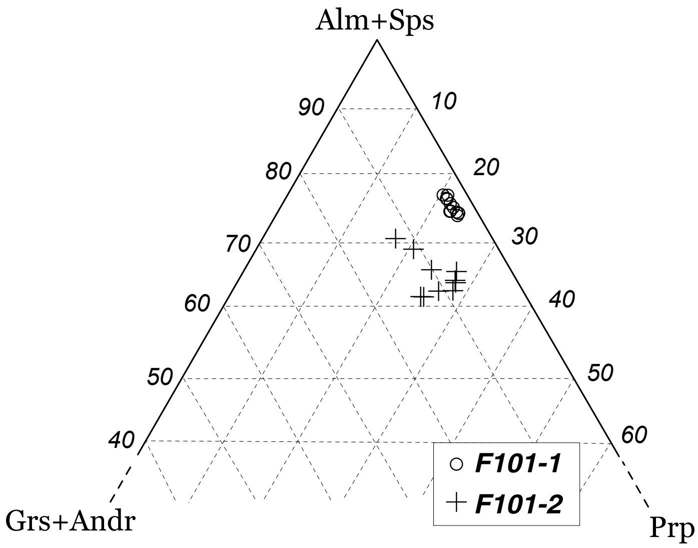

Fig. 7.2.
Ternary diagram of the end member proportions of the analyzed garnets in thin sections F101-1 and F101-2.

confirmed that these needles consist of quartz and rutile (Fig. 7.1). We do not consider them as inclusions but on the contrary propose that these needles represent exsolutions from a high Si-Ti content garnet precursor. Other accessory phases are represented by apatite, zircon and monazite.

Mineral assemblages of two thin-sections (respectively F101-1 and F101-2) of this Grt-Ky schist have been analyzed with a JEOL JXA-8900RL superprobe at Mainz University (Germany). F101-1 is a Grt-Ky schist whose Grt and Ky can reach sizes of 2 cm. (Fig. 7.1). On the other hand, F101-2 is more fine-grained and shows clear top-to-the-SW ductile shearing (asymmetric biotite-tails around the garnets of Fig. 7.6). The analyses used for thermobarometric calculations are given in Appendix 6.

X_{Mg} values represent Mg/(Fe+Mg).

Garnet end-member proportions are calculated as follow:

X_{Alm}= 100Fe $^{2+}$/(Mg+Fe^{2+}+Mn+Ca)
X_{Andr}=100Fe^{3+}/(Al^{VI}+Cr+Fe^{3+}+Ti)
X_{Gros}=100Ca/(Mg+Fe^{2+}+Mn+Ca)-X_{Andr}
X_{Prp}=100Mg/(Mg+Fe^{2+}+Mn+Ca)
X_{Sps}=100Mn/(Mg+Fe^{2+}+Mn+Ca)

Mineral chemistry

Garnet:

The analyzed garnets are typically almandine (ca. Alm $_{70-60}$) and pyrope rich (Prp $_{20-25}$) and have relatively homogeneous compositions (Fig. 7.2). In F101-1, the end member proportions are $Alm_{70-73}Andr_{0-5}Grs_{0-2}Prp_{20-24}Sps_{3-4}$. In F101-2, the end member proportions are slightly different: $Alm_{58-63}Andr_{0-2}Grs_{5-10}Prp_{24-26}Sps_{2-5}$. The compositional zoning of one porphyritic garnet of sample F101-1 (Fig. 7.3, located in Fig. 7.1) shows slight increase of pyrope content and decrease of almandine content towards the rim.

Biotite:

The X_{Mg} of the biotites in F101-2 is homogeneous and varies between 0.51 and 0.54. In accordance with their reddish colour, Ti-content of the biotites ranges between 2 and 2.30 Wt% suggesting a relatively high equilibration temperature.

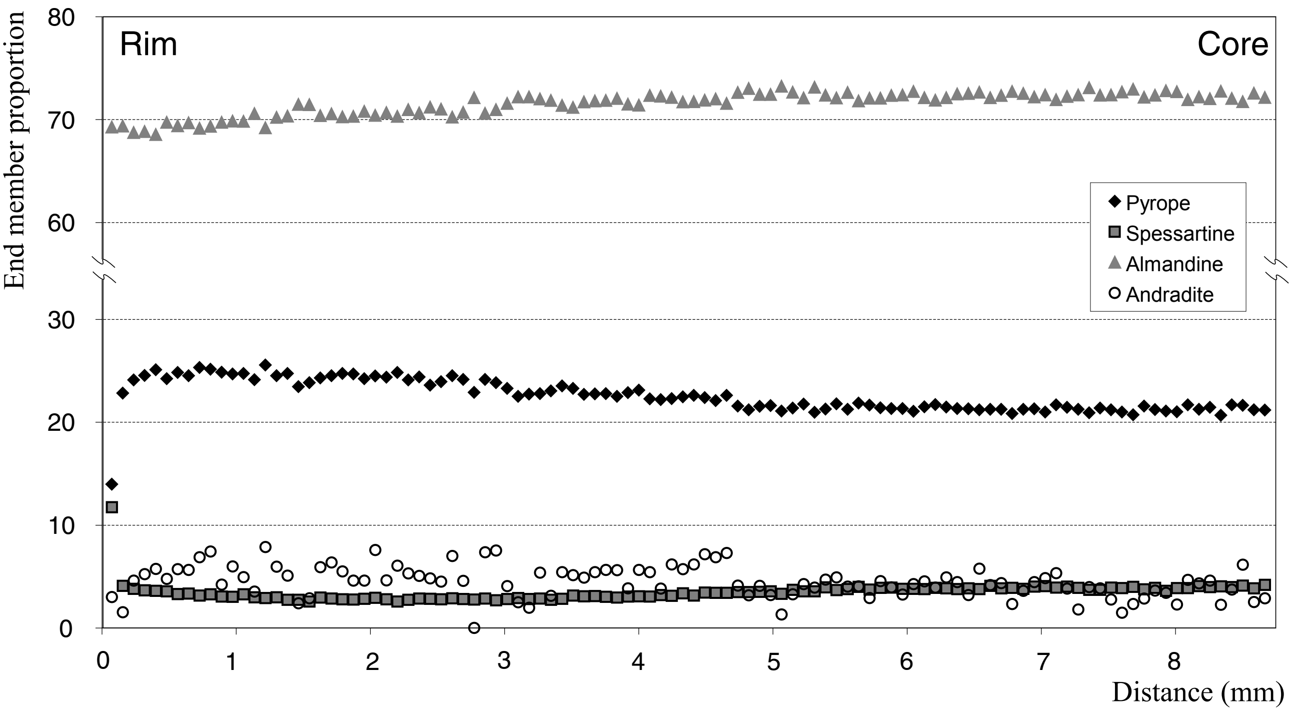

Fig. 7.3.
Compositionnal zoning profile of a porphyriritic garnet from F101-1. Location of the profile is shown in Fig. 7.1. The composition of the garnet is almost homogeneous but note the slight increase of pyrope and andratite content from core to rim associated with a decrease of alamandine proportion.

Muscovite:

Muscovites have Si contents ranging from 3.06 to 3.16 p.f.u. (normalized to 11 O). One of the analyzed mineral, included in a garnet showed higher Si content of 3.2.

Feldspar:

The analyzed feldspars are Na-rich plagioclases. Their composition varies between Ab_{91} and Ab_{65} (Fig 7.4). Plagioclases analyzed in sample F101-1 show a smaller compositional variation than those in F101-2. These typical composition is between Ab_{91} and Ab_{85}.

Thermobarometry

PT estimates of retrogressive equilibration in the previously described samples (F101-1 and F101-2) were made using multi-equilibria calculations. The software THERMOCALC 3.2.1 was used in Average PT mode (Powell & Holland 1994) using the dataset of Holland and Powell (1998; 1999 update). The assemblages Grt-Bt-Pl-Mu-Ky (+Qz, H_2O) were used. In the case of F101-2, as Ky was not observed in thin section, the latter phase was omitted. End-members activity and uncertainties were calculated with the AX program (available at http://www.esc.cam.ac.uk/astaff/holland/). In case of lack of muscovite adjacent to the equilibration volume, the composition of the muscovite from the matrix

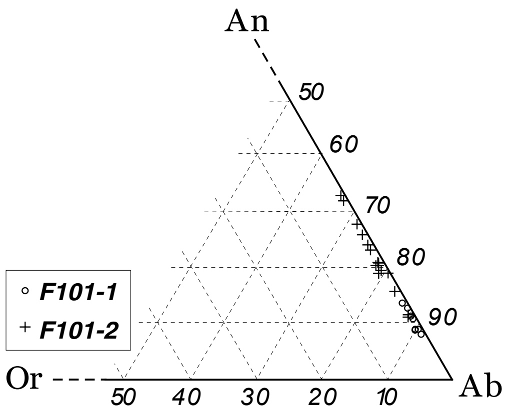

Fig. 7.4.
Ab-An-Or ternary diagram of the analyzed feldspars in F101-1 and F101-2.

has been used in the calculation. This assumption is justified by the homogeneity of the analyzed muscovites. The main source of uncertainty in such calculations is the composition of the minerals in equilibrium. This is why several possible compositions have been used (sometimes even extreme, possibly unrealistic). Fig 7.5 and 7.6 show spot location and details the mineral assemblages used for thermobarometric estimations. For instance, in sample F101-1, garnet core and rim compositions have been used, and produced no significant difference in the results.

Repeated equilibrium-PT results are consistent within error for the two samples (Fig 7.5 and 7.6). For F101-1, pressure vary from 11.1 ± 1.5 to 11.7 ± 2 Kbar and temperature varies between 733 ± 39 and 737 ± 26 °C. In F101-2, the pressure is estimated from 10.2 ± 1.4 to 11.8 ± 1.9 Kbar and the temperature from 753 ± 54 to 689 ± 40°C. Uncertainties on the chemical composition of the phases in equilibrium have no significant influence on the obtained PT conditions. In the case of sample F101-2, these equilibration conditions are based on the assemblages that formed in pressure shadows around garnets. These σ tails indicate a top-to-the-SW sense of shear.

Discussion and conclusions

The garnet compositional zoning of Fig 7.3 could be interpreted in terms of prograde growth, although it is weakly defined. However, the Qz and rutile needles are interpreted as a reequilibration feature. Consequently, the apparent zoning illustrated in Fig. 7.3 is thought to result from the "erasing" of an earlier zoning (possibly growth-zoning) by reequilibration processes.

Although no direct evidence for UHP metamorphism was found (e.g. coesite or diamond), sample F101 can have experienced UHP conditions because of the presence of exsolved quartz and rutile needles in the garnet porphyroblasts. This is the expression of a high Si-Ti garnet precursor, probably due to HP or UHP conditions of growth, prior to reequilibration at lower pressures. Thus we propose that the "melange"/UHP zone in the Greek central Rhodope forms a continuous belt, along strike, extending from north of Xanthi to at least the Nestos River south of Sidironero (and most probably until Katonevrokopi, personal observations). This also confirms the protolith age-distribution presented in chapter 5 (see Fig 5.9) and correlates with the almost continuous observation of a amphibolite-rich zone from Xanthi area to Katonevrokopi (Kronberg 1969 and personal observations).

Finally, the thermobarometric results suggest that the top-to-the-SW ductile shearing is associated with reequilibration at a pressure of 10.2 ± 1.4 to 11.8 ± 1.9 Kbar and temperature from 753 ± 54 to 689 ± 40°C.

Average PT estimates of F101-1

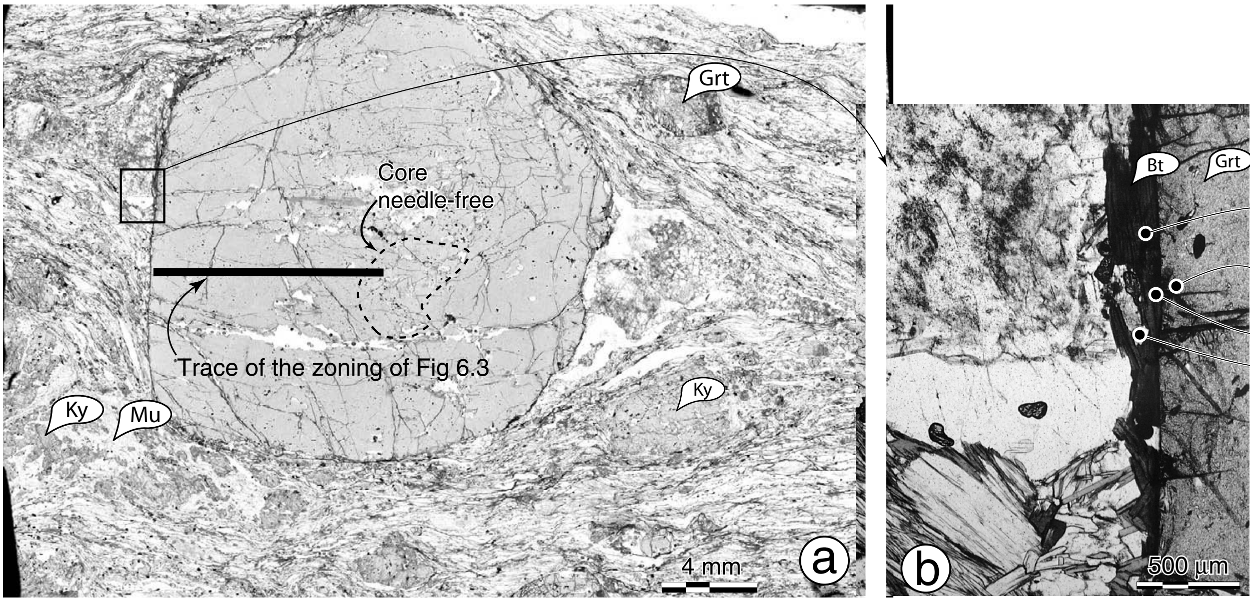

1: Grt 81/Bt82/Pl84/Mu119/Ky
T = 737°C, sd = 26,
P = 11.6 kbar, sd = 1.3,
cor = 0.759, sigfit = 1.07

2: Grt 81/Bt83/Pl84/Mu119/Ky
T = 737°C, sd = 32,
P = 11.5 kbar, sd = 1.6,
cor = 0.759, sigfit = 1.31

3: Grt394/Bt82/Pl84/Mu119/Ky
T = 733°C, sd = 39,
P = 11.7 kbar, sd = 2.0,
cor = 0.764, sigfit = 1.59

4: Grt386/Bt82/Pl84/Mu119/Ky
T = 734°C, sd = 29,
P = 11.1 kbar, sd = 1.5,
cor = 0.760, sigfit = 1.18

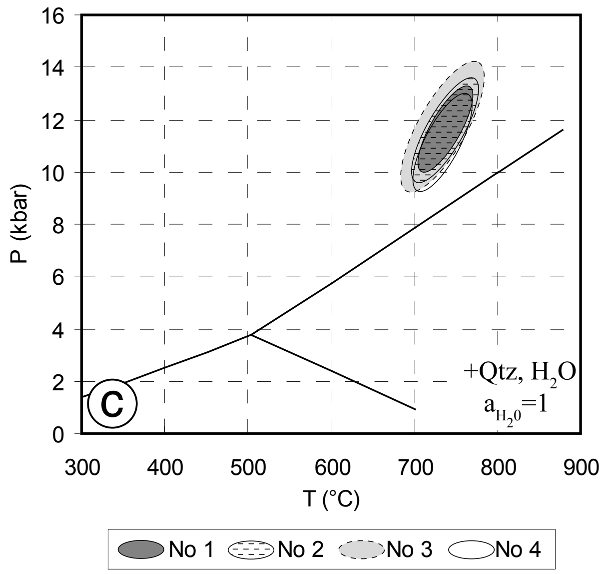

Independent set of 6 reactions used for the 4 calculated intercepts:

gr + 2ky + q = 3an
3an + pa = gr + ab + 3ky + H_2O
3east + 6q = py + phl + 2mu
phl + east + 6q = py + 2cel
py + 3east + 4q = 3phl + 4ky
ann + 2ky + q = alm + mu

Fig. 7.5.
a) Microphotograph of F101-1 thin section with location of the analyzed area.
b) Location of analyzed points.
c) Plot of the error-ellipses obtained with THERMOCALC 3.2.1 software using the average PT approach (Powell & Holland 1994). The assemblages used and statistics are listed on the left of the PT diagram. Grt394 and Grt386 are respectively the core and rim composition of the garnet. Note that the thermobarometric results do not vary significantly whether core or the rim composition are used. The independent set of reactions used for the calculation is listed to the right of the PT diagram.

Average PT estimates of F101-2

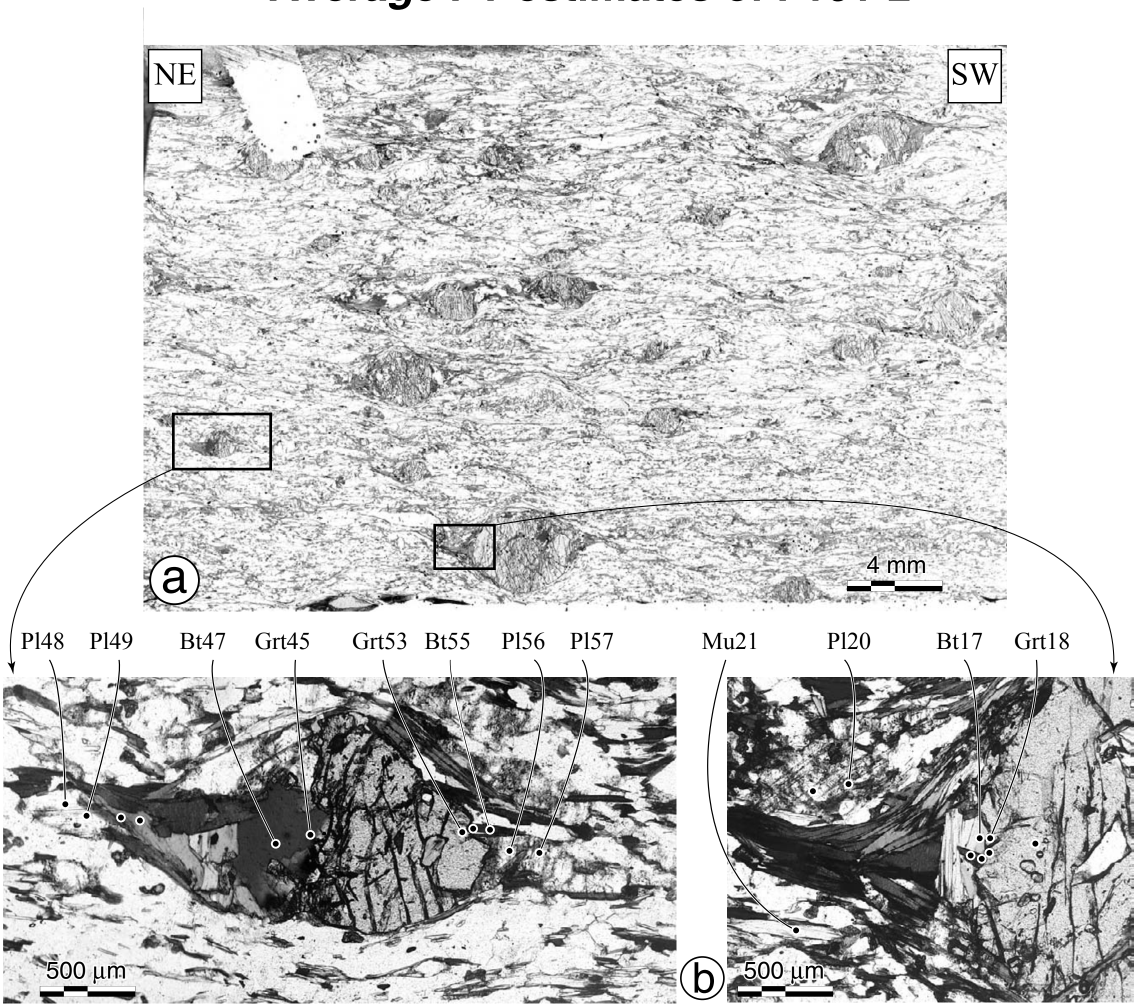

1: Grt18/Mu21/Pl20/Bt17
T = 753°C, sd = 54,
P = 11.8 kbar, sd = 1.9,
cor = 0.756, sigfit = 1.63

2: Grt45/Mu21/Pl48/Bt47
T = 703°C, sd = 32,
P = 11.0 kbar, sd = 1.1,
cor = 0.795, sigfit = 1.00

3: Grt45/Mu21/Pl49/Bt47
T = 689°C, sd = 40,
P = 10.2 kbar, sd = 1.4,
cor = 0.793, sigfit = 1.28

4: Grt53/Mu21/Pl56/Bt55
T = 711°C, sd = 41,
P = 10.9 kbar, sd = 1.5,
cor = 0.786, sigfit = 1.30

5: Grt53/Mu21/Pl57/Bt55
T = 699°C, sd = 48,
P = 10.3 kbar, sd = 1.7,
cor = 0.783, sigfit = 1.54

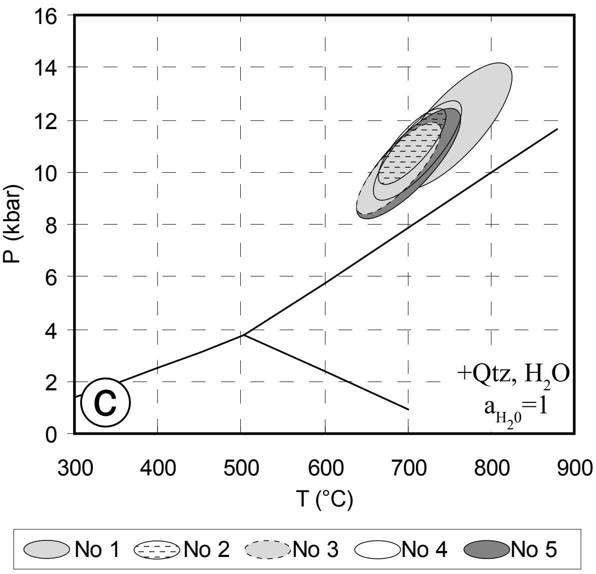

Independent set of 5 reactions used for the 5 calculated intercepts:

gr + 2pa + 3q = 3an + 2ab + $2H_2O$
mu + 2phl + 6q = py + 3cel
2east + 6q = py + mu + cel
3an + ann = gr + alm + mu
3an + phl = py + gr + mu

Fig. 7.6.
a) Picture of F101-2 thin section, parallel to the streaching lineation, with location of the analyzed areas. Note the biotite assymetric tails around the garnets, indicating a top-to-the-SW ductile shear sense.
b) Location of analyzed points in the biotite-rich assymetric tails.
c) Plot of the error-ellipses obtained with THERMOCALC 3.2.1 software using the average PT approach (Powell & Holland 1994). The assemblages used and statistics are listed on the left of the PT diagram. The independent set of reactions is listed to the right.

Chapter 8

Discussion

The geochronological data define two coherent age-groups consistent with structural observations. These results are discussed in the light of their structural position. Indications about the geodynamic setting of intrusion of the orthogneisses obtained by the geochemical study will also be integrated to their geological contexts. Then, we compare our results with published data from the Bulgarian part of the Rhodope Massif and from the neighbouring areas of the Aegean region.

Xanthi section

In the North Xanthi section (Fig. 8.1.b), the leucocratic gneiss below the Pangeon marbles is Permo-Carboniferous (RH11). In the UHP "melange" zone orthogneisses are also Permian (RH96 and F34). Above the "melange" zone, the augen-gneiss sliver is dated at 275.8 ± 3.9 Ma (F127). This gneissic body is overlain by a double horizon of marble. Liati (1986) and Barr *et al.* (1999) reported the presence of ultramafic rocks locally associated with this horizon, which in turn is overlain by highly sheared epidote-amphibolites. Above this shear zone, four Bt-gneisses (± Hbl) samples belong to the Late-Jurassic group (F220, F181, F180-2 and RH330). Despite the large amount of Tertiary intrusions and the strong migmatitization, the latter group represents a homogeneous and coherent body overthrusting the Pangeon Unit.

Drama section

In the Northern Drama section (Fig. 8.1.a), the gneisses above the Pangeon marbles, and below the Grt-Ky schist horizon, are Permian (samples RH78 and RH79, 282.7 ± 3.0 and 286.4 ± 4.0 Ma respectively). Therefore, although the contact marble-gneisses may be a thrust, in our view, it does not represent a terrane boundary, as the orthogneisses below and above the marbles, within the Pangeon Unit, witness the same crustal-growth event.

Above the Permian orthogneisses, a thin slice of Grt-Ky-Rt micaschists is associated with Grt-Cpx and Grt-Bt migmatites, minor marbles, amphibolites and ortho-migmatites. The garnets in the micaschist F101 show numerous crystallographically oriented needles of rutile and quartz (Fig. 8.1.a, see also chapter 6). These needles are interpreted as exsolutions from a Si-Ti-rich precursor of the garnet, pointing to a possible HP or UHP metamorphic history of the micaschist before reequilibration at around 10-12 Kbar and 700-750°C. In Xanthi area, Mposkos & Kostopoulos (2001) reported analogous features in similar lithologies, which revealed metamorphic micro-diamonds. The Grt-Cpx-Pl paragenesis (without Opx and primary Hbl) in the associated mafic migmatites points as well to a HP granulite-facies metamorphism (though not unequivocally, see Pattison 2003). Further upward in the pile, on the northern side of the Nestos River, a large amount of amphibolites (associated with marbles) is overlain by Bt-gneisses (F216) dated 158.0 ± 1.7 Ma by SHRIMP.

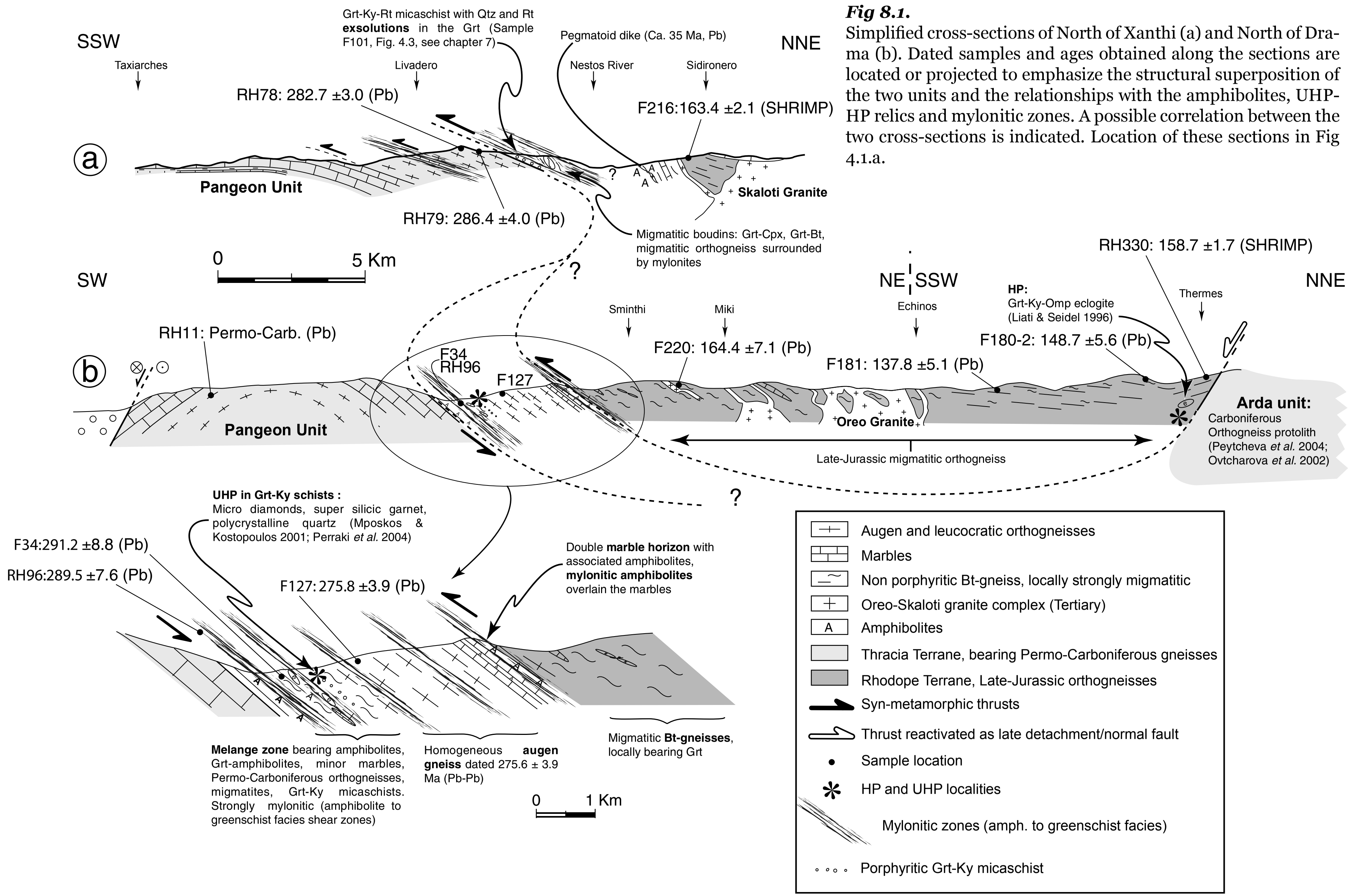

Fig 8.1.
Simplified cross-sections of North of Xanthi (a) and North of Drama (b). Dated samples and ages obtained along the sections are located or projected to emphasize the structural superposition of the two units and the relationships with the amphibolites, UHP-HP relics and mylonitic zones. A possible correlation between the two cross-sections is indicated. Location of these sections in Fig 4.1.a.

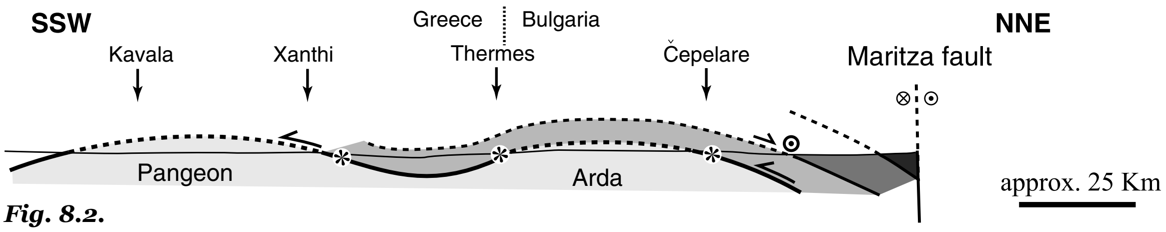

Fig. 8.2.
NNE-SSW idealized cross-section of the Central Rhodope. Note the flat-lying nature of the proposed suture separating the two terranes and its probable rooting below the Asenica Unit close to the contact with the Maritza fault. Tertiary intrusives, brittle faulting and sedimentary basins were removed to simplify the scheme.

Correlation of the two cross-sections

The distribution of protolith-ages between the two cross-sections is analogous (Paranesti area, Fig. 5.9): two Bt-gneisses located in the upper unit (F190 and RH126) belong to the Jurassic-Cretaceous group, whereas further south the augen-gneiss RH60 is Permian. Furthermore, an important amount of amphibolites and Grt-amphibolites has been recognized between the sampling sites of RH126 and RH60, on the road between Perivlepto village and the Nestos River (West of Paranesti, Fig. 4.4.c). All studied sections show important similarities. A Late-Jurassic Bt-gneiss body occupies systematically the higher structural position, whereas the underlying Pangeon Unit exposes only Permo-Carboniferous gneisses. Therefore, we correlate the sections of Xanthi and Drama along strike as shown in Fig. 8.1 and 5.9.

At large scale, mylonitic zones, UHP /eclogites relicts, and most of the mafic material (oceanic affinities) separate these units: therefore we consider them as two distinct igneous terranes, characterized by different timing of crustal growth. Aware of the risk of over-simplification, these terranes will be named as follows: Thracia terrane, bearing Permo-Carboniferous orthogneisses, and Rhodope terrane, consisting of Late-Jurassic orthogneisses. The present-day configuration can be explained by their collision after a subduction phase that gave rise to the UHP and HP metamorphism (Fig. 8.3). In such an interpretation, the melange zone bearing HP-UHP relicts and amphibolites represents a suture zone. This suture will be named the Nestos suture.

The Permian augen-gneiss sliver above the melange zone in the Xanthi section (sample F127) can be explained by overthrusting of parts of the lower block above the UHP-slice and incorporation of footwall material into the “melange” zone. The occurrence of an amphibolitic mylonite zone, associated with marbles, between the Permian orthogneiss-slice and the Bt-gneiss unit supports this hypothesis (Fig. 8.1 and Fig. 4.7.b and c). The amphibolites may have had a previous HP/UHP history erased by the retrograde amphibolite-facies overprint (Liati 1986; Liu *et al.* 2003).

Protolith emplacement tectonic setting

Geochemical analyses alone are not sufficient to decipher the geodynamic setting of the studied rocks. Therefore, we will discuss the geochemical results in the light of the geological and geodynamic context.

Permian granitoids:

During Late Carboniferous to Early Permian magmatism is active along all the Southern European margin, from Northern Italy to the Moesian platform (e. g. Schermaier *et al.* 1997, Finger & Steyrer 1990; Okay *et al.* 2001; Carrigan *et al.* 2003; Cortesogno *et al.* 2004). Interpretations diverge between post-orogenic collapse to subduction-related. Granitoids of the same age in the Arda dome are interpreted to be related to a volcanic-arc or late- to post-collision magmatism (Georgieva *et al.* 2003; Peytcheva *et al.*

2004).

The geodynamic setting of the Rhodope during Permian and Carboniferous is obscured by the Alpine orogeny, and the precise context of Permo-Carboniferous magmatism remains beyond the purpose of this study. Our data argue in favour of a volcanic-arc setting, possibly above the northward subduction of Paleo-Tethys below the Eurasian continental margin, as already documented in the Pelagonian basement (Vavassis *et al.* 2000; Reischmann *et al.* 2001; Anders *et al.* 2002; Stampfli & Borel 2002).

Jurassic granitoids:

Collision between the Rhodope and the Thracia terranes occurred in Cretaceous-Early Cenozoic time (Burg *et al.* 1996); the Late-Jurassic granitoids are therefore pre-collisional. This rules out the possibility of a post- and most probably syn-collisional intrusion. A back-arc basin setting is possible (influence of the subducted slab), but the continental affinities shown by the inherited component of the zircons make this possibility difficult. Therefore, we interpret the Late-Jurassic granitoids as the products of a subduction-related magmatic arc.

The Late-Jurassic igneous activity can be related to the subduction of a marginal ocean (Vardar, Meliata type?), located to the north of the Tethys Ocean. A contemporaneous Jurassic magmatic activity is recorded eastward, in the Pontides-Caucasus magmatic arc (Robertson & Dixon 1984; Dercourt *et al.* 1986; Kazmin *et al.* 1986; Sengör *et al.* 1993; Ricou *et al.* 1998). This northward subduction system at the southern margin of the Eurasian plate might be similar to the setting of the Rhodope Massif.

A remaining question concerns the crust on which the Jurassic magmatic arc was built. The SHRIMP dating of inherited cores hints at building on continental crust. Many of the preserved zircon cores have Permo-Carboniferous igneous ages (Fig. 5.6 and appendix 4). This might be the age of the last major growth of the continental crust on which the Jurassic arc formed. This crust may represent the equivalent of the Thracia terrane, rifted by the opening of a marginal ocean. This (Triassic?) rifting of the Permo-Carboniferous continental crust gave rise to a passive margin to the south, with deposition of the limestones that will become the Pangeon marbles on the Thracia terrane. The northern margin of this ocean evolved to a subduction zone in Jurassic time (building of the Rhodopian magmatic arc).

Correlation with the Bulgarian Central Rhodope

The intrusion-ages found in this study can be correlated with ages in the Bulgarian part of the Central Rhodope. Orthogneisses of the Arda dome yielded protolith ID-TIMS zircon ages of 310.7 ± 4.6 Ma and 300.0 ± 11 Ma (Ovtcharova et al. 2002; Peytcheva et al. 2004; Fig. 5.9). Although the Pb-Pb ages determined in the present study are slightly younger (ca. 275-290 Ma), we ascribe them to the same magmatic phase. Ivanov (1981) reports Pangeon marbles from a borehole in the Arda unit. The correlation of Arda and Pangeon units, as proposed in Fig. 8.1 and 4.1, is in agreement with the cross-section of Ivanov (1981). These two units appear as being part of the same terrane: the Thracia terrane, corresponding to the Drama plus Arda units of Ricou et al. (1998).

On the other hand, orthogneisses in the hanging wall of the Arda Unit are Late Jurassic (Ovtcharova *et al.* 2004). These ages are similar to our Pb-Pb and SHRIMP ages within the Rhodope terrane. Moreover, between the Arda Unit and its hanging wall, ultramafic material and eclogites are exposed (Kolcheva *et al.* 1986), and the mafic material has oceanic affinities (Kolcheva *et al.* 1986; Kolceva & Eskenazy 1988). Therefore, we propose that the unit bearing Late-Jurassic orthogneisses in Bulgaria belongs as well to the Rhodope terrane, and corresponds approximately to the Mesta unit plus Liaskovo formation of Ricou *et al.* (1998).

The Upper Arda Unit 2 of Burg *et al.* (1990), overlying the Arda dome on its northern slope, can be included into the Rhodope terrane, considering the occurrence of UHP and HP relicts and the deformational pattern in the Čepelare formation (Fig.

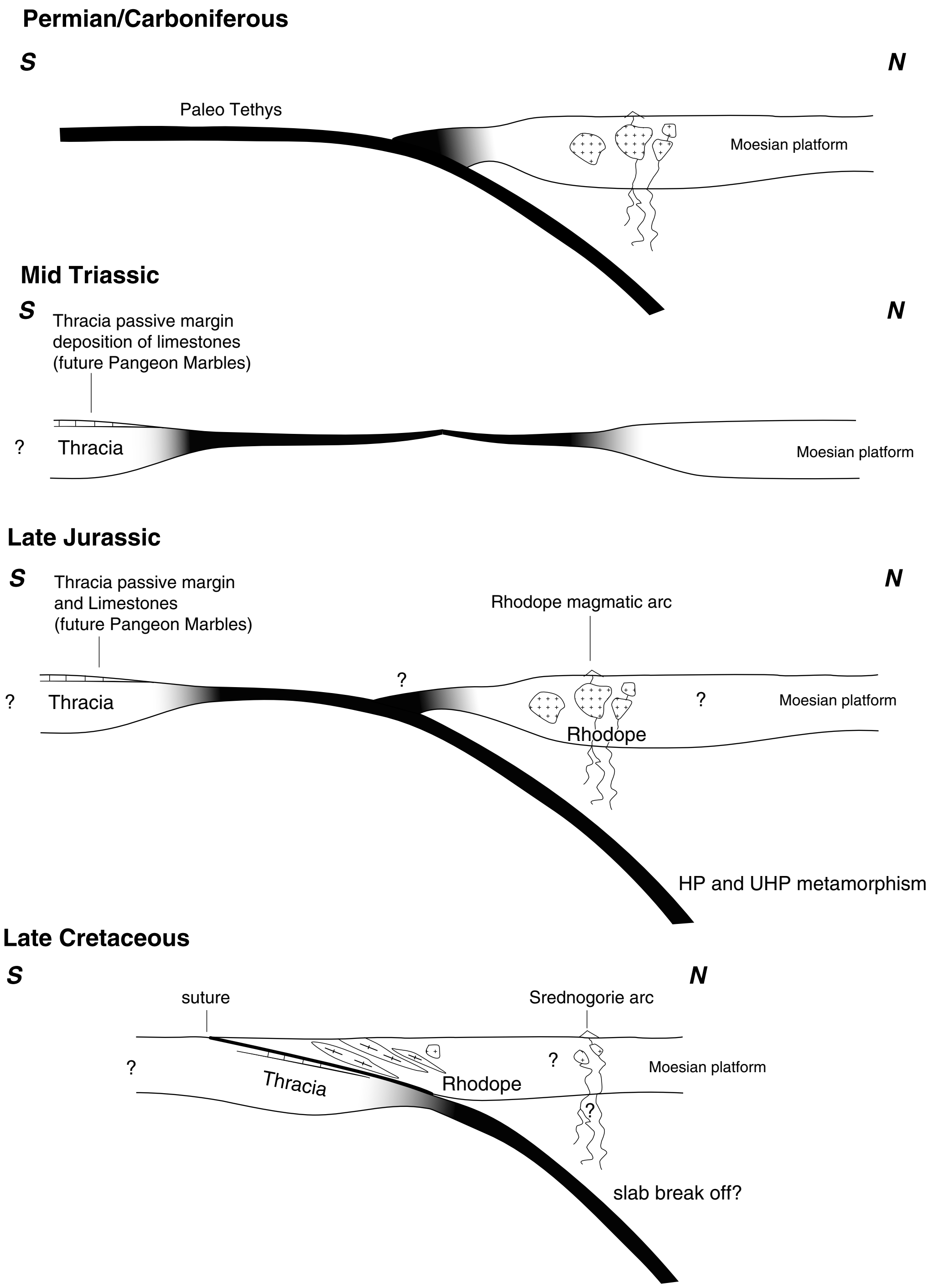

Fig. 8.3.
Interpretative model of the evolution of the Rhodope Massif (orientation of the section is only indicative):

Permo-Carboniferous: the Paleo Tethys subducts below the southern European margin giving rise to an important phase of continental growth by arc magmatism.

In **Late-Triassic Early Jurassic time**, an ocean separates the two terranes after a rifting phase (Early Triassic?).

In **Late Jurassic**, the Nestos Ocean separating the Thracia and Rhodope terranes subducts below the Rhodope terrane, giving rise to the calc-alkaline magmatic arc and the UHP/HP metamorphism.

During **Late Cretaceous** the two terranes collide (Burg *et al.* 1996) generating the overall configuration evidenced by this study as illustrated in Fig. 8.2. Despite the gap of at least 50 Ma between the igneous activity of the two arcs, this geometry implies the possibility that the Late-Cretaceous Srednogorie arc was generated above the same subduction zone.

1b, Kolceva *et al.* 1986; Burg *et al.* 1990; Gerdjikov *et al.* 2003; Kostopoulos *et al.* 2003;). Burg *et al.* (1990) already interpreted the Čepelare formation as a crustal-scale thrust zone. However, geochronological information on the orthogneiss protoliths above the Čepelare formation is too scarce to allow final conclusions on this issue.

Implications for the mode of occurence and age of the UHP relicts

The Rhodope terrane overthrusted the Thracia terrane along a flat-lying "melange" zone. This zone, bearing UHP and eclogite relicts, represents a suture. One striking feature is that, until now, UHP relicts have been only identified within this suture zone, suggesting that the terranes involved in the collision were not so deeply subducted, and that the UHP relicts are only preserved and exhumed within the suture zone. This characteristic reminds other collisional belts such as the Kokchetav massif (Kaneko *et al.* 2000) or the French Massif Central (Matte 1991; Lardeaux *et al.* 2001). On the other hand, this setting is in contrast to the Norwegian Caledonides where, instead, the continental crust of the Western Gneiss Region has been deeply subducted (e.g. Andersen *et al.* 1991).

Based on this simple geometric relationship, we propose that a single subduction event explains the occurrence of UHP and eclogite relicts in the Central Rhodope, despite the large time window interpreted as representing the UHP and/or HP stage. In the Central Rhodope, ages interpreted as representing the HP or UHP event range from 42 up to ca. 150 Ma. The zircon age of 42 ± 0.9 Ma from an eclogite (Liati & Gebauer 1999) is surprisingly close to the age of the HT overprint and migmatitization as revealed by U-Pb monazite dating in Bulgaria (35-37 Ma and 47-52 Ma; Peytcheva *et al.* 2004; Ovtcharova *et al.* 2004). Instead, the U-Pb SHRIMP age of 148.8 ± 2.2 Ma in zircon metamorphic rims from Grt-Ky metasediments (Liati 2005), as well as the 140 ± 4 Ma Sm-Nd age from the same lithologies (Grt/whole-rock age interpreted as cooling age postdating the UHP, Reischmann & Kostopoulos 2002), suggest a Late Jurassic age for the HP/UHP metamorphism. Therefore, the Late-Jurassic magmatic arc defined in this study is likely to have been built above the same subduction zone that gave rise to the UHP-HP metamorphism.

Further west in the Drama section of this study, a zircon rim in an amphibolized eclogite within the melange zone yielded an age of 51.0 ± 1.0 Ma (Liati 2005). The REE patterns of the dated zircon domains (Jurassic and Early Eocene) show no Eu anomly and flat HREE profiles. These ages are then interpreted as closely approximating HP and/or UHP stages. This series of ages (42, 51, 149 and 73 Ma, the latter belongs to the Kimi complex, out of the studied area) is interpreted as a testimony of repeated subduction and collision of several terranes (Liati 2005). This interpretation contrasts with our results, which instead clearly show a unique "melange" zone bearing the UHP relicts. Therefore, we prefer to interpret the large scatter of UHP-HP stage ages as reflecting a complex exhumation history of the UHP rocks related to a single subduction system rather than the collision of more than two terranes during the alpine orogeny. If this is true, the Eocene ages must be regarded as representing an overprinting (still at HP, possibly at the base of an over-thickennned crust?) but clearly postdating the UHP stage. The latter cannot have lasted for ca. 100 Ma as the exhumation from mantle depth to the base of the crust should be extremely fast if we compare with other similar settings in diffferent orogenic belt (e.g. Hermann *et al.* 2001; Lardeaux *et al.* 2001).

The location of the suture root remains also matter of further work. However, considering the overall vergence of the structures towards the SW and SSW, the Vardar zone is unlikely the root zone. Instead, the rooting of the suture can be expected towards the North, below the Asenica unit in Bulgaria, at the contact with the Maritza fault (Burg *et al.* 1996; Ricou *et al.* 1998). The northern limit of the Rhodope terrane remains unclear. Additional studies, especially on Asenica and Parvenec units, are needed to reveal their affinities. Protolith ages are too scarce to allow unravelling the detailed relationships and geodynamic evolution of the Thracia terrane versus the Moesian platform.

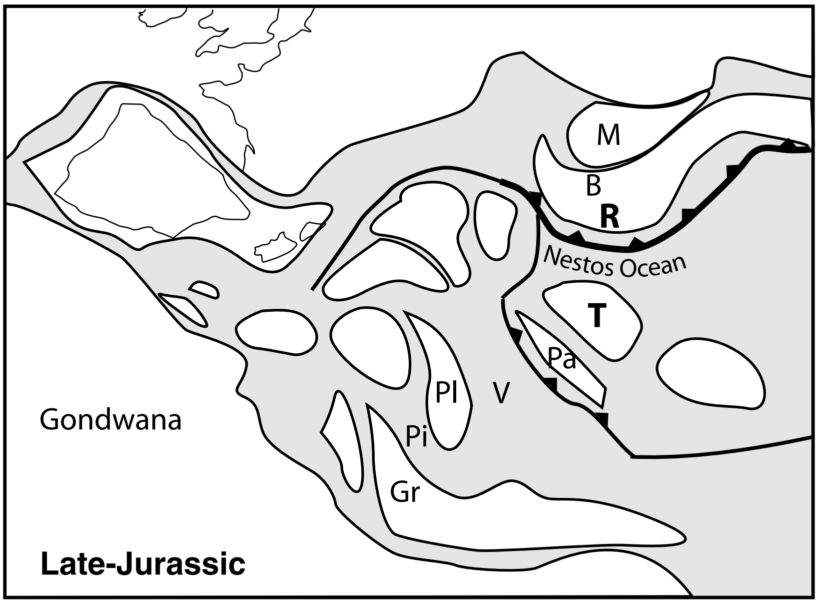

Fig. 8.4.
Late-Jurassic paleogeographic position of the Rhodope and Tracia terranes in the Tehys realm, modified after Ricou (1994).

Paleogeographic implications

The present work shows the existence of a north-directed subduction zone, active at the southern European margin in Late Jurassic time, located north of the Vardar zone. This confirms the evolutionary model proposed by Ricou *et al.* (1998; see also Ricou 1994). This model has also been implemented in the more recent one of van Hinsbergen *et al.* (2005).

The model of Robertson & Dixon (1984) is also in favour of a North-directed subduction system at the southern European margin although this subduction is located at the Northern margin of the Vardar Ocean.

Stampfli & Borel (2001, see also Bonev & Stampfli 2003) are in favour of a Jurassic South-Eastward subduction of the Rhodope below the Izanca Ocean (future eastern Vardar Ocean) instead of a northward subduction north of the Vardar Ocean.

Fig. 8.3 and 8.4 illustrates an attempt to synthesize the evolution of the massif since the Carboniferous and to integrate it in the more general Tethys realm.

The proposed geometry in Fig. 8.3 might suggest that the Late Cretaceous Srednogorie magmatic arc is related to the slab corresponding to the Nestos suture, and not, as previously inferred, to the Vardar subduction further south (e.g. Boccaletti *et al.* 1974, Hsü *et al.* 1977, Ciobanu *et al.* 2002). However, this proposition must be confirmed by further studies notably because the effect of the Maritza fault is not yet quantified, and the gap of more than 50 Ma between the igneous activity of Rhodope and Srednogorie arcs raises major questions.

Open questions

An aspect that remains unsolved is the lateral continuation of the terranes and the suture identified in this study.

Towards the West, the importance of the Pirin granitic intrusion (Fig. 2.2) might render the identification of the terrane harder. Furthermore, the overlying Kraiste (Fig. 1.2) seems to have different affinities (Graf 2001 and Kounov 2002).

Towards the East, the structural framework is still obscure. All we can say is that the lower unit (Byala Reka, Fig. 2.2) seems to be a prolongation of the Thracia terrane, since it also has a Permo-Carboniferous basement (Peytcheva *et al.* 1995 and this study, samples RH311 and RH323). On the other hand, despite numeros studies and the presence of

UHP relicts in Kimi and Sidiro areas (Mposkos & Kostopoulos 2001), the hanging wall unit characterisation and structural frame are still unclear, most of these studies being focused only on the petrology of single outcrops. The question whether the Kimi Complex (the hanging wall unit of the Eastern Rhodope) belongs to the Rhodope terrane is opened. These two units seem significantly different. In general the Kimi complex shows a larger amount of mafic material than in the Rhodope terrane as defined here. However, despite these doubts, as the UHP metamorphism in Eastern and Central Rhodope might be related to the same subduction event, the suture would extend for more than 200 Km laterally making of the melange zone not only a punctual occurence but a large UHP belt.

In the eastern Rhodope, at higher stuctural level, the low grade ophiolitic series of Evros formed in a arc environment during the Jurassic (Magganas 2002). The comparison with the Rhodope terrane is difficult, since the provenance of the Evros ophiolite is uncertain. Nonetheless, the similarity in age and environment with the Rhodope terrane suggests that the Evros ophiolite could represent a non subducted part of the Rhodope terrane.

The allochtonous Mesozoic schist series of arc affinities in southeastern Bulgaria (Bonev & Stampfli 2003) is also candidate for representing some supracrustal expression of the Rhodope terrane. However, these autors prefer to interpret them as representing an island arc-accretionary complex related to the southward subduction of the Meliata–Maliac Ocean under the supra-subduction back-arc Vardar ocean/island arc system.

UHP metamorphism has been suggested from graphitized diamond between the Serbo-Macedonian Massif and the Vardar zone (Kostopoulos *et al.* 2001). This metamorphic event is most probably Late Jurassic/Early Cretaceous as suggested by the Sm-Nd age of 145 ± 22 Ma of Reischmann & Kostopoulos (2001). This implies a similar age of subduction for these rocks and the ones of the "melange" zone in the Rhodope Massif. Furthermore the similarity in age of the subduction-related magmatic activity in the Vardar Zone (Anders *et al.* 2005) and the Rhodope terrane is also striking. Therefore three scenarios are possible:

1) two subduction zones were active one in the Vardar and one in the Rhodope, producing UHP metamorphism at the same time.

2) only one was active within the Rhodope (corresponding to the Nestos suture) and consequently, the eastern Vardar zone represent a klippe of Rhodopian affinity.

3) The third possibility is a combination of the two last ones: two subduction zones were active at the same time, one in the Vardar (Paikon arc) and one in the Rhodope. But part of the Rhodope Massif have been overthrusted until the eastern Vardar Zone.

However, the question whether the Vardar zone represents, at least for its eastern part, a klippe of the Rhodope terrane (Ricou *et al.* 1998), or rather a "in situ" magmatism (Brown & Robertson 2004), is still open. Between these two domains, the presence of the Vertiskos terrane, of neither Rhodopian (s.l.) neither Vardar affinities, complicates the scheme (Himmerkus *et al.* 2003).

Conclusion

This study results in a clearer view on the organization between the gneissic blocks and the UHP-HP occurrences in the Central Rhodope. The UHP relicts are part of a coherent horizon which delineates the suture zone separating two terranes.

Two magmatic units are identified on the basis of their distinct intrusion ages. Pb-Pb single zircon and zircon U-Pb SHRIMP ages are organized in two age groups: one ranges between 270 and 291 Ma, the other between 134 and 163 Ma. These two crustal units with different magmato-tectonic evolutions are interpreted as distinct terranes because of their lithological differences and the nature of their contact characterized by mylonitic zones, UHP-relicts and mafic material (defined here as the melange zone). The Thracia terrane records a Permo-Carboniferous igneous activity, probably related to the subduction of the Paleo-Tethys underneath the southern European margin. The Rhodope terrane, a Late-Jurassic magmatic complex, witnesses the subduction of an oceanic basin of the Neo-Tethys system below the European margin.

Between these two terranes the UHP relicts and eclogites, associated with amphibolites of oceanic affinities and ultramafic rocks, delineate a suture within the Central Rhodope. The trace of this suture can be followed for more than 70 km along strike in the Greek part of the Rhodope Massif, and for almost 100 km to the North, along the main transport direction. The UHP relicts are recognised only within the melange zone. Although the precise mechanisms of exhumation are still uncertain, we propose that the UHP relicts are only preserved and exhumed within the melange zone. Furthermore, the singularity of the suture suggests that a single Jurassic subduction explains the UHP and eclogitic metamorphisms in the Central Rhodope despite the large age range previously attributed the UHP and/or HP stage. This subduction phase was followed by the Cretaceous collision between the two terranes defined in this study.

Appendix

Appendix 1a:
Orthogneiss sample pictures (Permo-Carboniferous group)

RH31

RH60

RH78

RH79

RH87

RH89

RH96

RH123

RH132

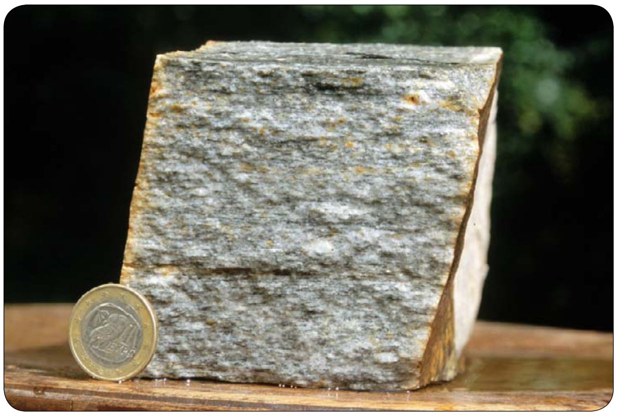

RH336

F34

F127

Appendix 1b:
Orthogneiss sample pictures (Late-Jurassic group)

RH126

RH330

F180-2

F181

F190

F216

F220

F225

Appendix 2: Zircon cathodo-luminescence imaging

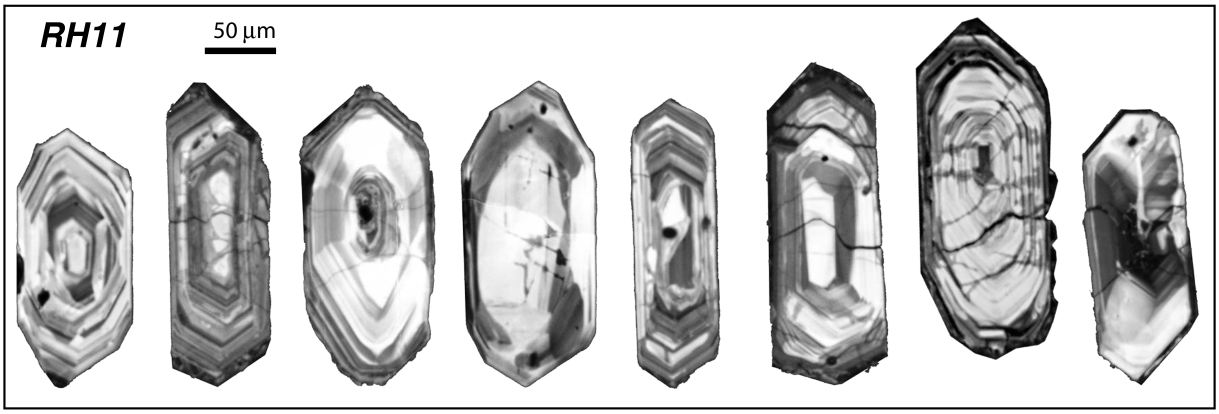

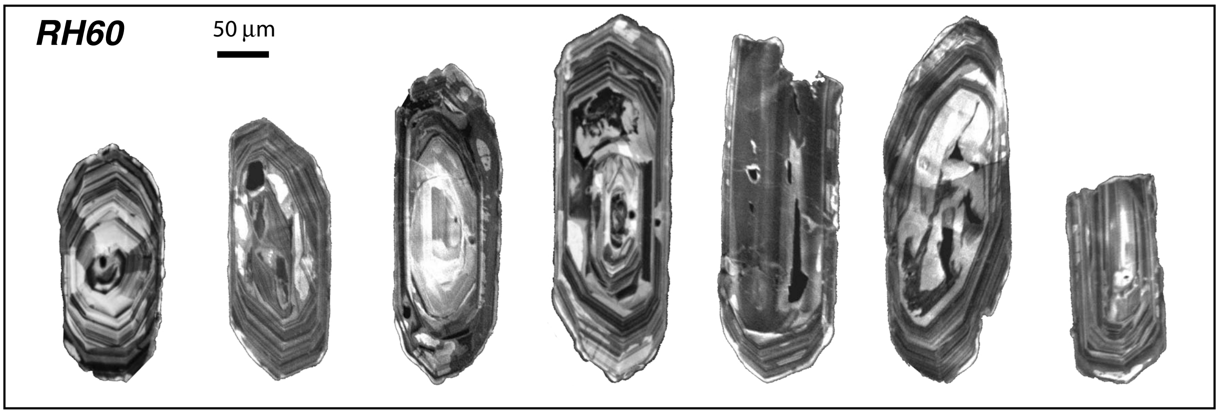

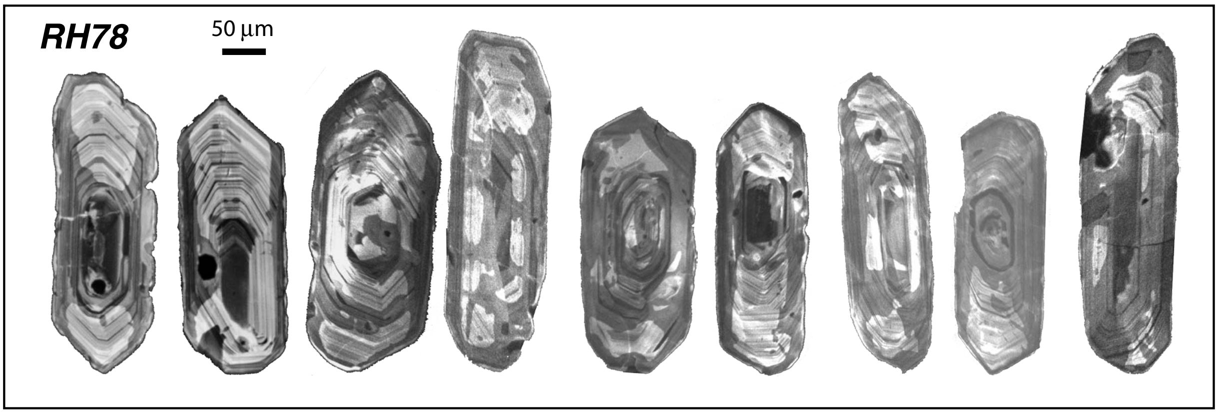

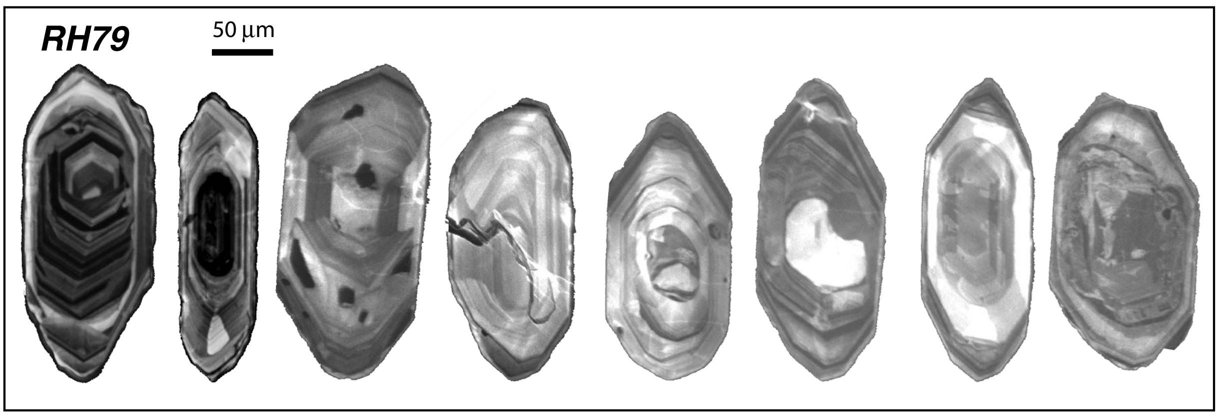

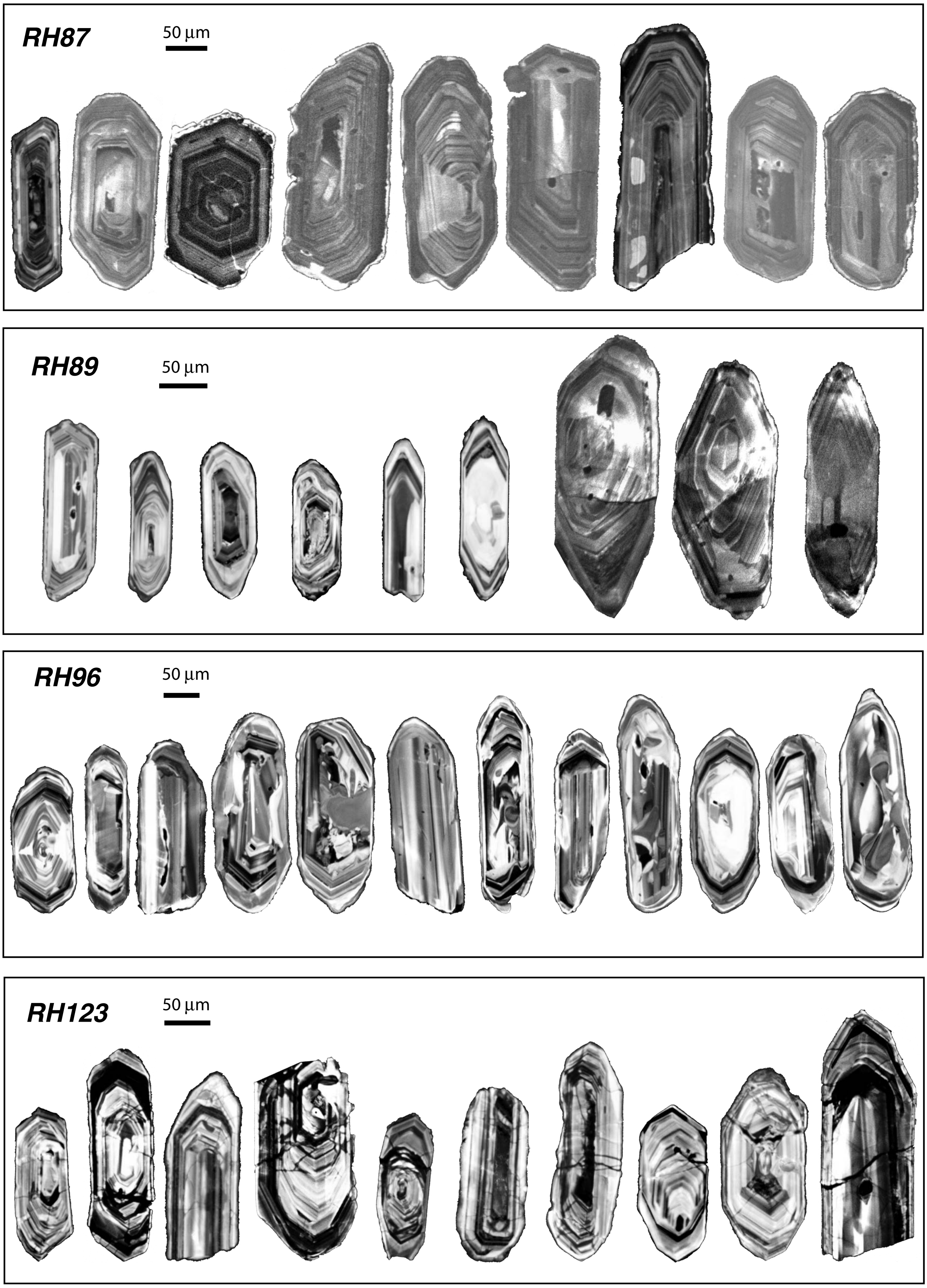
RH87
50 µm
RH89
50 µm
RH96
50 µm
RH123
50 µm

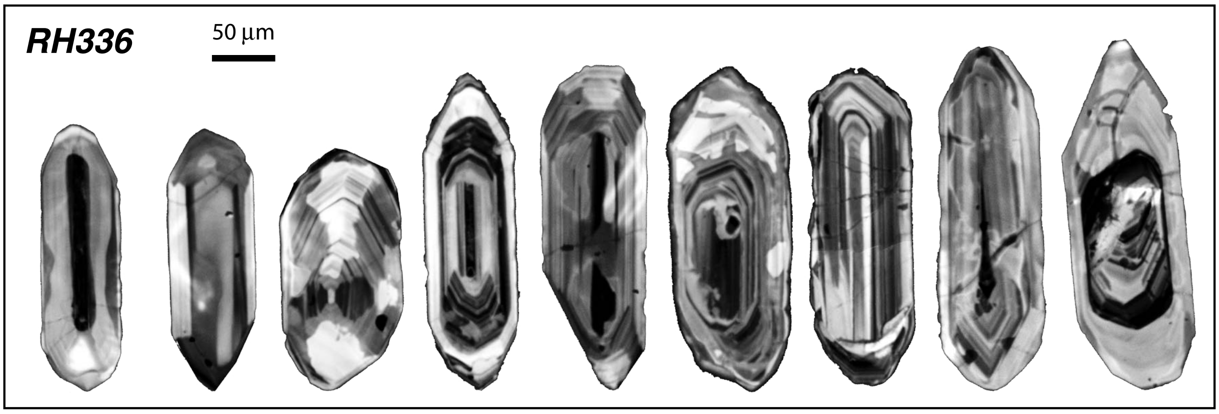
RH336
50 µm

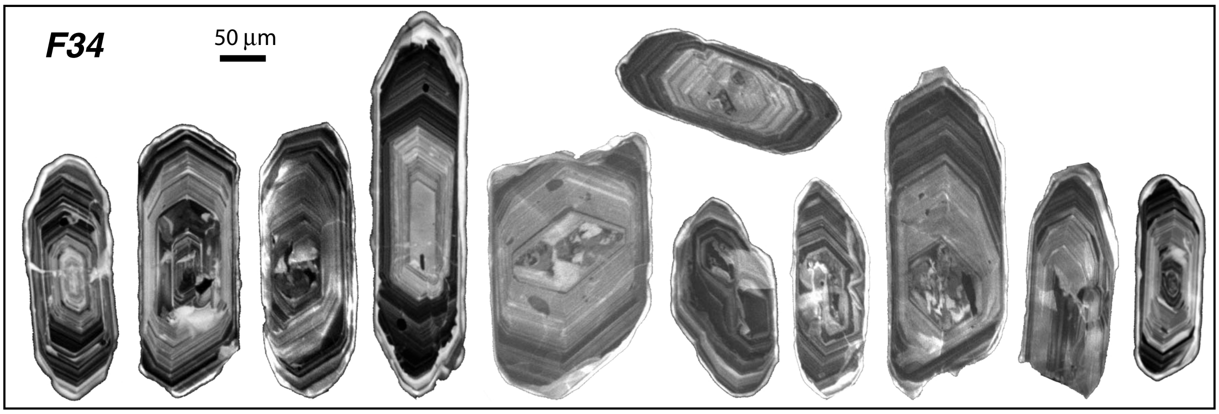
F34
50 µm

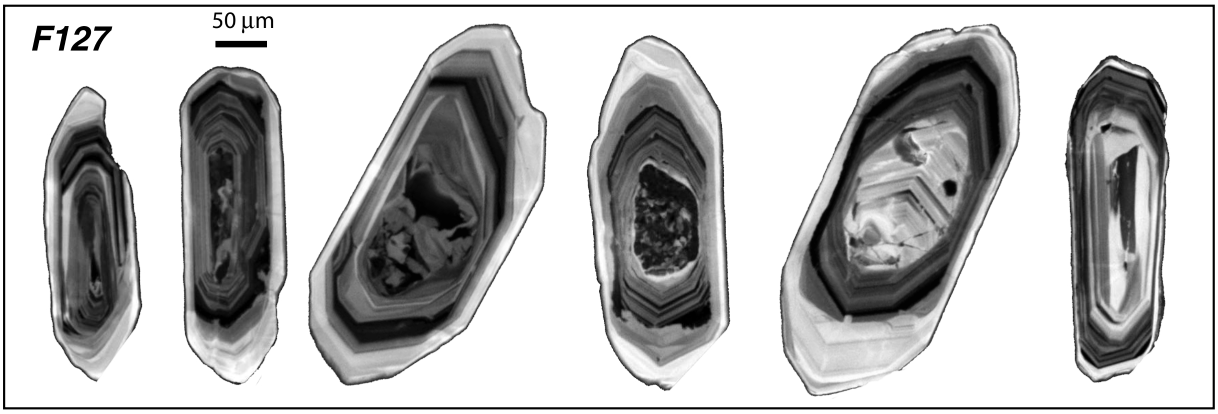
F127
50 µm


RH323
50 µm

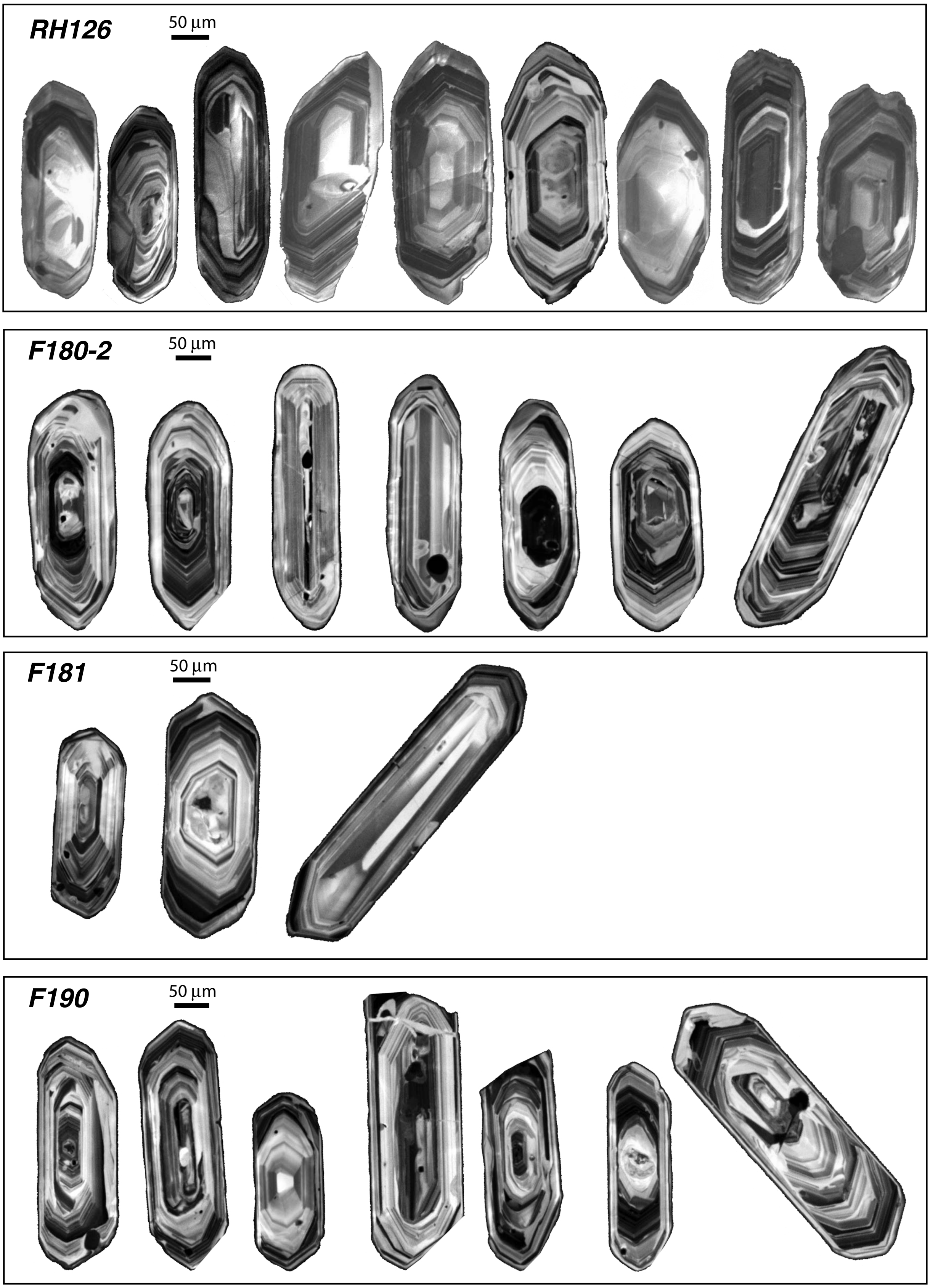
RH126
50 µm
F180-2
50 µm
F181
50 µm
F190
50 µm

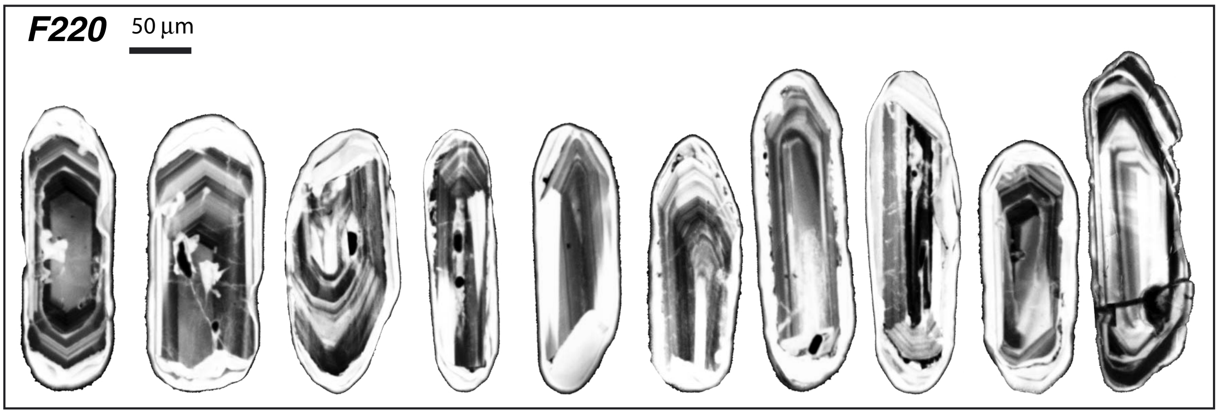
F220
50 µm

Appendix 3:
Pb-Pb evaporation analytical results

Appendix 3: *Summary of the measured Pb-Pb zircon isotopic ratios and associated 2 σ errors. The calculated apparent ages for each measurement, the weighed average after rejection for each sample are given (when meaningful). All the measured zircons were euhedral. All analyses are single grain measurements except F180-2 and F220, number of zircons in brackets.*

Grain and samples	Habitus	$^{207}Pb/^{206}Pb$	± 2σ (%)	$^{206}Pb/^{204}Pb$	± 2σ (%)	App. age (Ma)	±2σ (Ma)	reasons for rejection
RH11								
1		0.05339	0.04	17489	4.62	309.6	2.7	
3		0.05418	0.19	5805	6.33	270.2	12.0	
4		0.05468	0.16	5006	7.05	273.8	13.7	
6		0.05504	0.15	3976	3.61	256.5	9.7	
9	200*100 µm, yellow, turbid	0.05395	0.30	6513	7.96	272.0	15.7	
10	200*80 µm, yellow, clear	0.05420	0.26	4919	6.84	250.9	15.9	
11	200*100 µm, white, turbid, fragment	0.05381	0.26	11453	18.92	308.5	16.4	
12	200*100 µm, light yellow, clear	0.05352	0.24	7311	8.72	264.0	14.1	
			RH11	**mean age:**		**309.6 ± 2.6 or 263.9 ± 9.2**		
				intercept age:		**n.a.**		see text
RH60								
1	300 µm, uncolored, clear	0.05417	0.09	5780	2.94	269.2	5.6	
2	300 µm, uncolored, clear	0.05514	0.04	4338	1.36	275.0	3.1	
3	*350 µm, uncolored, clear*	*0.06451*	*0.13*	*1135*	*1.61*	~~*266.8*~~	~~*12.6*~~	d
4	300 µm, uncolored, clear	0.05343	0.11	9139	4.52	277.8	6.0	
5	350 µm, white, turbid	0.05872	0.12	2087	0.84	272.5	5.3	
7	350 µm, uncolored, clear	0.05472	0.11	5036	2.69	277.1	5.9	
8	*400 µm, light yellow, turbid*	*0.05619*	*0.44*	*3351*	*5.61*	~~*276.4*~~	~~*21.8*~~	a
9	300*100 µm, uncolored, clear	0.05340	0.14	8866	6.50	274.3	8.3	
10	250*90 µm, light yellow, clear	0.05278	0.15	18282	12.15	284.7	8.4	
11	350*150 µm, light yellow, clear	0.05390	0.16	7644	4.55	284.5	7.8	
			RH60	**mean age:**		**275.5**	**3.6**	
				intercept age:		**279.3**	**7.5**	
RH78								
1	400 µm, uncolored, clear	0.05479	0.15	5120	2.82	282.1	7.2	
4	*400 µm, uncolored, clear*	*0.05496*	*0.30*	*4812*	*10.75*	~~*281.7*~~	~~*23.1*~~	a
5	400 µm, uncolored, clear	0.05629	0.13	3490	2.27	289.5	7.4	
7	400*120 µm, uncolored, clear	0.05400	0.15	6769	3.66	278.3	7.0	
8	300*100 µm, uncolored, clear	0.05290	0.26	14686	14.63	281.0	13.5	
10	*400*120 µm, uncolored, clear*	*0.06206*	*0.28*	*1498*	*2.25*	~~*297.5*~~	~~*16.2*~~	d
11	400*100 µm, uncolored, clear	0.05337	0.17	10037	4.40	281.6	6.9	
12	400*140 µm, uncolored, clear	0.05318	0.33	12174	11.62	284.3	14.7	
13	400*100 µm, uncolored, clear	0.05402	0.14	7026	4.12	282.6	7.1	
			RH78	**mean age:**		**282.7**	**3.0**	
				intercept age:		**276.4**	**5.6**	
RH79								
5	300 µm, clear, uncolored, clear	0.05317	0.14	13103	7.50	288.0	7.0	
6	300 µm, uncolored, clear, fragment	0.05522	0.19	4593	6.35	287.0	14.0	
7	300*100 µm, uncolored, clear	0.05246	0.15	35650	12.49	288.0	7.0	
8	280*100 µm, uncolored, clear	0.05245	0.13	27291	15.76	282.0	8.0	
			RH79	**mean age:**		**286.4**	**4.0**	
				intercept age:		**285.0**	**12.0**	
RH87								
1	*600 µm, light yellow, clear*	*0.06051*	*0.15*	*1811*	*1.11*	~~*303.9*~~	~~*7.5*~~	b
3	400 µm, uncolored, clear	0.05534	0.11	4444	3.74	287.4	8.0	
4	350 µm, uncolored, slightly turbid	0.06489	0.07	1115	0.62	274.2	6.4	
6	400 µm, uncolored, clear	0.05871	0.20	2136	1.82	278.6	10.2	
7	400*50 µm, uncolored, clear	0.06623	0.27	1010	1.78	272.6	18.2	
9	*300*80 µm, uncolored, slightly turbid*	*0.06308*	*0.34*	*1249*	*3.21*	~~*256.0*~~	~~*25.7*~~	a
10	300*100 µm, uncolored, clear	0.05563	0.21	3850	4.95	277.6	13.5	
			RH87	**mean age:**		**278.7**	**7.7**	
				intercept age:		**287.6**	**6.2**	

a: too large error

b: inherited component

c: lead loss

d: low $^{206}Pb/^{204}Pb$

Appendix 3 *(continued)*

Grain and samples	Habitus	$^{207}Pb/^{206}Pb$	± 2σ (%)	$^{206}Pb/^{204}Pb$	± 2σ (%)	App. age (Ma)	±2σ (Ma)	reasons for rejection
RH89								
2		*0.05421*	*0.18*	*5212*	*5.50*	~~*258.8*~~	~~*11.6*~~	c
3	300 µm, light brown, clear	0.05567	0.22	3896	3.85	281.3	11.8	
5	300 µm, pink, clear	0.05484	0.11	5024	3.11	282.0	6.8	
6	400 µm, pink, slightly turbid, fragment	0.05861	0.11	2158	1.42	277.5	7.0	
7	*300*120 µm, uncolored, clear*	*0.05573*	*0.29*	*3354*	*5.31*	~~*256.8*~~	~~*17.6*~~	c
8	300*100 µm, uncolored, clear	0.05372	0.18	8722	5.76	287.4	8.8	
10	300*100 µm, uncolored, clear	0.05290	0.21	13717	10.42	278.0	10.4	
11	300*150 µm, uncolored, clear	0.05382	0.14	8304	3.71	287.7	6.2	
			RH89	**mean age:**		**282.9**	**4.8**	
				intercept age:		**287.2**	**7.9**	
RH96								
1	400 µm, uncolored, clear	0.05304	0.13	14158	8.43	285.6	7.1	
2	400 µm, yellow, clear	0.05476	0.10	6028	3.18	299.9	5.9	
3	400 µm, yellow, clear	0.05388	0.19	7483	7.45	281.7	11.2	
4	400 µm, yellow, clear, fragment	0.05371	0.13	8967	6.37	288.8	7.8	
5	300 µm, light yellow, clear	0.05256	0.18	19640	11.51	277.2	8.5	
6	250*100 µm, light yellow, clear	0.05265	0.21	27137	12.82	290.4	8.3	
7	280*100 µm, yellow, clear	0.05323	0.43	13950	17.17	293.5	19.3	
			RH96	**mean age:**		**289.5**	**7.6**	
				intercept age:		**278.0**	**14.0**	
RH123								
2	300*100 µm, light pink, clear	0.06264	0.26	1333	2.52	269.5	18.5	
4	400 µm, light yellow, clear	0.05418	0.21	5642	8.03	269.3	15.0	
7	250*220 µm, pink, turbid	0.06127	0.30	1516	4.23	267.7	26.2	
8	280*120 µm, uncolored, clear	0.06422	0.25	1170	2.19	271.6	18.1	
9	*300*100 µm, white, turbid*	*0.07017*	*0.41*	*784*	*2.66*	~~*261.8*~~	~~*33.1*~~	
			RH123	**mean age:**		**269.7**	**9.0**	
				intercept age:		**266.0**	**14.0**	see text
RH323								
1	350*120 µm, uncolored, clear	0.05316	0.17	15718	10.18	295.2	8.5	
2	350*180 µm, unclored, clear	0.05291	0.10	24560	9.95	299.3	5.3	
3	350*200 µm, uncolored, clear, fragment	0.05286	0.13	15943	9.88	282.7	7.4	
4	400*140 µm, uncolored, clear	0.05358	0.14	9999	9.69	290.3	10.0	
5	350*100 µm, uncolored, clear	0.05313	0.14	11777	6.37	280.2	7.0	
6	250*200 µm, uncolored, clear, fragment	0.05324	0.26	10680	12.73	279.6	15.0	
7	250*100 µm, uncolored, clear	0.05497	0.36	4601	9.79	275.8	23.6	
8	250*80 µm, uncolored, clear	0.05272	0.36	15043	16.81	274.3	16.9	
9	300*100 µm, slightly brown, clear	0.05441	0.22	7020	8.16	298.7	13.2	
10	350*150 µm, brown, clear	0.05326	0.23	11152	13.12	283.1	14.1	
			RH323	**mean age:**		**289.7**	**6.5**	
				intercept age:		**294.0**	**16.0**	
RH311								
1	400*180 µm, yellowish, turbid	0.06505	0.15	1125	1.23	286.5	10.2	
2	*300*100 µm, uncolored, clear*	*0.05488*	*0.08*	*11022*	*4.30*	~~*352.2*~~	~~*4.4*~~	b
3	350*60 µm, uncolored, clear	0.05447	0.49	5258	11.65	271.1	27.8	
4	250*100 µm, uncolored, clear	0.05440	0.27	4614	7.08	251.0	17.2	
5	300*100 µm, uncolored, slightly turbid	0.05344	0.31	10163	15.72	285.4	18.9	
			RH311	**mean age:**		**278.0**	**26.0**	
				intercept age:		**265.0**	**64.0**	
F34								
1	400 µm, light yellow, clear	0.05318	0.10	15060	5.57	294.7	4.7	
2	300*100 µm, yellow, clear	0.05341	0.13	12449	5.85	295.6	6.1	
3	300*100 µm, light yellow, clear	0.05317	0.26	11774	13.68	282.0	14.8	
4	300*150 µm, yellow, clear	0.05302	0.13	13148	6.15	281.1	6.2	
5	300*100 µm, yellow, clear	0.05439	0.19	6979	11.07	298.0	15.9	
			F34	**mean age:**		**291.2**	**8.8**	
				intercept age:		**275.0**	**81.0**	

a: too large error

b: inherited component

c: lead loss

d: low $^{206}Pb/^{204}Pb$

Appendix 3 *(continued)*

Grain and samples	Habitus	$^{207}Pb/^{206}Pb$	± 2σ (%)	$^{206}Pb/^{204}Pb$	± 2σ (%)	App. age (Ma)	±2σ (Ma)	reasons for rejection
RH336								
1	400*180 µm, uncolored, clear	0.05490	0.24	5083	9.39	286.3	18.9	
2	*280*100 µm, uncolored, clear*	*0.05315*	*0.35*	*4026*	*11.37*	~~*171.7*~~	~~*30.0*~~	c
3	*300*100 µm, light yellow, clear*	*0.05294*	*0.23*	*9461*	*6.21*	~~*258.4*~~	~~*9.8*~~	c
4	300*100 µm, orange, clear	0.05303	0.11	13587	3.60	283.3	4.3	
5	*300*120 µm, orange, clear*	*0.05238*	*0.22*	*12892*	*11.67*	~~*251.9*~~	~~*11.9*~~	c
6	400*120 µm, light yellow, slightly turbid	0.05325	0.12	10327	3.32	277.9	5.0	
7	*300*120 µm, uncolored, clear*	*0.05291*	*0.18*	*9196*	*7.57*	~~*254.9*~~	~~*9.9*~~	c
8	300*150 µm, orange, clear	0.05409	0.18	7489	5.05	291.2	8.6	
9	250*150 µm, uncolored, clear	0.05754	0.34	2798	4.96	298.9	19.8	
			RH336	**mean age:**		**281.1**	**6.4**	
				intercept age:		**273.0**	**14.0**	
F127								
1	*300*80 µm, light yellow, clear*	*0.05325*	*0.25*	*9112*	*19.82*	~~*269.6*~~	~~*23.7*~~	a
2	340*100 µm, uncolored, clear	0.05400	0.29	5878	7.67	263.4	16.1	
3	300*60 µm, yellow, clear	0.05333	0.25	10391	7.53	282.1	10.9	
6		*0.06211*	*0.44*	*8768*	*14.36*	~~*678.0*~~	~~*20.0*~~	b
7	250*100 µm, uncolored, clear	0.05326	0.27	8827	12.84	267.8	17.2	
8	400*100 µm, uncolored, clear	0.05250	0.21	22188	23.55	278.6	14.0	
9	350*80 µm, uncolored, clear	0.05285	0.23	12937	9.75	272.8	10.6	
10	300*100 µm, uncolored, clear	0.05264	0.15	17459	6.43	276.4	6.0	
11	300*80 µm, uncolored, clear	0.05281	0.25	15167	15.37	278.6	13.5	
			F127	**mean age:**		**275.8**	**3.9**	
				intercept age:		**282.4**	**6.7**	
RH126								
1	350*120 µm, uncolored, clear	0.04980	0.18	14448	10.50	138.3	9.8	
2	300*120 µm, uncolored, clear	0.05313	0.19	3368	4.96	137.4	15.1	
4	400*150 µm, yellow, clear	0.04932	0.11	24722	10.59	135.8	5.9	
5	400*100 µm, uncolored, clear	0.04975	0.38	16215	20.32	141.2	19.6	
6	*300*100 µm, uncolored, clear*	*0.04983*	*0.70*	*15368*	*36.00*	~~*142.4*~~	~~*n.a.*~~	a
7	400*100 µm, light yellow, clear	0.04947	0.14	18062	11.73	132	8.3	
8	300*100 µm, light yellow, clear	0.05014	0.18	9924	8.90	132.6	11.1	
9	350*150 µm, uncolored, clear	0.05027	0.20	8427	5.60	126.2	9.5	
10	*300*100 µm, uncolored, clear*	*0.04954*	*0.23*	*12541*	*17.98*	~~*119.1*~~	~~*17.2*~~	c
			RH126	**mean age:**		**134.0**	**3.5**	
				intercept age:		**133.7**	**7.6**	
F190								
1	400*100 µm, uncolored, clear	0.05074	0.24	7302	9.15	135.8	15.0	
2	400*100 µm, uncolored, clear	0.05060	0.24	8006	8.30	137.4	13.5	
3	300*100 µm, uncolored, clear	0.05063	0.26	7090	10.30	127.8	17.1	
4	*300*100 µm, uncolored, clear*	*0.04981*	*0.20*	*10330*	*9.05*	~~*120.0*~~	~~*12.1*~~	c
5	340*130 µm, uncolored, clear	0.04939	0.16	21700	14.85	135.0	9.1	
7	*280*100 µm, uncolored, clear*	*0.05053*	*0.18*	*17540*	*11.00*	~~*180.7*~~	~~*9.1*~~	b
8	400*150 µm, uncolored, clear	0.04998	0.20	12483	6.02	139.5	8.1	
9	300*80 µm, uncolored, clear	0.05249	0.24	3928	2.34	136.7	9.7	
			F190	**mean age:**		**136.5**	**4.3**	
				intercept age:		**135.6**	**5.8**	
F181								
1	*350*80 µm, uncolored, clear*	*0.05130*	*0.36*	*4231*	*12.30*	~~*93.5*~~	~~*30.3*~~	c
2	*300*100 µm, light yellow, clear*	*0.04974*	*0.23*	*11250*	*16.98*	~~*122.1*~~	~~*17.6*~~	c
3	350*100 µm, uncolored, clear	0.04938	0.12	23213	12.90	136.6	7.3	
4	*400*120 µm, light yellow, clear*	*0.05007*	*0.19*	*8471*	*12.09*	~~*124.4*~~	~~*15.4*~~	c
5	*320*100 µm, light yellow, clear*	*0.05177*	*0.21*	*6745*	*8.90*	~~*176.2*~~	~~*14.9*~~	b
6	*300*100 µm, uncolored, clear*	*0.04985*	*0.25*	*10738*	*12.90*	~~*124.4*~~	~~*15.1*~~	c
7	300*100 µm, yellow, clear	0.04941	0.17	22652	16.90	137.5	10.4	
8	250*140 µm, uncolored, clear	0.04985	0.18	14484	11.80	140.7	10.5	
			F181	**mean age:**		**137.8**	**5.1**	
				intercept age:		**129.0**	**18.0**	

a: too large error
b: inherited component
c: lead loss
d: low $^{206}Pb/^{204}Pb$

Appendix 3 *(continued)*

Grain and samples		$^{207}Pb/^{206}Pb$	± 2σ (%)	$^{206}Pb/^{204}Pb$	± 2σ (%)	App. age (Ma)	±2σ (Ma)	reasons for rejection
F180-2								
4	*450*120 µm, light yellow, clear*	*0.05208*	*0.28*	*4846*	*15.30*	~~*150.8*~~	~~*27.0*~~	a
5	400*100 µm, uncolored, clear	0.05199	0.22	5086	4.30	153.4	11.3	
6	400*120 µm, uncolored, clear	0.05176	0.21	4985	5.57	138.2	13.0	
7	300*120 µm, uncolored, clear	0.05021	0.15	13655	10.60	154.6	9.5	
Multi (4)	4 Zr, uncolored, clear, step 1	0.05003	0.24	13138	20.48	144.3	19.0	
Multi (4)	4 Zr, uncolored, clear, step 2	0.04974	0.17	20312	10.05	149.1	7.9	
Multi (4)	4 Zr, uncolored, clear, step 3	0.04966	0.15	17798	15.37	140.9	10.6	
Multi (4)	4 Zr, uncolored, clear, step 4	0.05004	0.18	15416	11.70	152.4	10.0	
			F180-2	**mean age:**		**148.7**	**5.6**	
				intercept age:		**148.0**	**12.0**	
F220								
5 (2)	2 Zr 200*50, light yellow, clear	0.05119	0.22	6871	11.35	150.7	18.0	
6 (3)	3 Zr 200*50, light yellow, clear	0.05040	0.22	11187	8.59	152.7	10.8	
7 (2)	2 Zr 200*50, light yellow, clear	0.05105	0.21	10206	8.24	177.1	10.9	
8 (2)	2 grains 200*80, light yellow, clear	0.05178	0.22	6123	6.82	166.5	13.4	
10 (3)	3 grains 150*70, light yellow, clear	0.05145	0.29	7235	8.19	168.4	15.2	
11 (3)	3 grains small, light yellow, clear	0.05144	0.25	7824	6.51	174.7	11.9	
12 (2)	2 Zr, light yellow, clear	0.05105	0.19	10054	10.21	176.0	12.3	
13 (2)	2 Zr 200*60, light yellow, clear	0.05217	0.18	4745	5.32	151.8	12.4	
14 (2)	2 Zr 200*60, light yellow, clear	0.05193	0.33	6138	8.88	173.9	18.6	
15 (3)	3 Zr 200*60, light yellow, clear	0.05130	0.22	6452	5.94	149.3	11.8	
16 (2)	2 Zr 200*60, light yellow, clear	0.05122	0.28	8239	7.90	169.1	13.7	
17 (3)	3 Zr 200*40, light yellow, clear	0.05253	0.28	4543	5.98	162.3	16.2	
			F220	**mean age:**		**164.4**	**7.1**	
				intercept age:		**170.0**	**27.0**	see text

a: too large error
b: inherited component
c: lead loss
d: low $^{206}Pb/^{204}Pb$

Appendix 4:
SHRIMP analytical results

Appendix 4: *Summary of SHRIMP isotopic measurements and apparent ages*

	com ^{206}Pb (%)	$^{206}Pb/^{204}Pb$	U (ppm)	Th (ppm)	$^{232}Th/^{238}U$	$^{206}Pb^*$ (ppm)	$^{238}U/^{206}Pb$	± 1σ (%)	$^{207}Pb/^{206}Pb$	± 1σ (%)	Pb_{com} corrected: $^{207}Pb^*/^{235}U$	± 1σ (%)	$^{206}Pb^*/^{238}U$	± 1σ (%)	err. corr.	$^{206}Pb/^{238}U$ age (Ma)	± 1σ (Ma)	Pb_{com} corr. method	reason for rejection
RH330																			
1.1	0.34	5446	781	285	0.38	16.5	40.53	1.1	.0512	2.0	.1644	4.22	.0246	1.14	0.270	156.6	1.8	4	
2.1	0.49	3730	500	141	0.29	9.7	44.45	1.2	.0530	2.5	.1516	6.65	.0224	1.29	0.195	142.7	1.8	4	outlier
3.1	0.28	6630	612	174	0.29	12.8	41.06	1.2	.0507	2.3	.1624	4.37	.0243	1.19	0.273	154.7	1.8	4	
4.1	0.18	9963	1465	500	0.35	32.8	38.33	1.0	.0506	1.4	.1765	2.18	.0260	1.02	0.469	165.7	1.7	4	
5.1	0.20	9319	696	252	0.37	14.7	40.65	1.1	.0512	2.1	.1682	3.73	.0246	1.16	0.310	156.4	1.8	4	
6.1	0.23	8054	701	401	0.59	39.4	15.29	1.0	.0558	1.2	.4855	1.88	.0653	1.03	0.547	407.5	4.1	4	core
7.1	0.44	4158	630	160	0.26	13.5	40.20	1.2	.0515	2.1	.1638	3.71	.0248	1.17	0.316	157.7	1.8	4	
7.2	bd	-	1409	331	0.24	30.4	39.78	1.0	.0492	1.5	.1707	1.78	.0251	1.03	0.576	160.0	1.6	no corr.	
8.1	0.15	12603	1160	315	0.28	25.4	39.29	1.0	.0498	1.6	.1706	2.47	.0254	1.05	0.427	161.8	1.7	4	
9.1	0.68	2672	437	140	0.33	9.2	40.64	1.3	.0514	2.6	.1545	6.35	.0244	1.30	0.204	155.7	2.0	4	
10.1	0.16*	-	502	183	0.38	20.0	21.59	1.1	.0544	1.9	.3386	3.57	.0462	1.19	0.334	291.4	3.4	8	core
11.1	0.08*	-	384	95	0.25	8.2	40.30	1.3	.0524	2.8	.1767	4.26	.0248	1.37	0.321	157.9	2.1	8	
12.1	bd	-	1043	314	0.31	22.3	40.23	1.1	.0497	1.7	.1703	1.99	.0249	1.06	0.536	158.3	1.7	no corr.	
F216																			
1.1	0.12*	-	773	6	0.01	16.1	41.33	1.1	.0498	2.1	.1626	2.46	.0242	1.14	0.463	154.0	1.7	8	lead loss
1.2	0.21	8575	96	49	0.53	32.4	2.54	1.3	.1632	0.9	8.765	1.68	.3931	1.32	0.790	2137.1	24.1	4	core
2.1	0.31	5968	182	102	0.58	8.9	17.57	1.4	.0569	2.7	.4260	4.99	.0567	1.41	0.282	355.7	4.9	4	core
3.1	0.17	10550	1653	371	0.23	37.3	38.11	1.0	.0501	1.4	.1758	2.40	.0262	1.02	0.427	166.7	1.7	4	
3.2	0.12	14649	246	128	0.54	17.0	12.40	1.2	.0602	1.9	.6573	2.74	.0806	1.22	0.444	499.5	5.9	4	core
4.1	0.00	-	1058	52	0.05	23.2	39.22	1.1	.0491	1.8	.1727	2.06	.0255	1.08	0.523	162.3	1.7	no corr.	
4.2	0.40	4595	430	301	0.72	18.6	19.90	1.1	.0534	1.8	.3468	3.62	.0500	1.14	0.316	314.8	3.5	4	core
5.1	bd	-	1932	353	0.19	43.1	38.49	1.0	.0500	1.2	.1790	1.57	.0260	0.99	0.633	165.4	1.6	no corr.	
6.1	0.36*	-	298	69	0.24	6.4	40.17	1.4	.0492	3.3	.1583	5.12	.0248	1.47	0.286	157.9	2.3	8	
7.1	bd	-	602	153	0.26	26.0	19.90	1.1	.0536	1.6	.3717	1.92	.0503	1.08	0.563	316.1	3.3	no corr.	core
8.1	0.05	35425	1562	582	0.38	70.3	19.08	1.0	.0535	0.9	.3836	1.49	.0524	0.97	0.653	329.2	3.1	4	core
9.1	0.11	16553	1782	327	0.19	38.8	39.45	1.0	.0490	1.3	.1679	1.90	.0253	1.00	0.527	161.2	1.6	4	
10.1	1.32	1387	232	70	0.31	8.0	24.92	1.3	.0572	2.7	.2543	9.77	.0396	1.45	0.148	250.3	3.5	4	core
11.1	0.19	9527	514	133	0.27	22.7	19.44	1.1	.0529	1.6	.3639	2.60	.0513	1.10	0.421	322.7	3.5	4	core
12.1	0.03	65133	979	113	0.12	21.8	38.65	1.1	.0499	1.8	.1770	2.31	.0259	1.08	0.468	164.6	1.8	4	

8: 208 corrected
4: 204 corrected
* : from 208 correction
bd: below detection limit (no common lead neither with 204 nor 208 correction)
calibration constant calculated after 204 corrected Pb/U:UO/U^2 curve

Appendix 5a:
Whole rock analyses (Permo-Carboniferous group)

Appendix 5a: *Major and trace elements XRF analyses of the gneisses belonging to the Permo-Carboniferous group. Rock types after de la Roche et al. (1980). g: granite; gd: granodiorite; t: tonalite*

Sample	RH11	RH31	RH60	RH78	RH79	RH87	RH89	RH123	RH130	RH132	RH336	F127	F34
Rock type		gd	gd	t	g	gd	g		gd	g	g	gd	gd
Major elements (wt %)													
SiO_2	80.23	70.62	67.35	62.78	72.26	68.44	73.11	77.56	72.35	71.32	73.55	66.95	70.55
TiO_2	0.13	0.32	0.60	0.70	0.32	0.54	0.22	0.14	0.23	0.29	0.21	0.47	0.34
Al_2O_3	9.62	15.35	15.56	15.82	14.40	15.04	14.42	11.41	14.44	15.22	14.05	16.20	15.48
Fe_2O_3	0.50	2.43	3.71	5.49	2.34	3.65	1.82	1.46	1.87	2.24	1.71	3.87	2.17
MnO	0.01	0.05	0.07	0.13	0.04	0.08	0.02	0.01	0.04	0.05	0.02	0.06	0.04
MgO	0.24	0.58	1.27	2.19	0.49	1.32	0.57	0.14	0.38	0.57	0.43	1.12	0.77
CaO	1.38	2.57	2.53	4.32	1.75	2.88	1.52	0.08	2.12	1.91	0.69	3.31	2.38
Na_2O	1.78	4.33	3.53	3.32	3.46	3.02	3.60	0.29	4.14	4.46	2.80	3.73	3.68
K_2O	4.12	2.81	3.94	3.58	4.13	3.77	3.61	7.12	2.94	3.16	4.71	3.03	3.73
P_2O_5	0.05	0.11	0.20	0.21	0.15	0.11	0.09	0.06	0.06	0.10	0.10	0.21	0.11
LOI	1.85	0.44	1.10	0.93	0.54	0.96	0.86	0.89	0.46	0.54	1.21	0.64	0.83
Total	99.91	99.60	99.86	99.45	99.88	99.83	99.84	99.16	99.02	99.87	99.47	99.60	100.06
A/CNK	0.97	1.03	1.06	0.92	1.08	1.05	1.15	1.37	1.04	1.07	1.28	1.05	1.07
A/NK	1.30	1.51	1.54	1.69	1.42	1.66	1.47	1.39	1.45	1.41	1.45	1.72	1.53
Trace elements (ppm)													
La	15	40	44	28	57	17	29	34	25	32	22	30	37
Ce	27	82	69	61	116	48	66	59	45	60	39	64	76
Nd	13	33	33	23	50	22	24	26	21	24	18	26	28
Sm	4	7	4	4	7	bd	5	5	3	5	9	4	4
Sc	4	7	8	7	7	9	6	0	3	5	3	6	6
V	14	25	66	107	23	60	14	21	17	26	16	51	37
Cr	12	8	14	15	13	9	7	11	3	4	4	8	21
Co	bd	3	5	10	bd	5	4	bd	4	4	bd	6	3
Ni	bd	3	6	3	bd	4	bd	2	bd	4	2	bd	5
Cu	2	bd	17	7	2	4	bd	5	bd	bd	5	3	8
Zn	14	49	76	61	56	57	46	19	43	46	51	64	38
Ga	10	20	20	15	20	18	18	11	18	19	18	21	20
Rb	98	77	150	110	145	149	101	154	80	82	162	86	104
Sr	69	536	481	592	261	200	241	165	467	522	144	487	382
Y	11	13	18	33	18	21	10	8	15	13	16	20	10
Zr	81	189	195	144	209	132	144	123	137	169	131	183	143
Nb	4	8	17	19	13	14	7	5	8	9	11	9	10
Ba	415	885	999	1151	906	557	1120	1587	887	1089	832	1005	796
Pb	15	22	23	16	26	23	26	28	23	18	26	19	22
Th	9	13.2	17.3	16.5	26	14.1	12.2	14.3	10.9	8.5	15.6	8.4	17.6
U	0.8	0.8	3	5.1	5.1	3.6	1.3	0.5	2.4	2.6	1.5	0.9	1.7

bd: below detection limit

Appendix 5b: Whole rock analyses (Late-Jurassic group)

Appendix 5b: *Major and trace elements XRF analyses of the gneisses belonging to the Late-Jurassic group. Rock types after de la Roche et al. (1980). g: granite; gd: granodiorite; t: tonalite*

Sample	RH126	RH330	F180-1	F180-2	F181	F190	F203	F206	F207	F216	F220	F224	F225	F226
Rock type	gd	t	t	t	gd	t	gd	gd	gd	gd	g	gd	gd	gd
Major elements (wt %)														
SiO_2	68.74	60.29	61.24	61.52	67.28	62.93	69.03	68.32	64.92	67.96	64.34	65.30	68.79	63.77
TiO_2	0.66	0.59	0.79	0.75	0.52	0.70	0.38	0.42	0.61	0.46	0.97	0.64	0.44	0.77
Al_2O_3	15.78	17.56	17.31	17.57	16.03	17.82	15.39	15.31	16.78	15.71	16.03	15.75	15.38	16.08
Fe_2O_3	3.61	5.12	5.86	5.86	3.99	5.07	3.17	3.20	4.86	3.64	5.97	5.26	3.42	6.08
MnO	0.06	0.08	0.10	0.10	0.08	0.08	0.05	0.08	0.09	0.04	0.11	0.10	0.08	0.13
MgO	1.18	2.36	2.19	2.20	1.39	1.96	1.14	0.95	1.97	1.49	2.43	2.10	1.05	2.30
CaO	3.62	4.69	4.52	4.70	3.43	4.68	2.61	2.81	3.68	2.91	1.41	3.50	2.82	3.27
Na_2O	3.67	3.94	3.57	3.78	3.77	3.97	3.74	3.60	3.60	3.75	4.33	3.16	3.90	3.41
K_2O	1.97	2.26	2.02	2.07	1.91	2.03	3.04	3.40	2.48	2.95	3.34	2.09	2.69	2.48
P_2O_5	0.13	0.14	0.20	0.18	0.16	0.19	0.20	0.16	0.18	0.14	0.09	0.05	0.12	0.08
LOI	0.73	1.74	2.02	1.07	0.60	1.31	1.04	1.10	0.77	0.75	1.00	0.93	1.20	1.32
Total	100.16	98.78	99.83	99.79	99.30	99.87	99.80	99.35	100.20	99.79	100.01	100.10	99.46	99.69
A/CNK	1.07	1.01	1.06	1.03	1.11	1.03	1.08	1.04	1.10	1.07	1.21	1.14	1.06	1.13
A/NK	1.93	1.97	2.15	2.08	1.94	2.04	1.63	1.59	1.95	1.68	1.49	2.11	1.65	1.94
Trace elements (ppm)														
La	37	19	5	7	33	28	9	33	10	15	23	28	20	32
Ce	78	39	14	21	63	61	26	67	22	34	52	52	38	66
Nd	30	17	10	12	28	27	11	29	14	18	25	23	18	31
Sm	4	4	4	3	6	4	bd	4	6	4	4	7	4	6
Sc	11	15	14	19	14	14	9	6	13	13	18	18	10	17
V	75	117	113	118	69	93	56	44	94	73	105	106	53	115
Cr	14	30	31	30	24	16	30	bd	30	26	9	54	11	58
Co	12	14	11	12	8	10	5	3	11	10	14	13	5	14
Ni	5	14	13	16	10	9	12	4	14	12	8	26	8	30
Cu	7	15	15	16	12	11	17	4	17	18	4	29	8	26
Zn	51	68	79	70	57	72	49	65	64	34	91	64	53	85
Ga	17	20	19	20	17	20	18	20	19	17	20	18	19	20
Rb	78	78	71	84	99	96	106	111	109	116	122	100	115	125
Sr	444	334	419	334	271	339	327	425	237	213	153	230	230	223
Y	12	22	17	24	6	26	15	19	22	19	33	7	23	23
Zr	169	129	196	177	150	200	126	175	132	130	272	155	135	162
Nb	7	9	10	9	11	6	8	13	12	10	11	13	10	12
Ba	842	683	653	608	465	594	806	994	565	532	550	484	617	372
Pb	16	24	17	14	14	19	25	21	22	24	16	15	32	21
Th	16.5	8.4	2.3	4.5	12.6	9.5	5.2	15.8	4.9	8.4	9.5	9.5	11.6	16.6
U	3.3	2.4	2.5	1.6	3.4	2.4	1.9	3.4	2.1	3.3	2.6	3.1	4	bd

bd: below detection limit

Appendix 6: Mineral analyses used in thermobarometric calculations

Appendix 6: Mineral analyses used for thermobaric estimations of samples F101-1 and F101-2.

Sample F101-1							
Analytical number	**Grt 81**	**Grt 386**	**Grt 394**	**Bt 82**	**Bt 83**	**Pl 84**	**Mu 119**
Mineral	**garnet**	**garnet**	**garnet**	**biotite**	**biotite**	**plagioclase**	**muscovite**
SiO_2	38.54	37.87	37.70	37.29	36.24	65.83	47.18
TiO_2	0.00	0.00	0.00	0.98	1.51	0.00	0.84
Al_2O_3	21.64	21.81	21.54	21.23	20.00	21.13	33.00
Cr_2O_3	0.10	0.03	0.02	0.04	0.02	0.05	0.04
Fe_2O_3	0.31	2.44	1.04	0.00	0.00	0.22	0.43
FeO	32.29	31.15	31.06	15.05	18.00	0.00	2.04
MnO	1.77	1.40	5.19	0.14	0.17	0.00	0.00
MgO	5.78	6.40	3.52	10.76	10.16	0.00	1.46
CaO	1.21	0.84	1.76	0.07	0.00	1.89	0.00
Na_2O	0.03	0.05	0.05	0.25	0.24	10.56	0.84
K_2O	0.00	0.00	0.00	8.22	8.82	0.11	9.67
Totals	101.67	102.00	101.87	94.05	95.18	99.79	95.51
Oxygens	12.00	12.00	12.00	11.00	11.00	8.00	11.00
Si	3.00	2.94	2.97	2.77	2.72	2.90	3.14
Ti	0.00	0.00	0.00	0.06	0.09	0.00	0.04
Al	1.99	1.99	2.00	1.86	1.77	1.10	2.59
Cr	0.01	0.00	0.00	0.00	0.00	0.00	0.00
Fe^{3+}	0.02	0.14	0.06	0.00	0.00	0.01	0.02
Fe^{2+}	2.10	2.02	2.05	0.94	1.13	0.00	0.11
Mn	0.12	0.09	0.35	0.01	0.01	0.00	0.00
Mg	0.67	0.74	0.41	1.19	1.14	0.00	0.15
Ca	0.10	0.07	0.15	0.01	0.00	0.09	0.00
Na	0.01	0.01	0.01	0.04	0.04	0.90	0.11
K	0.00	0.00	0.00	0.78	0.85	0.01	0.82
Sum Cation	8.00	8.00	8.00	7.65	7.75	5.00	6.98
End member proportion:							
Almandine	70.30	69.13	69.26				
Andradite	0.89	6.86	3.01				
Grossulare	2.17	-	1.97				
Pyrope	22.43	25.32	13.99				
Spessartine	3.90	3.15	11.72				
Uvarovite	0.30	0.09	0.05				
An						8.93	
Ab						90.47	
Or						0.60	

Appendix 6 (continued)

	Sample F101-2											
Analytical number	**Grt 18**	**Grt 45**	**Grt 53**	**Mu 21**	**Pl 20**	**Pl 48**	**Pl 49**	**Pl 56**	**Pl 57**	**Bt 17**	**Bt 47**	**Bt 55**
Mineral	**garnet**	**garnet**	**garnet**	**muscovite**	**plagioclase**	**plagioclase**	**plagioclase**	**plagioclase**	**plagioclase**	**biotite**	**biotite**	**biotite**
SiO_2	38.98	38.34	38.63	47.19	62.99	62.42	60.22	62.03	60.24	36.57	37.45	36.04
TiO_2	0.00	0.01	0.00	0.95	0.00	0.00	0.00	0.00	0.01	2.38	2.31	1.78
Al_2O_3	22.18	21.61	21.78	34.07	22.97	23.79	25.06	23.87	25.05	19.87	18.73	19.04
Cr_2O_3	0.02	0.04	0.00	0.08	0.07	0.06	0.03	0.00	0.01	0.00	0.05	0.05
Fe_2O_3	0.54	0.36	0.41	0.00	0.00	0.10	0.09	0.13	0.06	0.00	0.00	0.94
FeO	29.42	29.46	29.30	1.30	0.00	0.00	0.00	0.00	0.00	17.45	16.63	17.32
MnO	0.84	2.58	2.39	0.05	0.00	0.00	0.00	0.00	0.00	0.19	0.18	0.23
MgO	7.28	4.34	5.25	1.49	0.00	0.00	0.00	0.00	0.00	10.64	11.24	10.88
CaO	2.52	4.50	3.99	0.00	4.39	5.07	6.68	5.39	6.84	0.00	0.00	0.01
Na_2O	0.03	0.04	0.00	0.56	9.22	8.77	7.84	8.55	7.69	0.17	0.25	0.11
K_2O	0.00	0.03	0.00	10.17	0.20	0.12	0.11	0.15	0.15	9.43	9.01	8.24
Totals	101.81	101.30	101.75	95.87	99.83	100.33	100.03	100.12	100.05	96.71	95.87	94.66
Oxygens	12.00	12.00	12.00	11.00	8.00	8.00	8.00	8.00	8.00	11.00	11.00	11.00
Si	2.99	3.00	2.99	3.12	2.79	2.76	2.68	2.75	2.68	2.71	2.78	2.72
Ti	0.00	0.00	0.00	0.05	0.00	0.00	0.00	0.00	0.00	0.13	0.13	0.10
Al	2.00	1.99	1.99	2.65	1.20	1.24	1.32	1.25	1.31	1.73	1.64	1.69
Cr	0.00	0.00	0.00	0.00	0.00	0.00	0.00	0.00	0.00	0.00	0.00	0.00
Fe^{3+}	0.03	0.02	0.02	0.00	0.00	0.00	0.00	0.00	0.00	0.00	0.00	0.05
Fe^{2+}	1.88	1.93	1.90	0.07	0.00	0.00	0.00	0.00	0.00	1.08	1.03	1.09
Mn	0.05	0.17	0.16	0.00	0.00	0.00	0.00	0.00	0.00	0.01	0.01	0.02
Mg	0.83	0.51	0.61	0.15	0.00	0.00	0.00	0.00	0.00	1.17	1.24	1.22
Ca	0.21	0.38	0.33	0.00	0.21	0.24	0.32	0.26	0.33	0.00	0.00	0.00
Na	0.00	0.01	0.00	0.07	0.79	0.75	0.68	0.73	0.66	0.03	0.04	0.02
K	0.00	0.00	0.00	0.86	0.01	0.01	0.01	0.01	0.01	0.89	0.85	0.79
Sum Cation	8.00	8.00	8.00	6.97	5.01	5.00	5.00	5.00	5.00	7.75	7.72	7.71
End member proportion:												
Almandine	63.31	64.64	63.43									
Andradite	1.53	1.03	1.18									
Grossulare	5.35	11.50	9.89									
Pyrope	27.92	16.98	20.26									
Spessartine	1.82	5.73	5.24									
Uvarovite	0.07	0.12	0.00									
An						24.05	31.84	32.67	22.88			
Ab						75.25	67.56	66.53	76.01			
Or						0.70	0.60	0.80	1.11			

References

Anders, B., Reischmann, T., Poller, U. 2002. Geochemistry and Geochronology of Basement Rocks from the Pelagonian Zone, Greece. *Geochimica et Cosmochimica Acta*, **66**, A19 (abstr.).

Anders, B., Reischmann, T., Poller, U., Kostopoulos, D. 2005. Age and origin of granitic rocks of the eastern Vardar Zone, Greece: newconstraints on the evolution of the Internal Hellenides. *Journal of the Geological Society, London*, **162**, 1-14.

Anders, B., Reischmann, T., Kostopoulos, D., Poller, U. 2005. The oldest rocks of Greece: first evidence for a Precambrian terrane within the Pelagonian Zone. *Geological Magazine*, **in press**.

Andersen, T. B., Jamtveit, B., Dewey, J. F., Swensson, E. 1991. Subduction and eduction of continental crust; major mechanisms during continent-continent collision and orogenic extensional collapse, a model based on the South Norwegian Caledonides. *Terra Nova*, **3**, 303-310.

Ansdell, K. M., Kyser, K. T. 1993. Textural and chemical changes undergone by zircon during the Pb-evaporation technique. *American Mineralogist*, **78**, 36-41.

Aubouin, J. 1959. Contribution à l'étude géologique de la Grèce septentrionale: les confins de l'Epire et de la Thessalie. *Annales Géologique des Pays helléniques*, **10**, 403.

Aubouin, J., Brunn, J. H., Celet, P., Dercourt, J., Godfriaux, I., Mercier, J., Lys, M., Marie, P., Neumann, M., Sigal, J., Sornay, J. 1960. Le Crétacé supérieur en Grèce. *Bulletin de la Société géologique de France*, **7**, (II): 452-469.

Barr, S. R., Temperley, S., Tarney, J. 1999. Lateral growth of the continental crust through deep level subduction-accretion: a re-evaluation of central Greek Rhodope. *Lithos*, **46**, 69-94.

Bebien, J., Ohnenstetter, D., Ohnenstetter, M., Vergely, P. 1980. Diversity of the Greek ophiolites; birth of oceanic basins in transcurrent systems. In: *Tethyan ophiolites; Vol. 2, Eastern area* (Ed G. Rocci), pp. 129-197. Ofioliti, special issue.

Beyssac, O., Chopin, C. 2003. Comment on "Diamond, former coesite and supersilicic garnet in metasedimentary rocks from the Greek Rhodope: a new ultrahigh-pressure metamorphic province established" by E. D. Mposkos and D. K. Kostopoulos, EPSL, 192 (2001), 497-506. *Earth and Planetary Science Letters*, **214**, 669-674.

Black, L. P., Kamo, S. L., Allen, C. M., Aleinikoff, J. N., Dais, D. W., Korsch, R. J., Foudoulis, C. 2003. TEMORA 1: a new zircon standard for Phanerozoic U-Pb geochronology. *Chemical Geology*, **200**, 155-170.

Boccaletti, M., Manetti, P., Peccerillo, A. 1974. The Balkanids as an instance of back-arc thrust belt: possible relation with the Hellenids. *Geological Society of America Bulletin*, **85**, 1077-1084.

Bonev, N. G., Stampfli, G. 2003. New structural and petrologic data on Mesozoic schists in the Rhodope (Bulgaria): geodynamic implications. *Comptes Rendus Geoscience*, **335**, 691-699.

Bonneau, M. 1982. Evolution géodynamique de l'ars égéen depuis le Jurassic superieur jusqu'au Miocène. *Bulletin de la Sociétée géologique de France*, **XXIV**, (7): 229-242.

Bornovas, J., Rondogianni-Tsiambaou, T. 1983. Geological Map of Greece. Institute of Geology and Mineral Exlopartion of Greece (IGME), Athens.

Boyanov, I., Ruseva, M., Dimitrova, E. 1982. First find of Upper Cretaceous foraminifera in East Rhodopes. *Geologica Balcanica*, **12**, (4): 20.

Brown, S. A. M., Robertson, A. H. F. 2004. Evidence for Neotethys rooted within the Vardar suture zone from the Voras Massif, northernmost Greece. *Tectonophysics*, **381**, 143-173.

Bröcker, M., Kreuser, H., Matthews, A., Okrusch, M. 1993. $^{39}Ar/^{40}Ar$ and oxygen isotope studies of polymetamorphism from Tinos Island, Cycladic blueschist belt, Greece. *Journal of metamorphic Geology*, **11**, 223-240.

Bröcker, M., Enders, M. 1999. U–Pb zircon geochronology of unusual eclogite-facies rocks from Syros and Tinos (Cyclades, Greece). *Geological Magazine*, **136**, (2): 111-118.

Brunn, J. H. 1960. Les zones helléniques internes et leur extension. Réflexion sur l'orogenèse alpine. *Bulletin de la Société géologique de France*, **7**, (II): 470-486.

Burg, J.-P., Ivanov, Z., Ricou, L.-E., Dimov, D., Klain, L. 1990. Implications of shear-sense criteria for the tectonic evolution of the Central Rhodope massif, southern Bulgaria. *Geology*, **18**, 451-454.

Burg, J.-P., Godfriaux, I., Ricou, L.-E. 1995. Extension of the Mesozoic Rhodope thrust units in the Vertiskos-Kerdilion Massifs (Northern Greece). *Comptes Rendus de l'Academie des Sciences de Paris, série II a*, **320**, 889-896.

Burg, J.-P., Ricou, L-E., Ivanov, Z., Godfriaux, I., Dimov, D., Klain, L. 1996. Syn-metamorphic nappe complex in the Rhodope Massif. Structure and kinematics. *Terra Nova*, **8**, 6-15.

Carrigan, C. W., Mukasa, S. B., Haydoutov, I., Kolcheva, K. 2003. Constrating styles of Variscan granitic plutonism, central Bulgaria: a zircon and monazite U-Th-Pb geochronologic study. *Geological Society of America Abstract Program*, **35**, (6): 554.

Cavazza, W., Roure, F., Ziegler, P. A. 2004. The Mediterranean Area and the Surrounding Regions: Actve Processes, Remnants of Former Tethyan Oceans and Related Thrust Belts. In: *The TRANSMED Atlas* (Ed W. Cavazza, Roure, F.,Spakman, W., Stampfli, G. M., Ziegler, P. A.), pp. 1-29. Springer, Berlin Heidelberg.

Chappell, B. W., White, A. J. R. 1974. Two contrasting granite types. *Pacific Geology*, **8**, 173-4.

Cheniak, D. J., Watson, E. B. 2000. Pb diffusion in Zircon. *Chemical Geology*, **172**, 5-24.

Ciobanu, C. L., Cook, N. J., Stein, H. 2002. Regional setting and geochronology of the Late Cretaceous Banatitic Magmatic and Metallogenetic Belt. *Mineralum Deposita*, **37**, 541-567.

Claoué-Long, J. C., Compston, W., Roberts, J., Fanning, C. M. 1995. Two Carboniferous ages: A comparison of SHRIMP zircon dating with conventional zircon ages and $^{40}Ar/^{39}Ar$ analysis. In: *Geochronology, time scales and global stratigraphic correlations* (Ed K. Berggren W. A., D.V., Aubry, M-P., Hardenbol, J.), **No 4**, pp. 3-21. SEPM (Society for Sedimentary Geology) special publication.

Corfu 2003. Atlas of Zircon Textures. In: *Zircon* (Ed J. M. Hanchar, Hoskin, P. W. O.), *Reviews in Mineralogy & Geochemistry*, **53**, pp. 469-500. Mineralogical Society of America, Washington.

Cortesogno, L., Gaggero, L., Ronchi, A., Yanev, S. 2004. Late orogenic magmatism and sedimentation within Late Carboniferous to Early Permian basins in the Balkan terrane (Bulgaria): geodynamic implications. *International Journal of Earth Sciences*, **93**, 500-520.

de Bono, A. 1998. Pelagonian margins in Central Evia Island (Greece). Stratigraphy and geodynamic evolution, Université de Lausanne, Lausanne, 134 pp.

de La Roche, H., Leterrier, J., Grandclaude, P., Marchal, M. 1980. A classification of volcanic and plutonic rocks using R1-R2 diagram and major element analyses. Its relationships with current nomenclature. *Chemical Geology*, **29**, 183-210.

de Laeter, J. R. 1998. Mass spectrometry and geochronology. *Mass Spectrometry Reviews*, **17**, 97-125.

Degnan, P. J., Robertson, A. H. F. 1998. Mesozoic-early Teriary passive margin evolution of the

Pindos ocean (NW Peloponnese, Greece). *Sedimentary Geology*, **117**, 33-70.

Dercourt, J., Zonenshain, L. P., Ricou, L.-E., Kazmin, V. G., Le Pichon, X., Knipper, A. L., Grandjacquet, C., Sbortshikov, I. M., Geyssant, J., Lepvrier, C., Pechersky, D. H., Boulin, J., Sibuet, J.-C., Savostin, L. A., Sorokhtin, O., Westphal, M., Bazhenov, M. L., Lauer, J.-P., Biju-Duval, B. 1986. Geological evolution of the Tethys belt from the Atlantic to the Pamirs since the Lias. *Tectonophysics*, **123**, 241-315.

Dinter, D. A., Royden, L. 1993. Late Cenozoic extension in northeastern Greece: Strymon Valley detachment system and Rhodope metamorphic core complex. *Geology*, **21**, 45-48.

Dinter, D. A., Macfarlane, A., Hames, W., Isachen, C., Bowring, S., Royden, L. 1995. U-Pb and $^{40}Ar/^{39}Ar$ geochronology of the Symvolon granodiorite: Implications for the thermal and structural evolution of the Rhodope metamorphic core complex, northeastern Greece. *Tectonics*, **14**, (4): 886-908.

Dinter, D. A. 1998. Late Cenozoic extention of the Alpine collosional orogen, northeastern Greece: Origin of the north Aegean basin. *GSA bulletin*, **110**, (9): 1208-1230.

Dixon, J. E., Dimitriadis, S. 1984. Metamorphosed ophiolitic rocks from the Serbo-Macedonian Massif, near Lake Volvi, North-east Greece. In: *The Geological Evolution of the Eastern Mediterranean* (Ed J. E. Dixon, Robertson, A. H. F.), *Geological Society of London special publications*, **17**, pp. 603-618. Blackwell Scientific Publications.

Dougherty-Page, J. S., Barlett, J. M. 1999. New analytical procedures to increase the resolution of zircon geochronology by the evaporation technique. *Chemical Geology*, **153**, 227-240.

Finger, F., Steyrer, H. P. 1990. I-type granitoids as indicators of a late Paleozoic convergent ocean-continent margin along the southern flank of the central European Variscan orogen. *Geology*, **18**, 1207-1210.

Förster, H.-J., Tischendorf, G., Trumbull, R. B. 1997. An evaluation of the Rb vs. (Y+Nb) discrimination diagram to infer tectonic setting of silicic igneous rocks. *Lithos*, **40**, 261-293.

Gautier, P., Brun, J. P. 1994. Crustal-scale geometry and kinematics of late-orogenic extension in the central Aegean (Cyclades and Evvia Island). *Tectonophysics*, **238**, 399-424.

Gautier, P., Brun, J. P., Moriceau, R., Sokoutis, D., Martinod, J., Jolivet, L. 1999. Timing, kinematics and cause of Aegean extension: a scenario based on a comparison with simple analogue experimens. *Tectonophysics*, **315**, 31-72.

Gebauer, D. 1990. Isotopic systems - geochronology of eclogites. In: *Eclogite Facies Rocks* (Ed D. A. Carswell), pp. 141-159. Blackies, Glasgow-London.

Geisler, T., Ulonska, M., Schleicher, H., Pidgeon, R. T., van Bronswijk, W. 2001. Leaching and differential recrystallization of metamict zircon under experimental hydrothermal conditions. *Contributions to Mineralogy and Petrology*, **141**, 53-65.

Georgieva, M., Cherneva, Z., Mogessie, A. 2003. Geochemistry of metamorphozed hercynian granites from the Central Rhodopian Dome, Bulgaria. *Geophysical Research Abstracts*, **5**, 13058.

Gerdjikov, I., Gautier, P., Cherneva, Z., Kostopoulos, D. 2003. Tectonic setting of ultrahigh-pressure metamorphic rocks from Chepelare area, Central Rhodopes. In: *Annual conference of Bugarian Geological Society*.

Goranov, A., Atanasov, G. 1992. Lithostratigraphy and formation conditions of Maastrichtian-Paleocene deposits in Krumovgrad District. *Geologica Balcanica*, **22**, (3): 71-82.

Graf, J. 2001. Alpine tectonics in western Bulgaria: Cretaceous compression of the Kraište region and Cenozoic exhumation of the crystalline Osogovo-Lisec Complex. PhD, Swiss Federal Institute of Technology, Zürich, 197 pp.

Guiraud, M., Ivanov, Z., Burg, J.-P. 1992. Découverte de schistes de haute pression dans la région de Biala Tchekva (Rhodope Central, Bulgarie). *Comptes Rendus de l'Academie des Sciences de Paris*, **315**, 1695-1702.

Hermann, J., Rubatto, D., Korsakov, A, Shatsky, V. S. 2001. Multiple zircon growth during fast exhumation of diamondiferous, deeply subducted continental crust (Kokchetav Massif, Kazakhstan). *Contribution to Mineralogy and*

Petrology, **141**, 66-82.

Himmerkus, F., Reischmann, T. & Kostopoulus, D. 2003. First evidence for Silurian magmatism in the Serbo-Macedonian Massif, northern Greece. *Geochimica et Cosmochimica Acta*, **66**, A330 (abstr.).

Hintorne, J. R., Andersen, C. A., Conrad, R. L., Lovering, J. F. 1979. Single-grain $^{207}Pb/^{206}Pb$ and U/Pb age determinations with a 10 µm spatial resolution using the ion microprobe mass analyser (IMMA). *Chemical Geology*, **25**, 271-303.

Hoffman, J. F., Long, J. V. P. 1984. Unusual sector zoning in Lewisian zircons. *Mineralogical Magazine*, **48**, 513-517.

Holland, T. J. B., Powell, R. 1998. An internally consistent thermodynamic data set for phases of petrological interest. *Journal of Metamorphic Geology*, **16**, 309-343.

Hoskin, P. W. O., Black, L. P. 2000. Metamorphic zircon formation by solid-state recrystallization of protolith igneous zircon. *Journal of metamorphic Geology*, **18**, 423-439.

Howell, D. G. 1989. Tectonics of Suspect Terranes. Topics in the Earth Sciences, **4**. Chapman and Hall, London, 232 pp.

Hsü, K. J., Nachev, I. K., Vuchev, V. T. 1977. Geologic evolution of Bulgaria in light of plate tectonics. *Tectonophysics*, **40**, 245-256.

Innocenti, F., Kolios, N., Manetti, P., Mazzuoli, R., Peccerillo, G., Rita, F., Villari, L. 1984. Evolution and Geodynamic Significance of the Tertiary Orogenic Volvanism in Northeastern Greece. *Bulletin Volcanologique*, **47**, (1): 25-37.

Ireland, T. R., Williams, I. S. 2003. Considerations in Zircon Geochronology by SIMS. In: *Zircon* (Ed J. M. Hanchar, Hoskin, P. W. O.), *Reviews in Mineralogy & Geochemistry*, **53**, pp. 215-241. Mineralogical Society of America, Washington.

Irvine, T. N., Baragar, W. R. A. 1971. A guide to the chemical classification of the common volcanic rocks. *Canadian Journal of Earth Science*, **8**, 523-548.

Ivanov, R. 1981. The deep-seated Central-Rhodope Nappe and the interference tectonics of the Rhodope crystalline basement. *Geologica Balcanica*, **11**, (3): 47-66.

Ivanov, Z. 1988. Apercu général sur l'évolution géologique et structurale du massif des Rhodopes dans le cadre des Balkanides. *Bulletin de la Sociétée géologique de France*, **8**, (IV-2): 227-240.

Janousek, V., Farrow, C. M., Erban, V. 2003. GCDkit: new PC software for interpretation of whole-rock geochemical data from igneous rocks. *Geochimica et Cosmochimica Acta*, **67**, A186 (abstr.).

Jolivet, L., Brun, J. P., Gautier, P., Lallemant, S., Patriat, M. 1994. 3-D kinematics of extension in the Aegean from the Early Miocene to the Present, insight from the ductile crust. *Bulletin de la Société géologique de France*, **165**, 195-209.

Jolivet, L., Goffé, B., Monié, P., Truffert-Luxey, C., Patriat, M., Bonneau, M. 1996. Miocene detachment in Crete and exhumation P-T-t paths of high-pressure metamorphic rocks. *Tectonics*, **15**, (6): 1129-1153.

Jolivet, L., Rimmelé, G., Oberhaensli, R., Goffé, B., Candan, O. 2004. Correlation of syn-orogenic tectonic and metamorphic events in the Cyclades, the Lycian nappes and the Menderes massif. Geodynamic implications. *Bulletin de la Société géologique de France*, **175**, (3): 217-238.

Jordan, H. 1969. Geologie und Petrpgraphie im Zentrateil des Bos Dag (Drama, Griechisch-Makedonien). *Geotektonische Forschungen*, **31**, 50-85.

Kaneko, Y., Maruyama, S., Terabayashi, M., Yamamoto, H., Ishikawa, M., Anma, R., Parkinson, C. D., Ota, T., Nakajima, Y., Katayama, I., Yamamoto, J., Yamauchi, K. 2000. Geology of the Kokchetav UHP-HP metamorphic belt, Northern Kazakhstan. *The Island Arc*, **9**, 264-283.

Kaufman, P. S. 1995. Extentional tectonic history of the Rhodope metamorphic complex, Greece and geophysical modelling of the Halloran Hills, California. Phd, Massachusetts Institute of Technology, Cambridge, 295 pp.

Kazim, V. G., , Sbortshikov, I. M., Ricou, L-E., Zonenshain, L. P., Boulin, J., Knipper, A. L. 1986. Volcanic belts as markers of the

Mesozoic-Cenozoic active margin of Eurasia. *Tectonophysics*, **123**, 123-152.

Kempe, U., Gruner, T., Nasdala, L., Wolf, D. 2000. Relevance of cathodoluminescence for the interpretation of U-Pb zircon ages, with an example of an application to a study of zircons from the Saxonian Granulite Complex. In: *Cathodoluminescence in Geosciences* (Ed M. Pagel, Barbin, V., Blanc, P., Ohnenstetter, D.), pp. 415-455. Springer-Verlag, Berlin–Heidelberg.

Klötzli, U. S. 1997. Single zircon evaporation thermal ionisation mass spectrometry: method and procedures. *Analyst (the)*, **122**, 1239-1248.

Kober, B. 1986. Whole-grain evaporation for $^{207}Pb/^{206}Pb$-age-investigations on single zircons using a double-filament thermal ion source. *Contribution to Mineralogy and Petrology*, **93**, 482-490.

Kober, B. 1987. Single-zircon evaporation combined with Pb+ emitter bedding for $^{207}Pb/^{206}Pb$-age investigation using thermal ion mass spectrometry, and implications to zirconology. *Contribution to Mineralogy and Petrology*, **96**, 63-71.

Kockel, F., Mollat, H., Walther, H. W. 1971. Geologie des Serbo-Mazedonischen Massivs und seines mesozoischen Rahmens (Nordgriechenland). *Geologische Jahrbuch*, **89**, 529-551.

Kolceva, K., Zeljazkova-Panajotova, M., Dobrecov, N. L., Stojanova, V. 1986. Eclogites in Rhodope Metamorphic Group and their retrograde metamorphism. *Geochemistry, Mineralogy and Petrology*, **20-21**, 130-144.

Kolceva, K., Eskenazy, G. 1988. Geochemistry of metaeclogites from Central and Eastern Rhodope Mts (Bulgaria). *Geologica Balcanica*, **18**, (5): 61-78.

Kostopoulos, D. K., Ioannidis, N. M., Sklavounos, S. A. 2000. A new Occurence of Ultrahigh-Pressure Metamorphism, Central Macedonia, Northern Greece: Evidence from Graphitizedd Diamonds? *International Geology Reviews*, **42**, 545-554.

Kostopoulos, D., Gerdjikov, I. , Gautier, P., Reischmann, T., Cherneva, Z. 2003. First evidence of UHP metamorphism in the Central Rhodope Massif of southern Bulgaria. *Geophysical Research Abstracts*, **5**, 08327.

Kounov, A. 2002. Thermotectonic evolution of the Kraište, western Bulgaria. PhD, Swiss Federal Institute of Technology, Zürich, 221 pp.

Kretz, R. 1983. Symbols for rock-forming minerals. *American Mineralogist*, **68**, 277-279.

Krohe, A., Mposkos, E. 2002. Multiple generations of extensional detachments in the Rhodope Mountains (northern Greece): evidence of episodic exhumation of high-pressure rocks. In: *The Timing and Location of Major Ore Deposits in an Evolving Orogen* (Ed N. F. Blundell D. J., von Quadt A.), **204**, pp. 151-178. Geological Society Special Publication, London.

Kronberg, P. 1969. Gliederung, Petrographie und Tektogenese des Rhodopen-Kristallins im Tsal-Dag, Simvolon und Ost-Pangaon (Griechisch-Makedonien). *Geotektonische Forschungen*, **31**, 1-49.

Kronberg, P., Raith, M. 1977. Tectonics and metamorphism of the Rhodope crystalline complex in the Eastern Greek Macedonia and parts of Western Thrace. *Neue Jahrbuch fuer Geologie und Palaeontologie Monatshefte*, **45**, 697-704.

Lardeaux, J.-M., Ledru, P., Daniel, I., Duchene, S. 2001. The Variscan French Massif Central- a new addition to the ultra-high pressure metamorphic "club": exhumation processes and geodynamic consequences. *Tectonophysics*, **332**, 143-167.

Liati, A. 1986. Regional metamorphism and overprinting contact metamorphism of the Rhodope zone, near Xanthi (N. Greece). PhD, Technischen Universität Carolo-Wilhelimina, Braunschweig, 185 pp.

Liati, A., Seidel, E. 1996. Metamorphic evolution and geochemistry of kyanite eclogites in central Rhodope, northern Greece. *Contributions to Mineralogy and Petrology*, **123**, 293-307.

Liati, A., Gebauer, D. 1999. Constraining the prograde and retrograde P-T-t path of Eocene HP rocks by SHRIMP dating of different zircon domains: inferred rates of heating, burial, cooling and exhumation for central Rhodope, northern Greece. *Contributions to Mineralogy and Petrology*, **135**, 340–354.

Liati, A., Gebauer, D. 2001. Palaeozoic as well as Mesozoic sedimentation and polymetamorphism in Central Rhodope (N. Greece) as inferred from U-Pb SHRIMP-dating of detrital zircons. *Journal of Conference Abstracts*, **6 (1)**, 315.

Liati, A., Gebauer, D., Fanning, M. C. 2004. U-Pb zircon SHRIMP geochronology and REE geochemistry in (U)HP terranes: the example of Central Rhodope, N Greece. In: *5th International Symposium on the Eastern Mediterranean Geology*, **3**, pp. 1155-1158, Thessaloniki, Greece.

Liati, A., Gebauer, D., Fanning, M. C. 2004. The age of ophiolitic rocks of the Hellenides (Vourinos, Pindos, Crete): first U–Pb ion microprobe (SHRIMP) zircon ages. *Chemical Geology*, **207**, 171-188.

Liati, A. 2005. Identification of repeated Alpine (ultra) high-pressure metamorphic events by U-Pb SHRIMP geochronology and REE geochemistry of zircon: the Rhodope zone of Northern Greece. *Contrib Mineral Petrol*, **in press**.

Lips, A. L. W., White, S. H., Wijbrans, J. R. 1998. $^{40}Ar/^{39}Ar$ laserprobe direct dating of discrete deformational events: a continuous record of early Alpine tectonics in the Pelagonian Zone, NW Aegean area, Greece. *Tectonophysics*, **298**, 133-153.

Lips, A. L. W., White, S. H., Wijbrans, J. R. 2000. Middle-Late Alpine thermotectonic evolution of the southern Rhodope Massif, Greece. *Geodinamica Acta*, **13**, 281–292.

Lister, G. S., Banga, G., Feenstra, A. 1984. Metamorphic core complexes of cordilleran type in the Cyclades, Aegean Sea, Greece. *Geology*, **12**, 221-225.

Liu, F., Zhang, Z., Katayama, I., Xu, Z., Maruyama, S. 2003. Ultrahigh-pressure metamorphic records hidden in zircons from amphibolites in Sulu Terrane, eastern China. *The Island Arc*, **12**, 256-267.

Ludwig, K. R. 1998. On the treatment of concordant uranium-lead ages. *Geochimica et Cosmochimica Acta*, **62**, (4): 665-676.

Ludwig, K. R. 2001. SQUID 1.02: A user's manual. Berkeley Geochronology Center Special Publication, **2**, 19 pp.

Ludwig, K. R. 2003. Using Isoplot/Ex, Version 3.00: a geochronological toolkit for Microsoft Excel. Berkeley Geochronology Center Special Publication, **4**, 70 pp.

Magganas, A. C. 2002. Constraints on the petrogenesis of Evros ophiolite extrusives, NE Greece. *Lithos*, **65**, 165-182.

Maluski, H., Bonneau, M., Kienast, J.-R. 1987. Dating the metamorphic events in the Cycladic area: $^{39}Ar/^{40}Ar$ data from metamorphic rocks of the island of Syros (Greece). *Bulletin de la Société géologique de France*, **III (8)**, (5): 833-842.

Matte, P. 1991. Accretionnary history and crustal evolution of the Variscan belt in Western Europe. *Tectonophysics*, **196**, 309-337.

Mercier, J. L. 1968. Étude géologique des zones internes des Hellénides en Macédoine centrale (Grèce), thèse, université de Paris. *Annales Geologique des Pays Helleniques*, **20**, 1-792.

Moriceau, R. 2000. Evolution du massif métamorphique du Rhodope (Grèce, Bulgarie) dans le contexte alpin. Structures, cinématique et origine de la déformation ductile. PhD, University of Rennes I (France), Rennes, 537 pp.

Mposkos, E. D., Liati, A. 1993. Metamorphic evolution of metapelites in the high-pressure terrane of the Rhodope Zone, northern Greece. *Canadian Mineralogist*, **31**, 401-424.

Mposkos, E. D., Kostopoulos, D. K. 2001. Diamond, former coesite and supersilicic garnet in metasedimentary rocks from the Greek Rhodope: a new ultrahigh-pressure metamorphic province established. *Earth and Planetary Science Letters*, **192**, 497-506.

Mposkos, E. D. 2001. Petrology of the ultra-high pressure metamorphic Kimi Complex in Rhodope (N. E. Greece): a new insight into the Alpine geodynamic evolution of the Rhodope. *Bulletin of the Geological Society of Greece*, **34**, (6): 2169-2188.

Mposkos, E. D., Kostopoulos, D. K. 2003. Reply to comment on "Diamond, former coesite and supersilicic garnet in metasedimentary rocks from the Greek Rhodope: a new ultrahigh-pressure metamorphic province established" by O. Beyssac and C. Chopin. *Earth and Planetary Science Letters*, **214**, 675-678.

Nasdala, L., Lengauer, C. L., Hanchar, J. M., Kronz, A., Wirth, R., Blanc, P., Kennedy, A. K., Seydoux-Guillaume, A-M. 2002. Annealing radiation damage and the recovery of cathodoluminescence. *Chemical Geology*, **191**, 121-140.

Neumann, P., Zacher, W. 2004. The Cretaceous sedimentary history of the Pindos Bassin (Greece). *International Journal of Earth Sciences*, **93**, 119-131.

Okay, A. I., Satir, M., Tüysüz, O., Akyüz, S., Chen, F. 2001. The tectonics of the Strandja Massif: late-Variscan and mid-Mesozoic deformation and metamorphism in the northern Aegean. *International Journal of Earth Sciences*, **90**, 217-233.

Ovtcharova, M., Cherneva, Z., von Quadt, A., Peytcheva, I. 2002. Migmatitic geochronology and geochemistry - a key to understand the exhumation of the Madan dome (Bulgaria). *Geochimica et Cosmochimica Acta*, **66**, A573 (abstr.).

Ovtcharova, M., von Quadt, A., Cherneva, Z., Sarov, S., Heinrich, C., Peytcheva, I. 2004. U-Pb dating of zircon and monazite from granitoids and migmatites in the core and eastern periphery of the Central Rhodopean Dome, Bulgaria. *Geochimica et Cosmochimica Acta*, **68**, (11): A664 (abstr.).

Papanikolaou, D., Panagopoulos, A. 1981. On the structural style of Southern Rhodope, Greece. *Geologica Balcanica*, **11**, (3): 13-22.

Papanikolaou, D. J. 1997. The tectonostratigrapic terranes of the Hellenides. *Annales Géologiques des Pays Helléniques*, **37**, 496-514.

Pattison, D. R. M. 2003. Petrogenetic significance of orthopyroxene-free garnet + clinopyroxene + plagioclase +/- quartz-bearing metabasites with respect to the amphibolite and granulite facies. *Journal of metamorphic Geology*, **21**, 21-34.

Pearce, J. A., Harris, N. B. W., Tindle, A. G. 1984. Trace element diagrams for the teconic interpretation of granitic rocks. *Journal of Petrology*, **25**, 956-983.

Perraki, M., Proyer, A., Mposkos, E., Kaindl, R., Baziotis, I., Hoinkes, G. 2004. Micro-and nanodiamonds in garnets of the metapelitic rocks from the Greek Rhodope: an in situ micro-Raman study. In: *5th International Symposium on the Eastern Mediterranean Geology*, **3**, pp. 1216-1219, Thessaloniki, Greece.

Peytcheva, I., von Quadt A. 1995. U–Pb zircon dating of metagranites from Byala Reka region in the East Rhodopes, Bulgaria. In: *XV Congress of the Carpatho-Balcan Geological Association* (Ed G. S. o. Greece), **Special Publication 4**, pp. 637–642, Athens, Greece.

Peytcheva, I., von Quadt, A., Ovtcharova, M., Handler, M., Neubauer, F., Salnikova, E., Kostitsyn, Y., Sarov, S., Kolcheva, K. 2004. Metagranitoids from the eastern part of the Central Rhodopean Dome (Bulgaria): U–Pb, Rb–Sr and $^{40}Ar/^{39}Ar$ timing of emplacement and exhumation and isotope-geochemical features. *Mineralogy and Petrology*, **82**, 1-31.

Pidgeon, R. T., Nemchin, A. A., Hitchen, G. J. 1998. Internal structures of zircons from Archaean granites from the Darling Range batholith: implications for zircon stability and the interpretation of zircon U-Pb ages. *Contributions Mineralogy and Petrology*, **132**, 288-299.

Powell, R., Holland, T. J. B. 1994. Optimal geothermometry and geobarometry. *American Mineralogist*, **79**, 120-133.

Powell, R., Holland, T. J. B., Worley, B. 1998. Calculating phase diagrams involving solid solutions via non-linear equations, with examples using THERMOCALC. *Journal of Metamorphic Geology*, **16**, 577-588.

Reischmann, T., Kostopoulos, D. K., Loos, S., Anders, B., Avgerinas, A., Sklavounos, S. A. 2001. Late Palaeozoic magmatism in the basement rocks southwest of Mt. Olympos, Central Pelagonian Zone, Greece: Remnants of a Permo-Carboniferous magmatic arc. *Bulletion of the Geological Society of Greece*, **25**, 985-993.

Reischmann, T., Kostopoulos, D. K. 2001. Geochronology and PT constraints on the exhumation history of an UHP eclogite from Northern Greece. In: *AGU, Fall Meeting*, **82(47)**, pp. F1344. Eos. Trans.

Reischmann, T., Kostopoulos, D. 2002. Timing of UHPM in metasediments from the Rhodope Massif, N Greece. *Geochimica and*

Cosmochimica Acta, **66**, A633 (abstr.).

Ricou, L. E. 1994. Tethys reconstructed: plates, continental fragments and their Boundaries since 260 Ma from Central America to South-eastern Asia. *Geodynamica Acta (Paris)*, **7**, (4): 169-218.

Ricou, L.-E., Burg, J.-P., Godfriaux, I., Ivanov, Z. 1998. Rhodope and Vardar: the metamorphic and the olistostromic paired belts related to the Cretaceous subduction under Europe. *Geodynamica Acta (Paris)*, **11**, (6): 285-309.

Ring, U., Layer, P. W., Reischmann, T. 2001. Miocene high-pressure metamorphism in the Cyclades and Crete, Aegean Sea, Greece: Evidence for large-magnitude displacement on the Cretan detachment. *Geology*, **29**, (5): 395-398.

Robertson, A. H. F., Dixon, J. E. 1984. Aspects of the geological evolution of the Eastern Mediterranean. In: *The Geological Evolution of the Eastern Mediterranean* (Ed J. E. Dixon, Robertson, A. H. F.), *Geological Society of London special publications*, **17**, pp. 1-74. Blackwell Scientific Publications.

Robertson, A. H. F., Shallo, M. 2000. Mesozoic–Tertiary tectonic evolution of Albania in its regional Eastern Mediterranean context. *Tectonophysics*, **316**, 192-254.

Robertson, A. H. F. 2002. Overview of the genesis and emplacement of Mesozoic ophiolites in the Eastern Mediterranean Tethyan region. *Lithos*, **65**, 1-67.

Romano, S. S., Doerr, W., Zulauf, G. 2004. Cambrian granitoids in he pre-Alpine basement of Crete (Greece): evidence from U-Pb dating of zircon. *International Journal of Earth Sciences*, **93**, 844-859.

Rubatto, D., Gebauer, D. 2000. Use of cathodoluminescence for U-Pb zircon dating by ion microprobe: some examples from the Western Alps. In: *Cathodoluminescence in Geosciences* (Ed M. Pagel, Barbin, V., Blanc, P., Ohnenstetter, D.), pp. 373-400. Springer-Verlag, Berlin–Heidelberg.

Schermaier, A., Haunschmid, B., Finger, F. 1997. Distribution of Variscan I- and S-type granites in the Eastern Alps a possible clue to unravel pre-Alpine basement structures. *Tectonophysics*, **272**, 315-333.

Schermer, E. R., Lux, D. R., Burchfield, B. C. 1990. Temperature-Time history of subducted continental crust, Mount Olympos region, Greece. *Tectonics*, **9**, (5): 1165-1195.

Schermer, E. R. 1990. Mechanisms of blueschist creation and preservation in an A-type subduction zone, Mount Olympos region, Greece. *Geology*, **18**, 1130-1133.

Schermer, E. R. 1993. Geometry and kinematics of continental basement deformation during the Alpine orogeny, Mt. Olympos region Greece. *Journal of Structural Geology*, **15**, (3-5): 571-591.

Sengör, A. M. C., Cin, A., Rowley, D. B., Nie, S-Y. 1993. Space-Time patterns of Magmatism along the Tethysides: A Preliminary Study. *The Journal of Geology*, **101**, 51-84.

Skourlis, K., Doutsos, T. 2003. The Pindos Fold-and-thrust belt (Greece): inversion kinematics of a passive continental margin. *International Journal of Earth Sciences*, **92**, 891-903.

Sokoutis, D., Brun, J.-P., Van Den Driessche, J., Pavlides, S. 1993. A major Oligo-Miocene detachment in southern Rhodope controlling north Aegean extension. *Journal of the Geological Society, London*, **150**, 243-246.

Soldatos, T., Christofides, G. 1986. Rb-Sr geochronology and origin of the Elatia Pluton, Central Rhodope, North Greece. *Geologica Balcanica*, **16**, (1): 15-23.

Stacey, J. S., Kramers, J. D. 1975. Approximation of terrestrial lead isotope evolution by a two-stage model. *Earth and Planetary Science Letters*, **26**, 206-221.

Stampfli, G. M., Borel, G. D. 2002. A plate tectonic model for the Paleozoic and Mesozoic constrained by dynamic plate boundaries and restored synthetic oceanic isochrons. *Earth and Planetary Science Letters*, **196**, 17-33.

Turpaud, P., Reischmann, T. 2003. Zircon ages of granitic gneisses from the Rhodope (N. Greece), determination of basement age and evidences for a cretaceous intrusive event. *Geophysical Research Abstracts*, **5**.

van Hinsbergen, D. J. J., Hafkensheid, E., Spakman, W., Meulenkamp, J. E., Wortel, R. 2005. Nappe stacking resulting from subduction of oceanic and continental lithosphere below

Greece. *Geology*, **33**, (4): 325-328.

Vance, D., Müller, W., Villa, I. M. (eds) 2003. Geochronology: Linking the Isotopic Record with Petrology and textures. Geological Society, London, Special Publications, **220**, 272 pp.

Vavassis, I., De Bono, A., Stampfli, G. M., Giorgis, D., Valloton, A., Amelin, Y. 2000. U-Pb and Ar-Ar geochronological data from the Pelagonian basement in Evia (Greece): geodynamic implication for the evolution of Paleothetys. *Schweizerische Mineralogische und Petrographische Mitteilungen*, **80**, 21-43.

Vavra, G., Schmid, R., Gebauer, D. 1999. Internal morphology, habit and U-Th-Pb microanalysis of amphibolite-to-granulite facies zircons: geochronology of the Ivrea Zone (Southern Alps). *Contributions to Mineralogy and Petrology*, **134**, 380-404.

von Braun, E. 1993. The Rhodope question viewed from Eastern Greece. *Z. dt. geol. Ges.*, **144**, 406-418.

Warzenitz, N., Baumann, A., Nollau, G. 1994. Miocene uplift of mid-crustal rocks in the Rodope metamorphic core complex, caused by late alpine extension of previously thickened crust (Thassos island, Pangeon complex, northern Greece). In: *7th congress of the Geological Society of Greece*, **XXX/1**, pp. 147-157, Thessaloniki.

Weindenbeck, M., Allé, P., Corfu, W. L., Griffin, W. L., Meier, M., Oberli, F., Von Quadt, A., Roddick, J. C., Spiegel, W. 1995. Three natural zircon standards for U-Th-Pb, Lu-Hf, trace element and REE analyses. *Geostandards newsletter*(19): 1-23.

Wetherill, G. W. 1956. Discordant uranium-lead ages. *Trans. Amer. Geophys. Union*, **37**, 320-326.

Williams, I. S., Buick, I. S., Cartwright, I. 1996. An extended episode of early Mesoproterozoic metamorphic fluid flow in the Reynolds Range, central Australia. *Journal of Metamorphic Geology*, **14**, 29-47.

Williams, I. S. 1998. U-Th-Pb geochronology by ion microprobe. In: *Application of microanalytical techniques to understanding mineralizing processes* (Ed M. A. McKibben, Shanks III, W. C., Ridley, W. I.), *Reviews in Economic Geology*, **7**, pp. 1-35.